## Title

Eddy Current Correction in PC-MRI: An Analysis of Local and Global Static Tissue Fitting Techniques

## Permalink

https://escholarship.org/uc/item/9z85q488

## Author

Chinchali, Avinash Pramod

## Publication Date

2018

UNIVERSITY OF CALIFORNIA

Los Angeles

# Eddy Current Correction in PC-MRI: An Analysis of Local and Global Static Tissue Fitting Techniques.

A dissertation submitted in partial satisfaction of the requirements for the degree of

Masters of Science in Bioengineering

by

Avinash Pramod Chinchali

2018

# ABSTRACT OF DISSERTATION

## Eddy Current Correction in PC-MRI: An Analysis of Local and Global Static Tissue Fitting Techniques.

by

Avinash Pramod Chinchali
Masters of Science in Bioengineering
University of California, Los Angeles, 2018
Professor Daniel B. Ennis, Chair

Eddy currents induce velocity errors ($v_{eddy}$) that influence PC-MRI derived parameters; static tissue corrections aim to minimize these $v_{eddy}$ influences. Local and global static tissue corrections have been proposed; however, these separate strategies have yet to be thoroughly characterized. The dependence of local and global static tissue corrections on SNR and the amount of static tissue used for correction is not well understood. To characterize these relationships, corrections were analyzed within a static phantom and flow phantom experiment. Corrections were repeated for a range of SNR and for increasing amounts of static tissue used for polynomial fitting. Local and global corrections were separately applied to reduce velocity offset within ROIs within a static tissue phantom. Global correction reduced velocity offset in 100% of ROIs and local correction reduced velocity offset in ~96% of ROIs. Local correction introduced error in ~4% of ROIs (always when

SNR < 30). Correction differences between local and global strategies in the static phantom experiment were on the order of 0.9 cm/s for low SNR protocols and 0.2 cm/s for high SNR protocols. Velocity offset within static ROIs was reduced by up to an additional ~0.6 cm/s by increasing static tissue coverage for low SNR protocols (~0.05 cm/s for high SNR protocols). Local and global corrections were separately applied to correct total volumetric flow estimates within a flow phantom. $V_{eddy}$ errors induce differences between total flows measured at different locations along a flow phantom. Static tissue corrections reduced these differences between total flow estimates in 90% of corrections. Of these cases, global correction provided a larger reduction in flow difference ~67% of the time. Local fitting introduced error in ~27% of total corrections, and errors were observed for a range of SNR. Global fitting introduced one instance of error (for lowest SNR). Flow differences were reduced by up to an additional ~2 mL by increasing static tissue coverage. This study indicates that: 1) Local static tissue correction is suitable only for higher SNR PC-MRI applications and 2) Maximizing the amount of static tissue used during polynomial fitting improves performance of applied corrections for low SNR applications.

The thesis of Avinash Pramod Chinchali is approved

Debiao Li

Holden H. Wu

Daniel B. Ennis, Committee Chair

University of California, Los Angeles

2018

## Table of Contents

**Page(s)**

**Chapter I**: Introduction to Phase Contrast MRI (PC-MRI)

**Chapter II**: Gradient Attributed Phase Errors

**Chapter III**: Specific Aims

## Table of Contents (continued)

**Page(s)**

**Chapter IV**: Static Phantom Experiment

**Chapter V**: Flow Phantom Experiment

**Chapter VI**: Conclusion

# List of Figures and Tables

**Page(s)**

**Chapter I**

**Chapter II**

**Chapter IV**

## List of Figures and Tables (continued)

**Page(s)**

**Chapter IV**

**Chapter V**

# Chapter I: Introduction to Phase-Contrast MRI (PC-MRI)

## 1. Overview

Traditional MRI is a well-validated imaging modality that is used clinically to obtain accurate anatomical depictions of underlying tissue and structure. The images from a MRI scan are analyzed both qualitatively and often times quantitatively to gain insight into a patient's specific condition. MRI has shown usefulness in a wide range of medical fields, ranging from cardiovascular all the way to oncology applications to just name a few. MRI data is complex in nature and therefore possesses both magnitude and phase components. Traditionally in MRI, a clinician will look at the magnitude data images from a scan as these will best depict underlying anatomical structures within the patient. However, a wide range of MRI applications take advantage of collected phase data to draw conclusions about patient health as well. Phase contrast MRI (PC-MRI) is one of such subsets of MRI. It is important to note that traditional MRI and PC-MRI techniques are both non-invasive techniques that do not expose patients to ionizing radiation.

PC-MRI is a technique that encodes the velocity of hydrogen protons or “spins” (terminology used interchangeably) into the phase of the detected MRI signal. Hydrogen protons are abundant within the human body, therefore the PC-MRI technique can draw insight into overall tissue motion and blood flow within a patient. Abnormal tissue motion and blood flow patterns within a patient are often indicative of serious underlying pathologies, highlighting the clinical usefulness of the PC-MRI technique. A wide variety of parameters can be calculated using the PC-MRI experiment, dependent upon final intended application. Table 1.1 lists various parameters calculated from PC-MRI experiments and their clinical usefulness. A specific application of the PC-MRI experiment that will be discussed in detail within this section is PC-MRI's usefulness towards the study and evaluation of intracranial aneurysms.

| **Calculated Parameter** | **Clinical Usefulness** |
|---|---|
| Mean and peak blood flow velocity, total flow | Stenosis, regurgitant flow, and abnormal blood flow pattern evaluation |
| 3D blood flow velocity streamlines | Angiography and blood flow pattern evaluation |
| Vessel compliance | Atherosclerosis, hypertension, and aneurysm evaluation |
| Vessel wall shear stress | Vascular remodeling and heart failure evaluation |
| Tissue motion estimation | Tissue strain rate and ischemia evaluation |

***Table 1.1.*** *Sample calculated parameters from PC-MRI protocols and their clinical usefulness.*

An aneurysm is defined as the localized enlargement of a blood vessel caused by the weakening of the vessel wall itself. As an aneurysm grows in size it becomes increasingly prone to rupture; and the rupture of an aneurysm is a potentially fatal event that must be treated immediately. It has been shown that abnormal flow patterns within a vessel can promote aneurysm formation, growth, and eventual rupture. Namely, flow patterns within a vessel classified by the following characteristics contribute to overall aneurysm progression: 1) a concentrated vessel in-flow jet; 2) vorticity and other complex flow patterns within the intra-saccular region of the aneurysm itself; and 3) abnormal blood flow-vessel wall interactions, which manifest as concentrated areas exhibiting high vessel wall shear stress and larger surrounding areas exhibiting low vessel wall shear stress[1].

One particular application of PC-MRI, known as 4-dimensional flow (4D-flow), is sensitive to these defining characteristics associated with aneurysms[1,2]. 4D-flow is a technique that allows volumetric spatial encoding with blood flow sensitivity in three independent directions. This spatial and velocity information is acquired over multiple temporal phases to allow the visualization of complex blood flow patterns over both time and space, hence the "4-dimensional" name given to the technique. Using the 4D-flow technique, visualization of complete blood flow velocity fields within an aneurysm is possible. Velocity streamlines can be constructed using this flow field and thus yield an estimate of the number of indices associated with the inflow into an aneurysm[1]. The parameter of blood flow vorticity can be estimated as the curl of the measured velocity field and is important for the characterization of abnormal blood flow within the intrasaccular region of an aneurysm[1]. Vessel wall shear stress (WSS) within an aneurysm can then be estimated using the measured blood flow velocity gradient perpendicular to the vessel wall itself[1]. Together, these parameters show immense potential towards providing objective criteria for aneurysm risk stratification within the clinical scenario[1].

It is essential to note that accuracy in generated velocity flow fields is of key importance in 4D-flow as parameters used for clinical evaluations (such as velocity streamlines, WSS, and flow vorticity) are all calculated from estimated flow fields. Velocity flow fields in PC-MRI have been shown to suffer from inaccuracies due to motion artifacts, chemical shift effects, intravoxel dephasing effects, gradient-attributed phase errors, and more[1]. Errors and artifacts that must be accounted for within PC-MRI are a central theme of this work.

## 2. Encoding Velocity

The goal of the PC-MRI experiment is to create a direct relationship between the phase of the detected MRI signal and underlying spin motion (i.e. spins that exhibit velocity). In the context of many MRI applications, the source of signal is the $^1$H proton. Individual protons or spins will act as magnetic dipoles and, in the presence of an external magnetic field (say the $B_0$ magnetic field produced by the scanner), will coherently align to form a net detectable bulk magnetization vector; which is then manipulated throughout a given MRI protocol. It is important to note that the spin motion, which the PC-MRI experiment is sensitive to, is coherent, macroscopic motion on a scale greater than the pixel-level itself. Motion on a scale smaller than the pixel-level will be addressed in a later section of this chapter (see "intravoxel dephasing"). In addition, this coherent, macroscopic motion that PC-MRI is sensitive to ideally takes place during the magnetization preparation module of the protocol. Motion that occurs during the imaging/spatial encoding module of a protocol will manifest as motion artifacts and can often compromise the clinical acceptability of images produced from a given scan. Compensation for motion artifacts along with other errors specific to PC-MRI will also be discussed within a later section of this chapter.

This section derives the intrinsic relationship between measured signal phase and underlying spin motion or spin velocity that is present in MRI. This derivation is outlined in Markl's review of flow imaging and should be referred to for further detail[3].

A governing relationship that is fundamental to MRI is the Larmor Equation. This equation relates the precessional frequency of a given spin to the local magnetic field that this spin is exposed to (equation below is shown in the rotating coordinate frame). This equation is important in MRI because spatial localization for a given spin is dependent upon that spin's specific precessional frequency.

$$\vec{w}(r,t) = \gamma \cdot [\Delta B_0 + \vec{G}(t) \cdot \vec{r}(t)] \qquad \textbf{Eq 1.1}$$

*where:* - $w(r,t)$ = *precessional frequency (rotating coordinate frame), MHz*
- $\gamma$ = *gyromagnetic ratio for a given species (constant), MHz/T*
- $\Delta B_0$ = *time-invariant offsets to the* $B_0$ *magnetic field, T*
- $G(t)$ = *gradient waveform vector, T/m*
- $r(t)$ = *position vector, m*

Note that offsets to the static $B_0$ field (field inhomogeneities, chemical shift effects, magnetic susceptibility effects, coil sensitivities, etc.) and the application of gradients themselves will both alter the local magnetic field strength and thus cause a spin to precess at a different Larmor frequency. The offsets described by the $\Delta B_0$ term in Eq 1.1 are assumed to be time-invariant. Later sections in this chapter will describe how time-variant offsets to the static $B_0$ field can potentially arise in MRI experiments and why these effects are especially problematic (eddy current and Maxwell errors).

The amount of phase that a spin accumulates is related to the amount of rotation this spin experiences over a certain time interval. In MRI, the maximum received signal amplitude occurs during the formation of an echo, denoted as time “t = TE”, and is therefore often a time point of interest. Consider the phase of an ensemble of spins at spatial position “r” and echo time “TE”:

$$\begin{aligned}\vec{\phi}(r, t = TE) &= \int_{t=0}^{t=TE} \vec{w}(r, t)dt \\ &= \int_{t=0}^{t=TE} \gamma[\Delta B_0 + \vec{G}(t) \cdot \vec{r}(t)]dt \\ &= \int_{t=0}^{t=TE} \gamma \Delta B_0 dt + \int_{t=0}^{t=TE} \gamma[\vec{G}(t) \cdot \vec{r}(t)]dt \qquad \textbf{Eq 1.2}\end{aligned}$$

*where: - $\phi(r,t)$ = measured signal phase, radians*

Using a Taylor series expansion of the r(t) position vector within Eq 1.2 will then yield Eq 1.3 as follows:

$$
\begin{aligned}
\vec{\phi}(r, t = TE) &= \int_{t=0}^{t=TE} \gamma \Delta B_0 dt + \int_{t=0}^{t=TE} \gamma[\vec{G}(t) \cdot \vec{r}(t)]dt \qquad \textbf{Eq 1.3} \\
&= \int_{t=0}^{t=TE} \gamma \Delta B_0 dt + \int_{t=0}^{t=TE} \gamma(\vec{G}(t) \cdot [r_0 + v_0 t + \frac{1}{2} a_0 t^2 + \ldots])dt \\
&= \int_{t=0}^{t=TE} \gamma \Delta B_0 dt + \int_{t=0}^{t=TE} \gamma \vec{G}(t) \cdot r_0 dt + \\
&\int_{t=0}^{t=TE} \gamma \vec{G}(t) \cdot v_0 t dt + \int_{t=0}^{t=TE} \gamma \vec{G}(t) \cdot \frac{1}{2} a_0 t^2 dt + \ldots \\
&= \gamma \Delta B_0 \cdot TE + (\gamma r_0 \cdot \vec{M_0}) + (\gamma v_0 \cdot \vec{M_1}) + (\frac{1}{2} \gamma a_0 \cdot \vec{M_2}) + \ldots \\
&= \phi_{background} + (\gamma r_0 \cdot \vec{M_0}) + (\gamma v_0 \cdot \vec{M_1}) + (\frac{1}{2} \gamma a_0 \cdot \vec{M_2}) + \ldots
\end{aligned}
$$

*where:* - $r_0$ *= initial position of spin , m*
- $v_0$ *= initial velocity of moving spins, m/s*
- $a_0$ *= initial acceleration of moving spins,* $m/s^2$
- $\phi_{background}$ *= time-invariant background phase offset, radians*
- $M_0$ *= zero moment =* $\int G(t)\, dt$ *,* $s \bullet T/m$
- $M_1$ *= first moment =* $\int G(t) \bullet t\, dt$ *,* $s^2 \bullet T/m$
- $M_2$ *= second moment =* $\int G(t) \bullet (t^2)\, dt$ *,* $s^3 \bullet T/m$
- *… = higher order terms*

From Eq 1.3 it can directly be seen where the different sources of phase in a MRI experiment arise from. Eq 1.3 shows that the phase of the detected MRI signal depends on multiple sources: 1) phase contributions from deviations to the static $B_0$ field itself, called “background phase offsets”; 2) phase contributions from stationary spins (called $M_0$ contributions); 3) phase contributions from moving spins or spins that exhibit velocity (called $M_1$ contributions); and 4) phase contributions from higher order terms ($M_2$ acceleration contributions and higher). It is essential to remember that the magnetic field deviations which give rise to the background phase offset are time-invariant. Therefore, these field deviations will be constant between any two independent acquisitions implementing similar protocols (i.e. each independent acquisition of an identical protocol will have the same $\phi_{background}$ term). This unique attribute specific to the $\phi_{background}$ term will be taken advantage of in the PC-MRI experiment and will be discussed in further detail within the next section. Furthermore, it is equally important to discuss phase contributions arising from higher order terms in Eq 1.3. In a typical PC-MRI experiment, a pulse sequence that exhibits a short TE on the scale of milliseconds is usually implemented (for example, spoiled gradient echo sequences)[3]. It is generally a safe assumption when using these short TE sequences that spins will "appear" to be constant velocity during this time interval. Based upon this assumption, higher order phase contributions from spins that are accelerating and so on and so forth can now be considered null or non-significant. Under this new set of assumptions, Eq 1.3 will reduce to Eq 1.4 as follows:

$$\begin{aligned}
\vec{\phi}(r, t = TE) &= \int_{t=0}^{t=TE} \gamma \Delta B_0 dt + \int_{t=0}^{t=TE} \gamma[\vec{G}(t) \cdot \vec{r}(t)]dt \qquad \textbf{Eq 1.4} \\
&= \int_{t=0}^{t=TE} \gamma \Delta B_0 dt + \int_{t=0}^{t=TE} \gamma(\vec{G}(t) \cdot [r_0 + v_0 t + \frac{1}{2} a_0 t^2])dt \\
&= \int_{t=0}^{t=TE} \gamma \Delta B_0 dt + \int_{t=0}^{t=TE} \gamma \vec{G}(t) \cdot r_0 dt + \\
&\int_{t=0}^{t=TE} \gamma \vec{G}(t) \cdot v_0 t dt + \int_{t=0}^{t=TE} \gamma \vec{G}(t) \cdot \frac{1}{2} a_0 t^2 dt \\
&= \gamma \Delta B_0 \cdot TE + (\gamma r_0 \cdot \vec{M_0}) + (\gamma v_0 \cdot \vec{M_1}) + (\frac{1}{2} \gamma a_0 \cdot \vec{M_2}) \\
&= \phi_{background} + (\gamma r_0 \cdot \vec{M_0}) + (\gamma v_0 \cdot \vec{M_1}) + (\frac{1}{2} \gamma a_0 \cdot \vec{M_2})
\end{aligned}$$

The reduced Eq 1.4, which was derived based upon the short TE and constant spin velocity assumptions, still depends upon phase contributions from multiple sources: 1) contributions from background phase offsets ($\phi_{background}$); 2) contributions from stationary spins ($M_0$ contributions); and 3) contributions from moving spins ($M_1$ contributions). The ultimate goal of the PC-MRI experiment, as mentioned before, is to create a direct relationship between overall phase of the detected MRI signal and underlying spin velocity itself. In order to do so based upon Eq 1.4, the PC-MRI experiment must null or negate phase contributions from background phase offsets and stationary ($M_0$) contributions and thus be solely dependent upon moving ($M_1$) contributions alone. The next subsection will discuss in detail how the PC-MRI experiment can null phase contributions from $\phi_{background}$ and $M_0$, whilst still being sensitive to $M_1$ phase contributions.

### 3. PC-MRI Experiment

As previously mentioned, the goal of the PC-MRI experiment is to establish a direct relationship between the overall phase of the detected MRI signal and the underlying coherent spin motion. This direct relationship can be achieved only when phase contributions from $B_0$ field deviations ($\phi_{background}$) and phase contributions from stationary spins ($M_0$ contributions) are both nulled, and therefore the measured signal phase will now be dependent upon contributions from moving spins ($M_1$ contributions) alone. This section will now go into further detail to describe how the PC-MRI experiment nulls the background and $M_0$ phase contributions, whilst still encoding $M_1$ phase contributions. The gradient waveforms and implementation strategies applied to achieve this goal are described in Markl's review of flow imaging[3].

### *3A. $M_0$ Moment Nulling and $M_1$ Moment Encoding*

Nulling of the $M_0$ moment and encoding of the $M_1$ moment can be successfully achieved via implementation of "bipolar, flow encoding" gradients on the desired axis of velocity sensitivity. These "bipolar, flow encoding" gradients will be simply referred to as "flow encoding" gradients for the remainder of this work. Flow encoding gradients are played after slice-selective excitation, to encode velocity information into the phase of the generated MRI signal. Spatial localization gradients for imaging are implemented only after velocity has been successfully encoded into the MRI signal. Figure 1.1 of this section displays the flow encoding gradient waveform previously discussed. By definition, gradients impart phase upon spins by altering the local magnetic field that a spin experiences (via the Larmor relationship introduced in the previous section). In the PC-MRI experiment, all excited spins will thus be de-phased by the application of the flow encoding gradient. However, upon changing the polarity of the flow encoding gradient waveform itself, all spins will begin to be re-phased. Stationary spins will be de-phased and re-phased by equal amounts because these spins do not travel to new locations during the flow encoding waveform, and will therefore exhibit no net phase difference upon completion of this waveform. Spins that are moving will experience new local magnetic fields and will therefore not be equally de-phased and re-phased; and these moving spins will thus exhibit a net phase difference that is proportional to underlying spin velocity itself.

Therefore, it should now be evident that stationary spins will have no net contribution to the measured MRI signal phase after implementation of the flow encoding strategy previously described (nulled $M_0$ contributions to signal phase). Alternatively, spins that have intrinsic velocity will contribute to the overall measured MRI signal phase when implementing these same flow encoding strategies (non-zero $M_1$ contribution to signal phase).

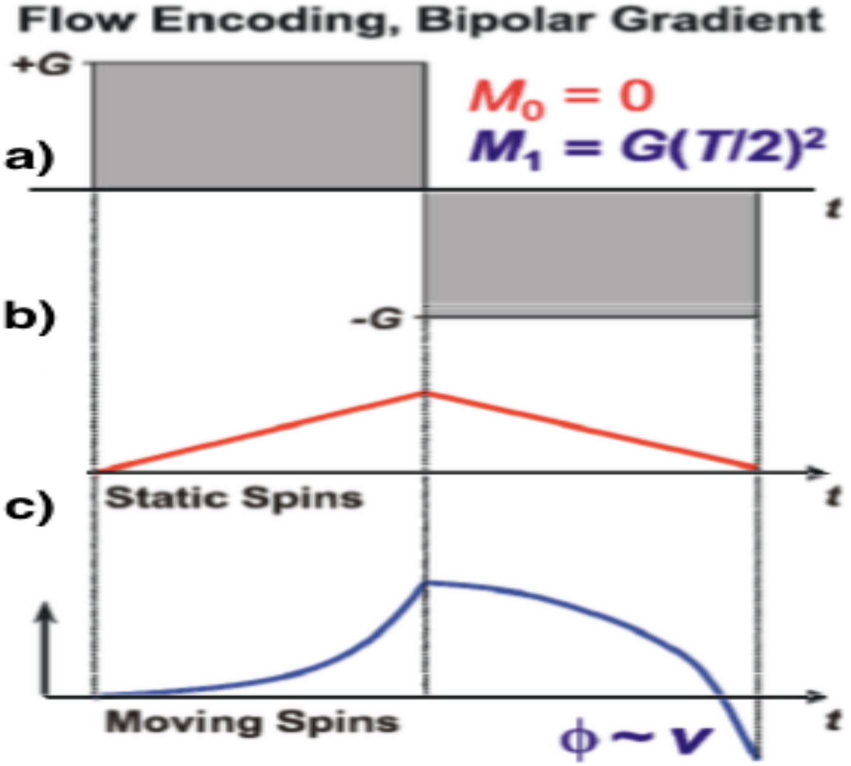

***Figure 1.1.*** *Bipolar, flow encoding gradient waveform for velocity sensitivity. (a) Bipolar, flow encoding gradient waveform itself, G(t). Net gradient area is zero. (b)* $M_o$ *moment profile tracked during the application of the flow encoding gradient waveform.* $M_0$ *moment is calculated as ∫ G(t) dt. Note that* $M_0$ *moment is nulled (zero) upon completion of the gradient waveform; therefore, stationary spins will not contribute to MRI signal phase. (c)* $M_1$ *moment profile tracked during the application of the same flow encoding gradient waveform.* $M_1$ *moment is calculated as ∫ G(t)•t dt. Note that* $M_1$ *moment is encoded (non-zero) upon completion of the gradient waveform; therefore, moving spins will contribute to MRI signal phase. Figure taken from Markl's review of flow imaging*[3]*.*

### *3B. Background Phase Offset Nulling*

As mentioned in a previous section, the PC-MRI experiment takes advantage of the fact that the background phase offset ($\phi_{background}$) created by two independent acquisitions of identical protocols will be equivalent. Consider some acquisition "A" which implements a flow encoding strategy such that $M_0$ contributions are nulled and $M_1$ contributions are encoded. The phase of the detected signal at echo formation can then be expressed as follows:

$$\phi(r, t = TE) = \phi_{background} + \gamma v_0 \cdot \vec{M}_{1A} \qquad \textbf{Eq 1.5}$$

Now consider some acquisition "B" which also implements a flow encoding strategy such that $M_0$ contributions are again nulled and $M_1$ contributions are again encoded. It is essential to note that the $M_1$ moments between independent acquisitions "A" and "B" are assumed to be different.

$$\phi(r, t = TE) = \phi_{background} + \gamma v_0 \cdot \vec{M}_{1B} \qquad \textbf{Eq 1.6}$$

A phase-difference reconstruction method can then be applied to create a direct relationship between measured signal phase and underlying spin velocity "$v_0$" on the pixel level itself (within phase difference maps).

$$\begin{aligned} \Delta\phi(r, t = TE) &= \phi_A - \phi_B \\ &= [\phi_{background} + \gamma v_0 \cdot \vec{M}_{1A}] - [\phi_{background} + \gamma v_0 \cdot \vec{M}_{1B}] \\ &= \gamma v_0 \cdot (\vec{M}_{1A} - \vec{M}_{1B}) \\ &= \gamma v_0 \cdot \Delta\vec{M}_1 \qquad \textbf{Eq 1.7} \end{aligned}$$

Note Eq 1.7 has a direct relationship between measured phase and underlying spin velocity "$v_0$" that is now completely free of contributions from background phase offsets. It is essential to realize that the $\Delta M_1$ term in Eq 1.7 can be calculated because original $M_{1,A}$ and $M_{1,B}$ encoding strengths are both known and user-controlled parameters. Rearrangement of Eq 1.7 allows for pixel level estimates of underlying spin velocity to be calculated within velocity maps (shown in Eq 1.8).

$$v_0 = \frac{\Delta\phi}{\gamma \cdot \Delta\vec{M}_1} \qquad \textbf{Eq 1.8}$$

Another key assumption with the phase difference reconstruction method not yet mentioned, is that the underlying spin velocity "$v_0$" is assumed to be the same between independent acquisitions, A and B. If underlying spin velocities during the temporal frame for acquisition A are inherently different than during the temporal frame for acquisition B, phase difference reconstruction is invalid and this can directly be seen from Eq 1.7. This phenomenon can occur for a wide variety of reasons, with non-periodic tissue motion and natural blood flow pulsatility being two examples. Consider the scenario where blood flow exiting the left ventricle and entering the aorta is of interest. In the according PC-MRI protocol, suppose that acquisition A is taken during diastole and acquisition B is taken during systole. Underlying blood flow velocities between the two acquisitions will be inherently different as no blood flow is expected to be entering the aorta during diastole for a healthy patient. Phase difference reconstruction therefore cannot be applied between acquisitions A and B in this scenario. Ensuring that acquisitions A and B are taken during the same temporal window of the cardiac cycle can deal with this blood pulsatility issue and will be discussed further within the “limitations and considerations” section.

It is also essential to realize at this point that the PC-MRI technique suffers from inherent time limitations. In order to directly relate phase measurements to underlying velocity, a minimum of two independent acquisitions (previously called acquisitions A and B) will have to be implemented and thus causes a two-fold increase in overall scan time. The number of independent acquisitions necessary can also increase as velocity information in an increasing number of directions is desired (ex. 4D-flow applications). This scan time constraint in PC-MRI will again be addressed in the “limitations and considerations” section of this chapter.

### *3C. Flow Compensation*

A common strategy used to estimate the background phase offset ($\phi_{background}$) itself is known as “flow compensation”. The signal phase from a flow compensated acquisition will be free of phase contributions from both $M_0$ and $M_1$ moments, and according to Eq 1.4 will therefore only depend upon the background phase offset ($\phi_{background}$) term. Therefore, a flow compensated acquisition can be considered a “universal reference” to which all other flow encoded acquisitions will be individually compared to for phase difference reconstructions. Figure 1.2 below describes the flow compensation gradient waveform itself and also tracks the $M_0$ and $M_1$ moment profiles throughout the application of this waveform. Note that flow compensation can be simultaneously implemented on $G_x$, $G_y$, and $G_z$ axes to compensate for spin motion in all directions.

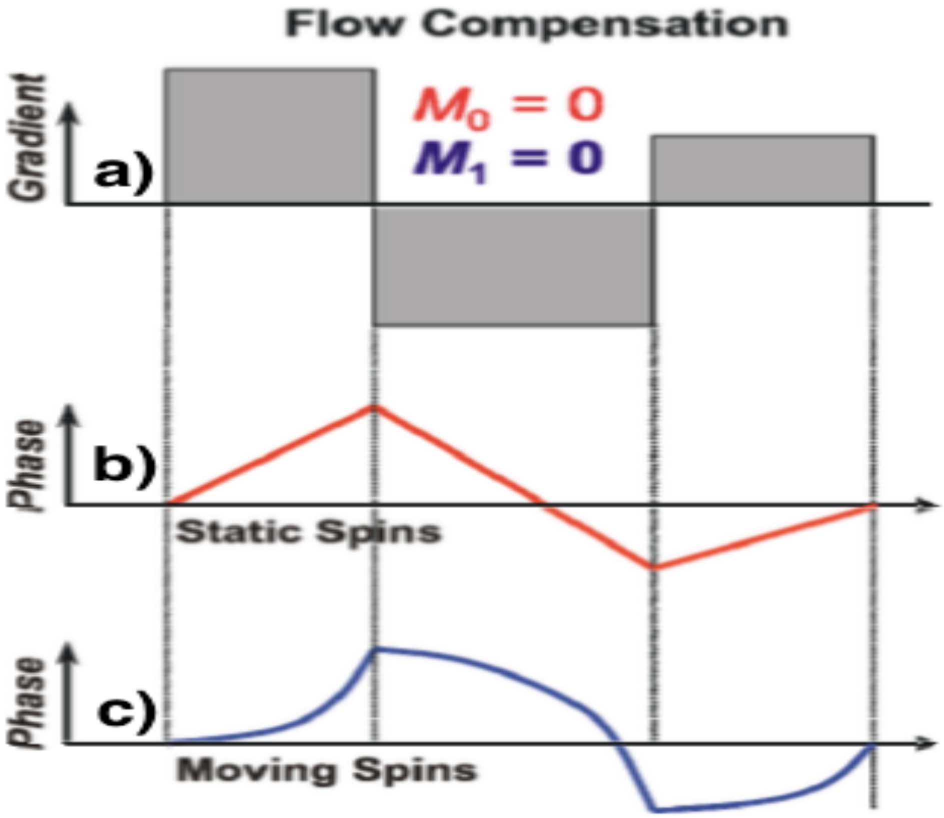

***Figure 1.2.*** *Flow compensation gradient waveform. (a) Flow compensation gradient waveform itself, G(t). (b)* $M_0$ *moment profile tracked during the application of the flow compensation gradient waveform.* $M_0$ *moment is calculated as* $\int G(t)\,dt$*. Note that* $M_0$ *moment is nulled (zero) upon completion of the gradient waveform; therefore, stationary spins will not contribute to MRI signal phase. (c)* $M_1$ *moment profile tracked during the application of the same flow compensation gradient waveform.* $M_1$ *moment is calculated as* $\int G(t)\bullet t\,dt$*. Note that* $M_1$ *moment is also nulled (zero) upon completion of the gradient waveform; therefore, moving spins will not contribute to MRI signal phase. Figure taken from Markl's review of flow imaging*[3]*.*

### *3D. Velocity Direction Sensitivity*

In the PC-MRI experiment, signal phase is sensitive to spin motion along the direction of the applied flow encoding gradients. For example, in order to be sensitive to spin motion along the "z-direction" or the long axis of the scanner, flow encoding gradients would be played along the $G_z$ gradient axis immediately after slice selective excitation. Recall that in MRI, any linear combination of $G_x$, $G_y$, and $G_z$ gradients can be implemented simultaneously. A simultaneous combination of flow encoding gradients on the $G_x$,$G_y$, and/or $G_z$ axes will thus allow for velocity sensitivity in any arbitrary direction of interest. The specific direction of spin motion along the measured velocity direction is determined by the sign of Eq 1.7 (if measuring velocity along the z-direction, the sign of Eq 1.7 will determine whether a spin is moving along +z or -z).

Often times the goal of a PC-MRI experiment is to measure velocity in multiple independent directions, for example the total velocity vector consisting of $<V_x, V_y, V_z>$ components. Recall that to measure a single component of the total velocity vector, say the $V_x$ component alone, two separate acquisitions will need to be implemented to account for the background phase offset term and thus directly relate measured phase to $V_x$ itself. Therefore, a total of six independent acquisitions will need to be implemented in order to recover each and every separate velocity component. However, implementing flow compensation strategies to estimate background phase offsets can reduce this total number of independent acquisitions from six down to four (see "pulse sequence" section). This is one of the primary advantages of implementing flow compensated reference strategies to estimate the background phase offset.

### *3E. Velocity Magnitude Sensitivity (VENC)*

Within the PC-MRI experiment, there is an inherent limitation to the maximum underlying spin velocity that can be encoded into the phase of the detected signal[4].

The maximum velocity that can be encoded into the phase of the MRI signal is referred to as "VENC" and is a user-controlled parameter. Recall that in MRI, phase can only be discriminated on a [-$\pi$ , $\pi$] dynamic range as this describes a full rotational coverage. Therefore, VENC also corresponds to the spin velocity that will create the maximum encode-able phase shift of ± $\pi$, given a specific $\Delta M_1$. Eq 1.9 mathematically describes the VENC parameter as follows:

$$VENC = \frac{\pi}{\gamma \cdot \Delta \vec{M}_1} \qquad \textbf{Eq 1.9}$$

*where:* $\Delta M_1$ *= difference between* $M_1$ *encoding strengths used for each acquisition,* $s^2 \bullet T/m$

Velocities that are outside the [-VENC, VENC] range will yield phase shifts outside ± п. A phase shift outside the dynamic range of [-$\pi$,$\pi$] will experience "phase wrapping" and therefore be erroneously mapped to a phase shift that actually lies within the [-$\pi$,$\pi$] dynamic range[4]. For instance, an actual phase shift of 3 $\pi$/2 will undergo "phase wrapping" and will be indistinguishable from a phase shift of – $\pi$/2; however, each of these two different phase shifts will yield drastically different velocity estimates based upon Eq 1.8. It is essential to avoid "phase wrapping" phenomena as these errors manifest as incorrect estimates of velocity magnitude and direction in output velocity map images (after phase difference reconstruction)[4]. Inaccurate estimates of velocity magnitude and direction directly compromise the clinical acceptability and usefulness of a given PC-MRI scan.

Optimal selection of the VENC parameter in PC-MRI is essential in order to mitigate the previously described "phase wrapping" phenomena. Ideally, VENC should be set to be greater than the maximum expected velocity from a given region of interest being studied. For example, if blood flow velocity in the thoracic aorta is of interest, VENC should be set to a value of around 150-200 cm/s as this value overestimates the maximum aortic blood flow velocities expected in healthy human adults[5]. Selection of the VENC parameter below "true" underlying velocities expected within the region of interest being studied will directly result in phase wrapping errors.

However, it is also important to realize that the selection of the VENC parameter cannot be arbitrarily large (although a larger VENC will indeed reduce the chances of phase wrapping errors). The reason for this is because selection of VENC is associated with an inherent velocity-to-noise ratio (VNR) penalty as highlighted by Eq 1.10[4].

$$VNR_{\Delta\phi} = SNR_{magnitude} \cdot \left(\frac{v_0}{VENC}\right) \qquad \textbf{Eq 1.10}$$

Recall in PC-MRI that pixel-level velocity estimates are directly calculated from the phase difference "$\Delta\phi$" reconstruction process, and therefore accuracy in $\Delta\phi$ estimates themselves are important. Velocity noise introduces inaccuracies in pixel-level $\Delta\phi$ estimates; VNR is a measure of this velocity noise. Increasing the magnitude of the VENC parameter reduces the VNR of $\Delta\phi$ images, and therefore directly detracts from $\Delta\phi$ estimate fidelity prior to velocity estimation. In practice, VENC is chosen to be large enough such that phase wrapping errors will not occur, but is also simultaneously minimized for optimal velocity noise performance[3]. The level of velocity noise itself is inversely related to the SNR of corresponding magnitude images acquired from a PC-MRI acquisition[3].

### *3F. Pulse Sequences and Image Acquisition*

As mentioned in the "encoding velocity" section, PC-MRI traditionally implements a short TE pulse sequence[3]. Short TE sequences are useful when underlying patient motion is significant and are often incorporated with segmented imaging schemes such as in cardiac PC-MRI applications. An example of such a sequence is the spoiled gradient echo (GRE) commonly used in PC-MRI. Many k-space acquisition strategies have been proposed for the PC-MRI experiment, including EPI, spiral, and radial trajectories; each with their own inherent advantages and disadvantages. In the following pulse sequence diagrams, the discussion will be limited to Cartesian acquisition schemes where k-space lines are acquired on a line-by-line basis. Consider the simplest PC-MRI experiment, measuring velocity in a single direction through a thin slice. The pulse sequence representing this experiment is depicted in Figure 1.3 below.

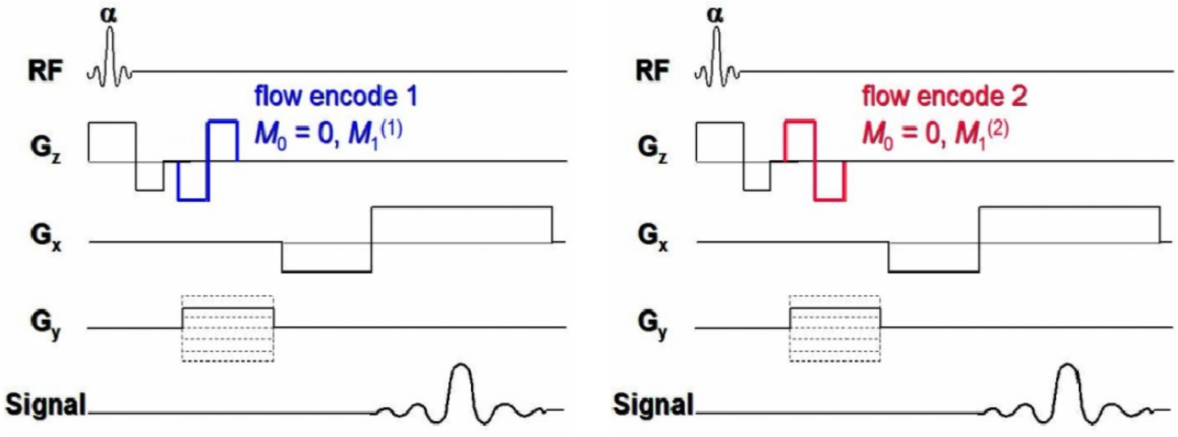

***Figure 1.3.*** *Basic, through-plane velocity PC-MRI pulse sequence. Flow encoding and slice-selective excitation waveforms are played on the same gradient axis. (a) First of two independent acquisitions with a unique flow encoding gradient, flow encode 1, played. Flow encode 1 is played following slice-selective excitation and prior to imaging gradients. (b) Second of two independent acquisitions with another unique flow encoding gradient, flow encode 2, played. Flow encode 2 is also played following slice-selective excitation and prior to imaging gradients. The* $M_1$ *moments created by flow encode 1 and flow encode 2 are unequal. Figure taken from Markl's review of flow imaging*[3].

Shown above are two independent acquisitions, each with unique $M_1$ moments encoded. Velocity sensitivity is along the z-axis because flow encoding gradients are played on $G_z$. Flow encoding $G_z$ gradients are played after slice selective excitation along z, therefore through-plane velocity is being encoded. Frequency and phase encoding gradients for 2D spatial localization are shown on $G_x$ and $G_y$ axes respectively. Spatial localization gradients (imaging gradients) are played after velocity has been successfully encoded into the MRI signal. The phase profiles generated by the two independent acquisitions will be used within the phase difference reconstruction process to develop output velocity maps. Various TE and gradient waveform optimized variants of the above shown pulse sequence exist, but are beyond the scope of this introductory PC-MRI chapter. An understanding of basic PC-MRI pulse sequences is sufficient for the remainder of this work. To expand upon the previous experiment, imagine velocity sensitivity is now desired in three independent directions through a thin slice. The pulse sequence for this experiment is depicted in Figure 1.4.

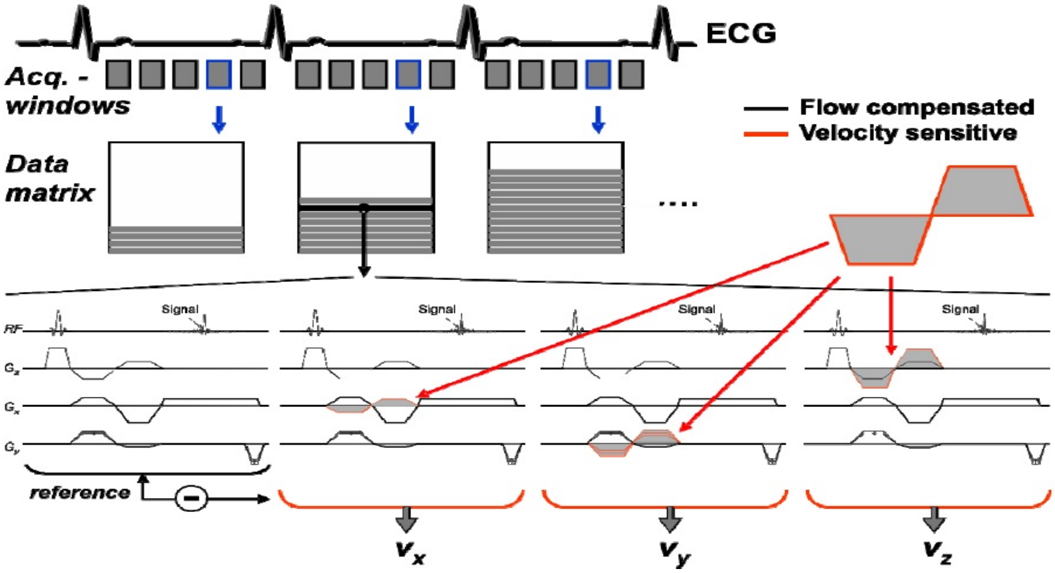

***Figure 1.4.*** *3-directional velocity sensitive PC-MRI pulse sequence. A flow compensated acquisition is first employed to estimate background phase offset itself. Subsequent acquisitions alternate the gradient axis which flow encoding waveforms are played on. An ECG triggered segmented acquisition scheme is employed to account for underlying cardiac motion. Phase difference reconstruction is then employed to develop* $V_x$*,* $V_y$*, and* $V_z$ *velocity maps. Figure taken from Markl's review of flow imaging*[3].

Shown above are four independent acquisitions, the first being a flow compensated acquisition used to estimate the background phase offset ($\phi_{background}$) alone. Note that during this "reference" acquisition, flow compensated waveforms are being simultaneously played on all gradient axes. This reference, flow compensated acquisition is then followed by separate flow encoding acquisitions played sequentially on $G_x$, $G_y$, and $G_z$ axes. $V_x$, $V_y$, and $V_z$ pixel-level velocity maps are constructed using the before-mentioned phase difference reconstruction method with the flow compensated acquisition considered the "universal reference" acquisition. Flow compensation and flow encoding gradients are both played after slice selective excitation. This sequence is implemented with an ECG triggered segmented acquisition strategy to suppress underlying cardiac motion artifacts (acquire different k-space matrices specific to different temporal phases of the cardiac cycle).

It is essential to note that scan time increases with an increasing the number of measured velocity directions (due to the need for a greater number of independent acquisitions). This scan time lengthening is further exacerbated when velocity information over various temporal phases is desired, for example measuring blood flow entering the aorta over the entire cardiac cycle (time-resolved velocity information). Time-resolved velocity data requires acquiring independent flow encoded or flow compensated acquisitions repeatedly for multiple different temporal phases of interest. Studies assessing flow within the thoracic aorta have implemented time-resolved PC-MRI protocols with two dimensions of spatial encoding and three dimensions of velocity encoding (2D-CINE-3dir) with acquisition times on the order of ~2 minutes given the following protocol parameters: 3T, 1.25x1.25x5 $mm^3$ voxel size, 24.4 ms temporal resolution, 3.57 ms TE, 6.1 ms TR, 455 Hz/pixel bandwidth, 15° flip angle, and 28 temporal phases acquired[6].
When considering PC-MRI experiments with volumetric spatial coverage (4D flow scans, etc.), scan times will compound in length even more significantly as phase encoding in a new, extra direction is also needed in addition to the traditional 2D frequency and phase encoding scheme for spatial localization. Due to the lengthening in TR from flow encoding gradients and the need for independent velocity encoded acquisitions in multiple directions, 4D flow sequences have been shown to be ~6x longer than traditional GRE sequences used for volumetric coverage in time-resolved contrast enhanced angiography[1]. Therefore, it should be

evident that overall scan time can quickly become a limiting factor in PC-MRI, dependent upon the intended application. This limiting constraint of scan time will be addressed once again in the "limitations and considerations" section.

## 4. Limitations and Considerations in PC-MRI

PC-MRI, like traditional MRI and other imaging modalities, suffers from a variety of limitations and constraints. Some of these considerations were briefly alluded to in previous sections but will now be formally discussed.

### *4A. Scan Time*

As discussed in the pulse sequence section, whenever more dimensions of spatial, temporal, and/or velocity encoding are desired for a specific PC-MRI application, scan time can easily grow to be clinically unacceptable in duration. Therefore it is essential to implement various acceleration techniques in order to reduce scan times down to acceptable clinical time scales. Implementation of short TE pulse sequences that exhibit optimized sequences (where slice selective, flow encoding/compensation gradients, and imaging gradients are combined whenever possible) can help significantly reduce overall scan time[3]. In addition, alternative k-space sampling trajectories such as radial and spiral trajectories have also shown promise in accelerating scan times. Other acceleration options include parallel imaging and compressed sensing techniques[7]. With the implementation of k-t GRAPPA and spiral or radial k-space sampling trajectories, 4D flow scan times have been reduced to about ~10 minutes for coverage of the aorta and ~15 minutes for coverage of the whole heart[5]. It is essential to note the immense potential that these techniques offer in reducing PC-MRI scan times; however, scan time acceleration is not a central theme of this work and will not be discussed at length.

### *4B. Motion Artifacts*

Although PC-MRI aims to be sensitive to macroscopic motion of spins, motion during the spatial encoding or imaging module of a protocol is unwanted and will appear as motion artifacts in acquired images. Motion artifacts are most apparent along the phase encoding direction of magnitude images from a scan. For cardiac PC-MRI scans, segmented imaging strategies triggered to a patients pulse rate or QRS waveform are implemented to deal with the rapid beating motion of the heart. Segmented imaging and implementing interleaved flow encodes as close in time as possible to each other can also help deal with flow pulsatility related motion artifacts[3]. Motion artifacts can also be suppressed using flow compensated reference acquisitions, and in some cases by swapping the phase encoding and frequency encoding directions. In addition, certain k-space acquisition strategies that heavily over-sample the center of k-space tend to be more robust to motion artifacts (radial and spiral trajectories). Finally, non-harmful physical restraints and sedatives may be used to suppress unwanted patient motion if deemed appropriate by a trained clinician.

### *4C. Phase Wrapping*

The concern of phase wrapping was first introduced in the section discussing the VENC parameter. Phase wrapping can be avoided by selecting a VENC higher than the expected underlying spin velocities to be studied, however this prior knowledge may not always be known. In such cases, a “VENC scout” technique can be implemented to determine the optimal selection of VENC and thus avoid the phase wrapping phenomenon altogether[4]. This technique involves repeated acquisitions each with a unique VENC selection. This process is repeated until velocity is deemed to be free of aliasing effects. Various groups have also investigated phase un-wrapping algorithms that can be applied to PC-MRI data post -collection to deal with the velocity aliasing/phase wrapping problem[8].

### *4D. Velocity Noise*

As with all imaging techniques, the PC-MRI experiment is not perfect and therefore intrinsic noise is collected within k-space data. It is therefore essential to optimally select the imaging parameters of a protocol such that features of interest are drawn out (contrast) with the maximum signal-to-noise ratio attainable (SNR). The phase of noise is random and appears salt and pepper-like on a phase difference map. This salt and pepper noise phase is superimposed upon phase estimates within actual regions of interest as well (all pixel-level phase estimates contain some inherent contribution from noise). Therefore, baseline phase from inherent noise is also being accounted for when estimating velocity within a region of interest (ROI)[3]. In other words, velocity estimates from the PC-MRI experiment can never “truly” reflect actual underlying spin velocities due to noise (but can still get close enough to be deemed clinically acceptable and useful).

### *4E. Intravoxel Dephasing*

Intravoxel dephasing describes the phenomenon of spin motion on a scale smaller than the pixel-level; for example, the random diffusion of spins within a voxel during the PC-MRI experiment. Consider a voxel with a population of thousands of spins, all traveling with a unique velocity. These spins will experience various local magnetic fields and therefore a range of phase accumulations will be seen for different spins. This phase dispersion existing across the voxel itself translates to a direct attenuation in the magnitude of the net signal produced from said voxel (loss of overall spin coherence). This is problematic because the phase difference reconstruction described in the PC-MRI experiment performs poorly for pixels that exhibit low signal magnitude[4,9]. Phase estimates for pixels that exhibit low signal magnitude are corrupted by noise and this will manifest as incorrect velocity estimates in output velocity maps (as PC-MRI establishes a direct relationship between phase and velocity). Implementation of flow compensation waveforms can help suppress the influence of intravoxel dephasing effects as both $M_0$ and $M_1$ contributions will be nulled in such strategies[4]. However, by definition, any flow encoded acquisition will encode $M_1$ contributions and therefore will inherently contain intravoxel dephasing effects. Therefore, upon phase difference reconstruction (subtracting flow compensated and flow encoded acquisitions), intravoxel dephasing effects will nonetheless persist.

### *4F. Chemical Shift*

The chemical shift between spins in fat and water can prove to be problematic for the PC-MRI experiment. Fat and water spins resonate at slightly different precessional frequencies, which can give rise to various forms of chemical shift artifact. Recall in MRI that spatial encoding gradients establish a direct relationship between precessional frequency and spatial position. When chemical shift occurs, it confounds this direct relationship. Fat and water spins originally from separate voxels can potentially be mis-registered to the same voxel (type I chemical shift). In type I chemical shift, the signal from the voxel of interest will now be a net sum of two originally separate voxels, and therefore yield an altered magnitude and phase. Recall that phase data fidelity is a necessary requirement to accurately estimate underlying velocity, and therefore chemical shift artifacts must be accounted for. Notably, these artifacts do not precisely cancel in phase difference signal processing.

In addition, it is possible to select an echo time such that fat and water spins within the same voxel itself are completely out of phase with another (type II chemical shift). This can attenuate signal produced from said voxel and will therefore also corrupt phase estimates themselves (as phase cannot be estimated reliably when there is low signal magnitude). Selection of a TE such that water and fat spins are constructively in-phase with each other can help avoid the above described scenario and reduce the severity of type II chemical shift artifact[4]. Chemical shift artifacts can also be mitigated by controlling the readout bandwidth of the protocol[4] or by implementing spectral selective excitation strategies combined with gradient spoiling.

### *4G. Gradient-Attributed Phase Errors*

Within the PC-MRI experiment, there is a class of errors that are attributed to the gradient waveforms themselves. The application of gradient waveforms can in-turn produce magnetic fields which detract from overall $B_0$ homogeneity within the scanner. Recall in MRI, anytime the local magnetic field is altered, spins specific to that location will now precess at an altered precessional frequency (via the Larmor relationship). Therefore, spins will accumulate "extra", net phase due to these gradient-attributed errors themselves and this will manifest as erroneous velocity estimates (as PC-MRI creates a direct relationship between measured phase and estimated velocity).

Gradient-attributed phase errors appear as spatially varying phase offsets across the field-of-view of a phase difference image, and these offsets become more pronounced as distance from isocenter is increased[3,10]. Gradient-attributed phase errors result in either over or under-estimation of true phase values at a given location. Maxwell terms and eddy current effects are specific examples of gradient-attributed phase errors that must be accounted for in PC-MRI prior to velocity estimation.

It is essential to realize that these errors are created by time-variant deviations to the main $B_0$ field. Because these effects are time-variant and highly specific to the gradient waveforms that produced them, it cannot be assumed that the gradient-attributed phase deviations created by the two independent acquisitions necessary for PC-MRI will be inherently equal[3]. Therefore, the phase deviations attributed to the gradient waveforms themselves will persist even after phase difference reconstruction steps are applied. This is mathematically shown below: consider the signal phase at echo formation for two independent flow encoded acquisitions, now with gradient-attributed phase error terms included ($\phi_{error}$).

$$\vec{\phi}_A(r, t = TE) = \phi_{background} + \gamma v_0 \cdot \vec{M}_{1A} + \phi_{error_A}$$ **Eq 1.11**

$$\vec{\phi}_B(r, t = TE) = \phi_{background} + \gamma v_0 \cdot \vec{M}_{1B} + \phi_{error_B}$$ **Eq 1.12**

Note that the $\phi_{background}$ term is equivalent between independent acquisitions A and B as this term is created by time-invariant deviations to the $B_0$ field. However, the gradient-attributed phase terms $\phi_{error,A}$ and $\phi_{error,B}$ are by definition inherently different for each unique flow encoded acquisition. Therefore upon phase difference reconstruction, residual phase terms will persist as shown in Eq 1.13.

$$\begin{aligned} \Delta\vec{\phi}(r, t = TE) &= \vec{\phi}_A - \vec{\phi}_B \\ &= \gamma v_0 \cdot \Delta\vec{M}_1 + (\phi_{error_A} - \phi_{error_B}) \\ &= \gamma v_0 \cdot \Delta\vec{M}_1 + \Delta\phi_{error} \end{aligned}$$ **Eq 1.13**

It is now clearly shown that the residual gradient-attributed phase error term confounds the direct relationship between measured signal phase and underlying spin velocity "$v_0$" sought after in phase difference maps. This will lead to erroneous velocity estimates if not carefully accounted for. Development of robust and efficient methods to account for these gradient-attributed phase error effects will directly improve the clinical usefulness of the PC-MRI technique as a whole.

Correction for gradient-attributed phase errors will be the central focus for the remainder of this work.

## 5. References

1. Turski, Patrick, et al. "Neurovascular 4DFlow MRI (Phase Contrast MRA): emerging clinical applications." *BioMed Central*, Neurovascular Imaging, 22 Apr. 2016, nvijournal.biomedcentral.com/articles/10.1186/s40809-016-0019-0.

2. Lorenz, R, et al. "Influence of eddy current, Maxwell and gradient field corrections on 3D flow visualization of 3D CINE PC-MRI data." *PubMed*, Magnetic resonance in medicine., July 2014, www.ncbi.nlm.nih.gov/pubmed/24006013.

3. Markl, Michael. *Velocity Encoding and Flow Imaging*. University Hospital Freiburg, Dept. of Diagnostic Radiology, Medical Physics, Freiburg, Germany, Jan. 2005, ee-classes.usc.edu/ee591/library/Markl-FlowImaging.pdf.

4. Nayak, Krishna S., et al. "Cardiovascular magnetic resonance phase contrast imaging." *Journal of Cardiovascular Magnetic Resonance*, BioMed Central, 9 Aug. 2015, jcmr-online.biomedcentral.com/articles/10.1186/s12968-015-0172-7.

5. Stankovic, Zoran, et al. "4D flow imaging with MRI." *PubMed*, Cardiovascular Diagnosis and Therapy, Apr. 2014, www.ncbi.nlm.nih.gov/pmc/articles/PMC3996243/.

6. Stalder, A F, et al. "Quantitative 2D and 3D phase contrast MRI: optimized analysis of blood flow and vessel wall parameters." *PubMed*, Magnetic resonance in medicine., Nov. 2008, www.ncbi.nlm.nih.gov/pubmed/18956416.

7. Bauer, S, et al. "K-t GRAPPA accelerated phase contrast MRI: Improved assessment of blood flow and 3-Directional myocardial motion during breath-Hold." *PubMed*, Journal of magnetic resonance imaging : JMRI., Nov. 2013, www.ncbi.nlm.nih.gov/pubmed/23908094.

8. Espe, E K, et al. "Unwrapping eddy current compensation: improved compensation of eddy current induced baseline shifts in high-Resolution phase-Contrast MRI at 9.4 Tesla." *PubMed*, Magnetic resonance in medicine., Oct. 2014, www.ncbi.nlm.nih.gov/pubmed/24264935.

9. Pelc, N J, et al. "Phase contrast cine magnetic resonance imaging." *PubMed*, Magnetic Resonance Quarterly, Oct. 1991, www.ncbi.nlm.nih.gov/pubmed/1790111.

10. Bernstein, Matt A, et al. "Chapter 15.2: Phase Contrast." *Handbook of MRI Pulse Sequences*, 1st ed., Elsevier Academic Press, 2004, pp. 659–678

# Chapter II: Gradient Attributed Phase Errors

## 1. Overview

As outlined in the previous chapter, the goal of a PC-MRI experiment is to establish a direct relationship between measured signal phase and underlying spin velocity itself. Therefore, an essential requirement for the PC-MRI experiment is to ensure that all other contributions to measured signal phase are negligible. This includes minimizing phase contributions from time-invariant background offsets, stationary spins, accelerating or higher order spins, and any erroneous phase contributions from the application of gradient waveforms themselves (gradient attributed phase errors). The focus of this chapter itself and a central theme of this entire work will be defining, characterizing, and correcting for gradient attributed phase errors within PC-MRI.

Gradients impart phase upon a spin system by altering the local magnetic field that this system experiences and thus changing a spin system's precessional frequency. A gradient attributed phase error is therefore any offset from "true" or "expected" phase values due to the application of the gradients themselves. Gradient attributed phase errors manifest as spatially varying phase offsets across the field-of-view (FOV) of phase difference maps[1]. These phase offsets typically increase in severity with distance from isocenter, and these phase offsets can result in either over or under-estimation of true phase values at a particular location.

There are a few different classes of gradient attributed phase errors within MRI. Each type of gradient attributed phase error originates from fundamentally different phenomena; however, all gradient attributed phase errors will still manifest as spatially varying phase offsets across a FOV. Different classes of gradient attributed phase errors will now be individually discussed.

## 2. Maxwell Phase Error

In MRI, gradients are magnetic fields designed to have a linear variation in local field strength along the x,y, and/or z spatial dimensions. In addition, the gradient magnetic fields are theoretically designed to be oriented along the z-axis alone (therefore gradient magnetic fields should only contain a $B_z$ magnetic field component, with no $B_x$ or $B_y$ components present).

However in actuality, the application of a $B_z$ oriented gradient is always accompanied by an orthogonal $B_x$ and/or $B_y$ field. This phenomenon can be described and shown using Maxwell's equations. The effect of this Maxwell phenomena results in a shift of the overall B field from being solely oriented along the z-axis (overall B field will now have x and/or y components) and also creates a higher order field strength spatial dependence within the overall B field itself ($x^2$ or $y^2$ spatial dependence)[2]. The magnetic field produced by higher order Maxwell terms is known as the "concomitant field". This concomitant field imparts extra, spatially and temporally dependent phase onto a spin system and thus results in erroneous phase offsets. These Maxwell phase errors are directly due to the presence of concomitant magnetic fields produced by applied gradients and can therefore be considered a "gradient attributed phase error".

The strength of the concomitant field at any specific location can be analytically calculated for a known gradient waveform using Maxwell's equations, and therefore serves as a basis for correction[2]. The following mathematical derivation to describe the concomitant field and this field's contribution to Maxwell phase error is detailed in Bernstein's MRI Pulse Sequences handbook.

Maxwell's equations dictates that any given magnetic field, B, must satisfy the following two conditions, named the divergence equation and the curl equation respectively:

Condition A. $\nabla \bullet B = 0$

Condition B. $(1/u_0) \nabla \times B = e_0 (\partial E/\partial t) + J$

Under the conditions of negligible displacement current density and real current density, the curl equation simplifies to as follows:

Condition A. $\nabla \bullet B = 0$

Condition B. $\nabla \times B = 0$

Expansion of the $\nabla$ operator within Maxwell's simplified conditions produces:

Condition A. $< \partial/\partial x , \partial/\partial y , \partial/\partial z > \bullet < B_x , B_y , B_z > = 0$

Condition B. $< \partial/\partial x , \partial/\partial y , \partial/\partial z > \times < B_x , B_y , B_z > = 0$

Thus yielding the overall scalar relationships:

1. $(\partial B_x/\partial x) + (\partial B_y/\partial y) + (\partial B_z/\partial z) = 0$
2. $\partial B_z/\partial y = \partial B_y/\partial z$
3. $\partial B_x/\partial z = \partial B_z/\partial x$
4. $\partial B_y/\partial x = \partial B_x/\partial y$

*Where: $B_x$, $B_y$, and $B_z$ are vector components of the overall magnetic field, T*

Applied gradients in MRI are by definition: $\partial B_z/\partial x = G_x$, $\partial B_z/\partial y = G_y$, & $\partial B_z/\partial z = G_z$. Additional parameters can be defined as follows to simplify further analysis:

$\alpha = (-1/G_z)(\partial B_x/\partial x)$ *dimensionless parameter*

$G_\perp = \partial Bx/\partial y = \partial B_y/\partial x$ *transverse gradient term*

The Jacobian, describing spatial dependence of the overall magnetic field, can now be expressed as follows:

$$\begin{bmatrix} \frac{\partial B_x}{\partial x} & \frac{\partial B_x}{\partial y} & \frac{\partial B_x}{\partial z} \\ \frac{\partial B_y}{\partial x} & \frac{\partial B_y}{\partial y} & \frac{\partial B_y}{\partial z} \\ \frac{\partial B_z}{\partial x} & \frac{\partial B_z}{\partial y} & \frac{\partial B_z}{\partial z} \end{bmatrix} = \begin{bmatrix} -\alpha G_z & G_\perp & G_x \\ G_\perp & (\alpha - 1)G_z & G_y \\ G_x & G_y & G_z \end{bmatrix}$$

Therefore, the magnetic field's vector components at any particular location can be calculated using Eq 2.1 in matrix form:

$$\begin{bmatrix} B_x \\ B_y \\ B_z - B_0 \end{bmatrix} = \begin{bmatrix} \frac{\partial B_x}{\partial x} & \frac{\partial B_x}{\partial y} & \frac{\partial B_x}{\partial z} \\ \frac{\partial B_y}{\partial x} & \frac{\partial B_y}{\partial y} & \frac{\partial B_y}{\partial z} \\ \frac{\partial B_z}{\partial x} & \frac{\partial B_z}{\partial y} & \frac{\partial B_z}{\partial z} \end{bmatrix} \begin{bmatrix} x \\ y \\ z \end{bmatrix}$$

$$= \begin{bmatrix} -\alpha G_z & G_\perp & G_x \\ G_\perp & (\alpha - 1)G_z & G_y \\ G_x & G_y & G_z \end{bmatrix} \begin{bmatrix} x \\ y \\ z \end{bmatrix} \qquad \textbf{Eq 2.1}$$

Note that $B_x$ and $B_y$ field components may be nonzero, and therefore the overall B-field may not be solely oriented along the z-axis. The overall B-field may not align along the z-axis despite the fact that applied gradients ($G_x$, $G_y$, and $G_z$) and the static $B_0$ field are all aligned along the z-axis themselves.

The overall amplitude of the magnetic field at the specified location of interest is now estimated by Eq 2.2 as follows:

$$B(x,y,z) = [\ (B_x)^2 + (B_y)^2 + (B_z)^2\ ]^{1/2} \qquad \textbf{Eq 2.2}$$

Taylor series expansion of Eq 2.2 and the assumption of cylindrical gradient coils yields Eq 2.3:

$$
\begin{aligned}
B &= B_0 + G_x x + G_y y + G_z z + \\
&\frac{1}{2 * B_0}\left[\frac{G_z^2}{4}(x^2 + y^2) + (G_x^2 + G_y^2)z^2 - G_x G_z xz - G_y G_z yz\right] \\
&= B_0 + \vec{G} \cdot \vec{r} + B_c
\end{aligned}
\qquad \textbf{Eq 2.3}
$$

*Where:* - $G = <G_x, G_y, G_z>$ *, T/m*
-$r = <x, y, z>$ *, m*
- $B_c$ *= concomitant magnetic field , T*

Rearrangement of terms allows the concomitant field, $B_c$ , to be described by Eq 2.4:

$$
B_c = \frac{1}{2B_0}\left[\left(G_x z - \frac{G_z x}{2}\right)^2 + \left(G_y z - \frac{G_z y}{2}\right)^2\right] \geq 0 \qquad \textbf{Eq 2.4}
$$

Note that $B_c$ is a non-negative function of the parameters $G_x$, $G_y$, $G_z$, x, y, and z. Therefore, the local strength of the concomitant magnetic field, $B_c$, depends upon the applied gradient waveforms and the spatial location of interest within the scanner.

With the concomitant field ($B_c$) mathematically described, Maxwell phase error ($\phi_c$) can now be estimated using Eq 2.5:

$$\phi_c(x,y,z) = \Upsilon \int B_c(G_x, G_y, G_z, x, y, z)\ dt \qquad \textbf{Eq 2.5}$$

*Where:* $\Upsilon$ *is the gyromagnetic ratio of the species being imaged, rad/s•T*
*- G =* $<G_x, G_y, G_z>$ *= applied gradients , T/m*
*- r = <x,y,z> = position vector, m*

It can be directly seen from Eq 2.1 that the concomitant field can only exist when gradient waveforms are being played. The concomitant field instantaneously becomes non-existent when gradients are not active; therefore, this field will no longer contribute to phase when applied gradients are inactivated[2].

Recall an essential requirement of the PC-MRI experiment is implementing non-identical flow encoding gradients between independent acquisitions, thereby creating differing concomitant fields between each acquisition. Maxwell phase errors between acquisitions will therefore not perfectly cancel out upon implementing traditional phase difference reconstruction, and these errors will confound the direct relationship between measured phase and underlying spin velocity that is sought after within PC-MRI. However, knowledge of Maxwell phase error ($\phi_c$) on the pixel level can be incorporated within a modified phase difference reconstruction scheme in PC-MRI to correct for concomitant field effects.

Consider two complex images that are formed from the independent acquisitions necessary for PC-MRI. One can define the complex value corresponding to a particular pixel of interest (for each image) by its corresponding real and imaginary components:

First Image: $Z_1$ = real + i(imaginary) = $x_1 + i(y_1) = p_1 e^{i\phi 1}$
Second Image: $Z_2$ = real + i(imaginary) = $x_2 + i(y_2) = p_2 e^{i\phi 2}$

Calculation of the phase difference specific to this pixel of interest, assuming no concomitant field effects exist, is as follows:

$$\Delta\phi = \phi_1 - \phi_2$$

$$= \arg (Z_1 , Z_2^*)$$

$$= \arctan (\text{ imaginary}(Z_1 \; Z_2^*) / \text{real}(Z_1 \; Z_2^*) )$$

$$= \arctan ( (x_2y_1 - x_1y_2) / ( x_1x_2 + y_1y_2) )$$

*Where: * = complex conjugate of a complex vector*

This traditional phase difference calculation can be easily modified to now account for pixel-level concomitant field effects ($\phi_{c,1}$ and $\phi_{c,2}$) as follows:

$$\Delta\phi = ( \phi_1 + \phi_{c,1} ) - ( \phi_2 + \phi_{c,2} )$$

$$= ( \phi_1 - \phi_2 ) + \Delta\phi_c$$

$$= \arg (Z_1 \; Z_2^* \; e^{-i\Delta\phi c})$$

$$= \arctan ( \text{ imaginary}(Z_1 \; Z_2^* \; e^{-i\Delta\phi c}) / \text{real}(Z_1 \; Z_2^* \; e^{-i\Delta\phi c}) )$$

Note that demodulation by Maxwell Phase contributions is performed on a pixel level prior to using the arctangent operator. Therefore, the output phase difference estimate for a particular pixel of interest within this modified reconstruction framework will now be free of Maxwell phase errors and will thus more closely reflect "true" underlying phase values.

Other Maxwell phase error compensation techniques include both hardware and pulse sequence based approaches[2]. The Maxwell phase error phenomenon is well documented within PC-MRI and its analytical correction (as outlined above) is considered the "gold standard". As a result, this specific class of gradient attributed phase error is considered a "solved" problem and will therefore not be a central theme for the remainder of this work. Further discussions of gradient attributed phase errors will be limited to the eddy current phenomena itself.

## 3. Eddy Current Phase Error

Another class of gradient attributed phase errors is due to the eddy current phenomenon. In order to understand the source of eddy currents themselves, consider Faraday's law of induction. Faraday's law of induction (Eq 2.6) states that any magnetic field oriented through a loop of wire (such as the many coils present within a MRI scanner) will induce a magnetic flux.

$$\varphi_B = \int_\Sigma B \bullet dA \qquad \textbf{Eq 2.6}$$

*Where:* -$\varphi_B$ *= magnetic flux , Wb*
- $B$ *= overall magnetic field , T*
-$\Sigma$ *= surface enclosed by the loop of wire*
-$dA$ *= infinitesimal element of surface* $\Sigma$ *,* $m^2$
$\bullet$ *= dot product operator.*

It is also known that a changing magnetic flux will induce an electromotive potential, $\varepsilon$ , as shown in Eq 2.7:

$$\varepsilon_{\text{induced}} = - \partial\varphi_B / \partial t = - \int_\Sigma \partial B/\partial t \bullet dA \qquad \textbf{Eq 2.7}$$

From Eq 2.7, it can clearly be seen that any time varying magnetic field ($\partial B/\partial t$) will contribute to a changing magnetic flux through nearby conducting structures (such as a coil or loop of wire). This changing magnetic flux will in-turn induce an electromotive potential within said conducting structure, resulting in the formation of an “eddy” current within the conducting structure itself (Ohm’s law). This current will lead to the generation of an eddy current associated magnetic field that, according to Lenz’s Law, opposes the applied B-field. This inductance phenomenon can be modeled and summarized using LR circuit theory as follows in Figure 2.1:

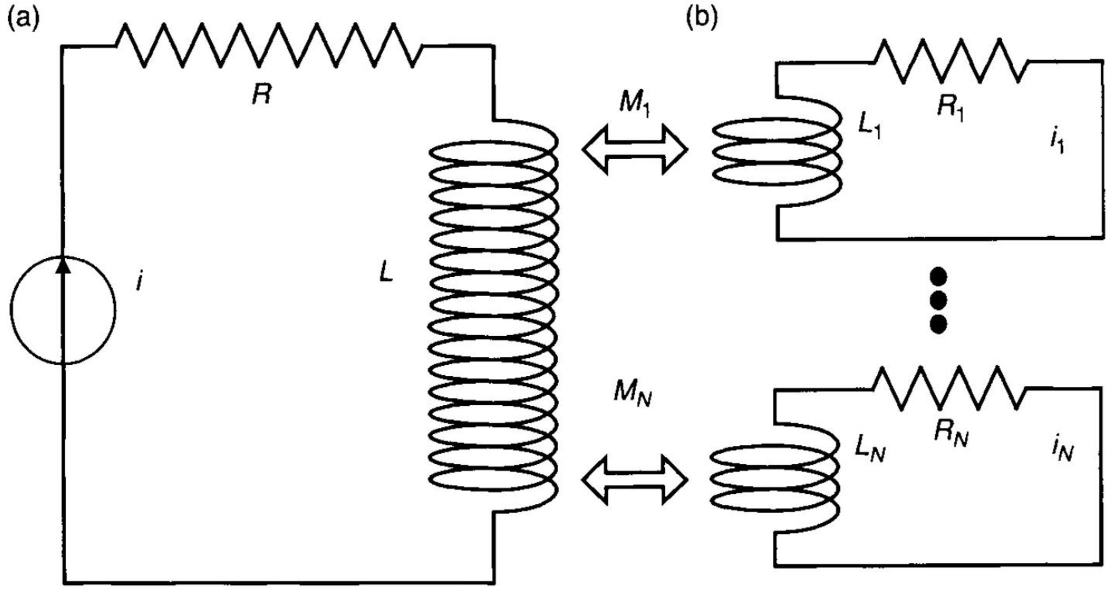

***Figure 2.1**. LR circuits modeling the eddy current phenomenon. (a) gradient coil modeled as resistor (R)–capacitor (L) circuit. Input current (i) generates gradient slew. (b) Conducting structures within a MRI scanner modeled as LR circuits. Upon gradient slew, mutual inductance ($M_N$) between the gradient coils and conducting structures generates eddy currents ($I_N$) within said conducting structures. These eddy currents induce magnetic fields that alter the B-field. Figure taken from Bernstein's MRI Pulse Sequence's handbook[2].*

In MRI, applied gradients are by definition time changing magnetic fields (during gradient slew) and will therefore contribute to the described eddy current phenomenon. Consider a gradient coil modeled as a LR circuit (Figure 2.1a). When input current is generated within this gradient coil, a gradient magnetic field will be produced. During any time-varying portions of the produced gradient waveform, mutual inductance ($M_n$) between the gradient coil (a) and nearby conducting structures (b) will generate eddy currents within said conducting structures. These eddy currents are denoted by $i_1$, $i_2$, … $i_N$ in part (b) of the above model. According to source-free LR circuit theory, the individual eddy currents, $i_N$, within the conducting structures can be modeled by Eq 2.8 as follows:

$$i_N(t) = i_0 \bullet e^{-Rt/L} \qquad \textbf{Eq 2.8}$$

These eddy currents, now "housed" within local conducting structures inside the scanner, will in-turn induce their own magnetic fields, $B_{eddy}$ :

$$B_{eddy} \propto i_N \propto \varepsilon_{induced} \qquad \textbf{Eq 2.9}$$

These induced magnetic fields are referred to as "eddy current induced fields" because they are created by the eddy current phenomena itself. These eddy current induced fields are essential to account for as they directly alter the magnitude of the local B field. Therefore, eddy current induced fields impart extra, unwanted phase onto a spin system (Larmor relationship). This eddy current phase error thus confounds the direct relationship between measured signal phase and underlying spin velocity that is sought after within the PC-MRI experiment, manifesting as spatially and temporally dependent velocity offsets, $v_{eddy}$. These $v_{eddy}$ offsets must be specifically corrected for prior to quantitative analysis in PC-MRI. The eddy current phenomenon can be considered a "gradient attributed error" as the application of gradient waveforms themselves will produce the eddy current induced field.

Note that the sign of Eq 2.7 indicates that the induced eddy currents will oppose the changing magnetic flux that produced them (Len's law). In other words, the eddy current induced field will always oppose the changing magnetic field which first produced it[2]. This attribute pertaining to the eddy current induced field is well illustrated in the following trapezoidal gradient waveform example:

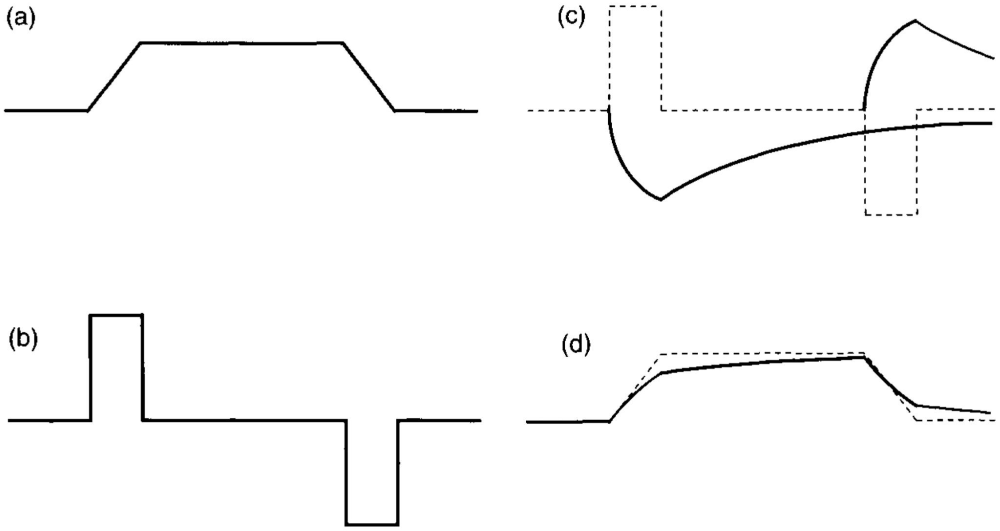

***Figure 2.2*** *Effects of eddy current induced fields on applied gradient waveforms. (a) Original applied gradient waveform on an arbitrary gradient axis. (b) dG/dt waveform – eddy current excitation waveform. Intervals of gradient slew induce unique eddy current fields. (c) Eddy current induced fields. Individual eddy current induced fields decay over time, characterized by unique time constants. The fields induced by separate intervals of gradient slew and the B-field undergo superposition. (d) Eddy current distorted gradient waveform. Superposition of eddy current induced fields results in distortion of intended gradient waveforms. Figure taken from Bernstein's MRI Pulse Sequences handbook*[2]*.*

Consider an ideal applied gradient waveform on a single axis that is trapezoidal in nature as in (a) of Figure 2.2. The eddy current induced fields created by the ramp up and ramp down sections of this applied gradient waveform can be considered independently. The ramp up section of this waveform will create a positive field change, and thus induce an eddy current field that is opposing this change as seen in the corresponding portion of (c). This eddy current induced field will then begin to decay during the constant amplitude portion of the applied gradient waveform (when no gradient slew is observed). The ramp down section of the applied gradient waveform will create a negative field change, and thus induce a new eddy current field that is positive in nature. The net observed gradient waveform will be described by the superposition of both eddy current induced fields and the original applied gradient waveform. The net observed waveform is distorted from its original shape due to the eddy current phenomena and is therefore referred to as an “eddy current distorted gradient waveform” (d). Note that this example displays only the effects of “on-axis” eddy current induced fields, or induced fields oriented in the same direction as the applied gradient that originally produced them. However, applied gradients also induce “cross-term” eddy fields, or fields that are oriented in an orthogonal direction to the applied gradient that produced them[4]. These cross-term eddy fields are in essence Maxwell fields. The phase effects of both on-axis and cross-term eddy current induced fields must be accounted for.

The amount of eddy current phase error that is accrued at a particular spatial location depends upon the local strength of the overall eddy current induced field at that same location. The local strength of the eddy current induced field depends complexly upon many parameters, and therefore no analytical solution describing this overall induced field has been proposed (unlike concomitant fields). For example: distance from the conducting structure(s) that “housed” the original eddy currents, applied gradient slew rates, maximum gradient amplitudes, and geometry of the conducting structure(s) itself can all influence the resulting local field strength of the eddy current induced field[5]. However, a general temporal and spatial dependence has been shown to be associated with these errors[2]:

### *3A. Temporal dependence*

As previously described, any changing magnetic field will produce eddy current induced fields within the scanner. Therefore, the eddy current induced field will be produced during any ramp up or ramp down portion of a given gradient waveform (during gradient slew). During constant amplitude portions of applied gradient waveforms, no changing magnetic flux will be induced within conducting structures and therefore eddy currents will begin to decay within said structures. As a result, the eddy current induced field itself and its effects on phase will become less pronounced during time intervals where no changing magnetic field is present[2]. This clear time dependence within the eddy current phenomenon is also demonstrated by the decaying natures of Eq 2.8 and Eq 2.9. However, it is essential to note that eddy current phase offsets will still aggregate when gradient slew is not observed, as the eddy current induced field itself has not yet completely decayed and is thus still able to impart unwanted phase (depending on the eddy current time constants). This is in direct contrast with Maxwell phase errors, as Maxwell phase errors will not aggregate during time intervals when the concomitant field is no longer present (intervals when gradients are no longer applied). Under source-free LR circuit theory, the temporal dependence of the eddy current induced field, $B_{eddy}$, can be modeled by Eq 2.10 as follows[2,3]:

$$B_{eddy}(t) = -dG/dt * e_N(t) \qquad \textbf{Eq 2.10}$$

$$= -dG/dt * [\, H(t) \sum \alpha_N \, e^{-t/\tau} \,]$$

*Where:* $*$ *= convolution operator*
- $G$ *= applied gradient waveforms* $\langle G_x, G_y, G_z \rangle$ *, T/m*
- $H(t)$ *= unit step function*
- $e_N(t)$ *= eddy current impulse responses*
- $\tau_N$ *= time constant, ms*
- $\alpha_N$ *= amplitude coefficient*

According to Eq 2.10, characterization of the impulse responses of induced eddy currents, $e_N(t)$, is necessary for modeling the temporal dependence within the overall eddy current induced field, $B_{eddy}$, itself. These impulse responses describe the effects of both on-axis and cross-term eddy current induced fields[5]. Each individual impulse response is characterized by a unique time constant ($\tau_N$) and amplitude ($\alpha_N$) which describe the rate of exponential growth and decay of the specific field after inductance[2]. Note, that the system may be best described by several time constants. Certain correction methods aim to measure these eddy current impulse response time constants and amplitudes as a basis for correction. Various eddy current correction techniques will be discussed in detail within the final section of this chapter.

### *3B. Spatial dependence*

Consider the z-component of an eddy current induced field, $B_{e,z}$. Upon Taylor series expansion, $B_{e,z}$ can be spatially modeled along the three physical axes of the scanner as follows in Eq 2.11:

$$B_{e,z}(r,t) = B_{0,e}(t) + r \bullet B_{1,e}(t) + \ldots$$ **Eq 2.11**

*Where:* - $B_{0,e}$ = *zero order eddy current term, T*
- $r$ = *position vector* $<x,y,z>$ *, m*
- $B_{1,e}$ = *first order (spatially linear) eddy current term, T/m*

Incorporation of the LR circuit model describing temporal dependence into the above Taylor expansion will yield Eq 2.12:

$$B_{e,z}(r,t) = [\, - dG/dt * e_0(t)\,] + r\ [- dG/dt * e_1(t)\,] + \ldots$$ **Eq 2.12**

*Where:* $*$ = *convolution operator*
-$G$ = *applied gradient waveforms* $<G_x, G_y, G_z>$*, T/m*
-$e_0(t)$ = *zero order eddy current impulse responses*
-$e_1(t)$ = *first order eddy current impulse responses*

The zero order term in the above expansion is referred to as the "$B_0$ eddy current" and the first order term is referred to as the "linear eddy current". The $B_0$ eddy current field is spatially constant over the field of view (FOV) and the linear eddy current field creates a linear spatial variation across the FOV[2]. Higher order spatial dependence terms in Eq 2.11 and Eq 2.12 are not commonly observed from empirical data and are therefore generally omitted during modeling and correction[2]. It can directly be seen from Eq 2.12 that knowledge of unique eddy current time constants and amplitudes are necessary to model both the spatial and temporal dependences of the eddy current induced field, $B_{eddy}$. Measurement of these eddy current impulse responses will be discussed in the final section of this chapter.

Eddy current induced phase errors will persist following the phase difference reconstruction method implemented within PC-MRI[6]. Consider signal phase at echo formation when a bipolar, flow-encoded acquisition is implemented:

$$\begin{aligned}\vec{\phi}_A(r, t = TE) &= \phi_{background} + \gamma v_0 \cdot \vec{M}_{1A} + \gamma \int_{t=0}^{t=TE} \vec{B}_{eddy_A} \cdot dt \\ &= \phi_{background} + \gamma v_0 \cdot \vec{M}_{1A} + \phi_{eddy_A}\end{aligned}$$ **Eq. 2.13**

Note that intervals of gradient slew within the flow-encoding gradient waveform will generate eddy current induced fields, $B_{eddy}$. These $B_{eddy}$ fields impart extra, unwanted phase upon spin systems ($\phi_{eddy}$). Recall in PC-MRI, independent acquisitions with unique encoded $M_1$ moments are necessary to directly relate signal phase to spin velocity. Consider the signal phase at echo formation when a different bipolar, flow-encoded acquisition is implemented:

$$\begin{aligned}\vec{\phi}_B(r, t = TE) &= \phi_{background} + \gamma v_0 \cdot \vec{M}_{1B} + \gamma \int_{t=0}^{t=TE} \vec{B}_{eddy_B} \cdot dt \\ &= \phi_{background} + \gamma v_0 \cdot \vec{M}_{1B} + \phi_{eddy_B}\end{aligned}$$ **Eq 2.14**

The $B_{eddy}$ fields induced by this new flow-encoded acquisition are also unique. Therefore, residual phase terms will persist upon phase difference reconstruction:

$$\Delta\vec{\phi}(r, t = TE) = \vec{\phi}_A - \vec{\phi}_B$$

$$= (\phi_{background} + \gamma v_0 \cdot \vec{M}_{1A} + \gamma \int_{t=0}^{t=TE} \vec{B}_{eddy_A} \cdot dt) -$$

$$(\phi_{background} + \gamma v_0 \cdot \vec{M}_{1B} + \gamma \int_{t=0}^{t=TE} \vec{B}_{eddy_B} \cdot dt)$$

$$= (\phi_{background} + \gamma v_0 \cdot \vec{M}_{1A} + \phi_{eddy_A}) -$$
$$(\phi_{background} + \gamma v_0 \cdot \vec{M}_{1B} + \phi_{eddy_B})$$

$$= \gamma v_0 \cdot \Delta\vec{M}_1 + \Delta\phi_{eddy} \qquad \textbf{Eq 2.15}$$

These residual eddy current phase terms ($\Delta\varphi_{eddy}$) confound the direct relationship between signal phase and spin velocity established within PC-MRI; and thus result in $v_{eddy}$ errors when estimating velocity. These $v_{eddy}$ errors in velocity estimates must be corrected for prior to quantitative analysis. It is important to note that unlike Maxwell errors, no overall analytical solution describing eddy current phase exists and therefore a modified phase difference reconstruction cannot be implemented to account for this specific class of phase error. The primary theme for the remainder of this work will be correcting for eddy current induced phase errors within PC-MRI.

## 4. Gradient Attributed Error Magnitudes

Quantitative analysis of velocity maps generated in PC-MRI suffers from inaccuracies due to gradient attributed phase errors. Velocity maps will contain offsets due to both Maxwell phase errors and eddy current phase errors, and these errors must be corrected for prior to analysis. Maxwell phase errors are considered negligible when incorporating their analytical solution during reconstruction as outlined previously. However, it is important to note that these Maxwell phase errors are very significant when left uncorrected. From Eq 2.4, it can directly be seen that the strength of the concomitant field varies inversely with main field strength and is directly proportional to applied gradient amplitudes. Therefore, Maxwell phase error will become significant when performing imaging experiments on low field strength scanners with high performance gradient waveforms. In these scenarios, the concomitant field is significant and has been shown to result in magnetic field inhomogeneities on the order of ten parts per million[2]. Maxwell errors resulting from these field inhomogeneities have been shown to cause geometric distortions, image shifts, ghosting, intensity losses, blurring, shading, and velocity errors within examinations, dependent upon intended application[2].

Eddy current artifacts increase in severity with gradient slew rate and/or applied gradient amplitude and therefore must be considered when implementing any sequences with high performance gradients[2]. The magnitude of the eddy current phase error itself has been shown to be both parameter and application dependent. A multi-center, multi-vendor study was conducted by Gatehouse et al. to assess the magnitude of eddy current error within clinical PC-MRI examinations. Through-plane acquisitions, similar to ones used clinically for aortic and pulmonary flow measurement, were applied to static phantoms at 1.5 T with a VENC of 150 cm/s. ROIs characteristic of the size of great vessels (~30 mm diameter) were prescribed within the static phantom at locations up to 70 mm off isocenter. Velocity offsets as large as 4.9 cm/s were observed within static tissue and an average offset of 2.7 cm/s was calculated across all ROIs. By theoretical calculation, this study asserted that a velocity offset of simply 0.6 cm/s would propagate and result in 5% miscalculation in cardiac output and up to 10% miscalculation in shunt flow measurement[7]. Other studies have reported eddy current phase errors to be as large as 10 to 25% for cardiac applications and smaller in magnitude for neurological applications[8]. A likely reason for this observed trend is that vessels being quantitatively analyzed in cardiac applications tend to be located farther from isocenter within a larger FOV, and therefore eddy current influence will be more prominent.

Suppose volumetric flow estimates within a single blood vessel are of interest. A time-resolved PC-MRI experiment where through-plane flow is being encoded within a thin slice perpendicular to this blood vessel of interest can be used to assess flow. The velocity profile, $v_i(t)$, for a single pixel within the blood vessel lumen can be plotted over different acquired temporal phases as shown in Figure 2.3:

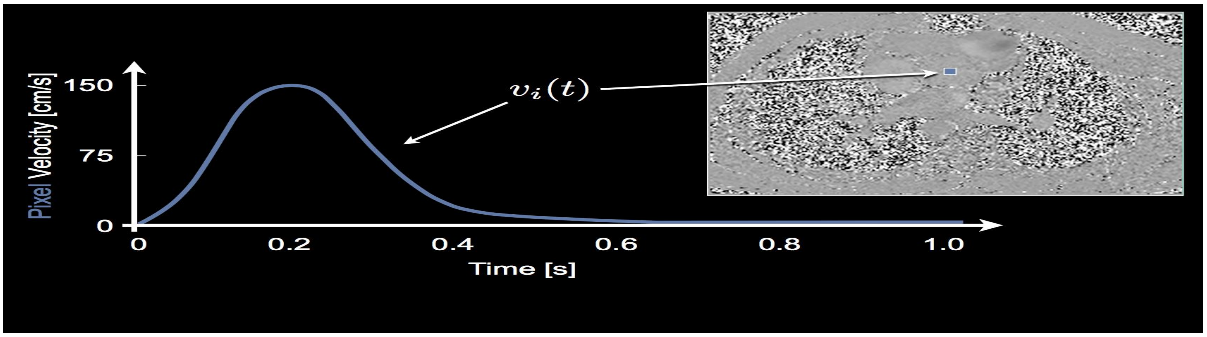

***Figure 2.3.*** *Velocity profile (over time) within a single pixel of a vessel lumen. Through-plane flow is being measured.*

This pixel velocity profile will contain an inherent velocity bias/offset due to eddy currents themselves, as described by the $v_{eddy}$ term in Figure 2.4 below:

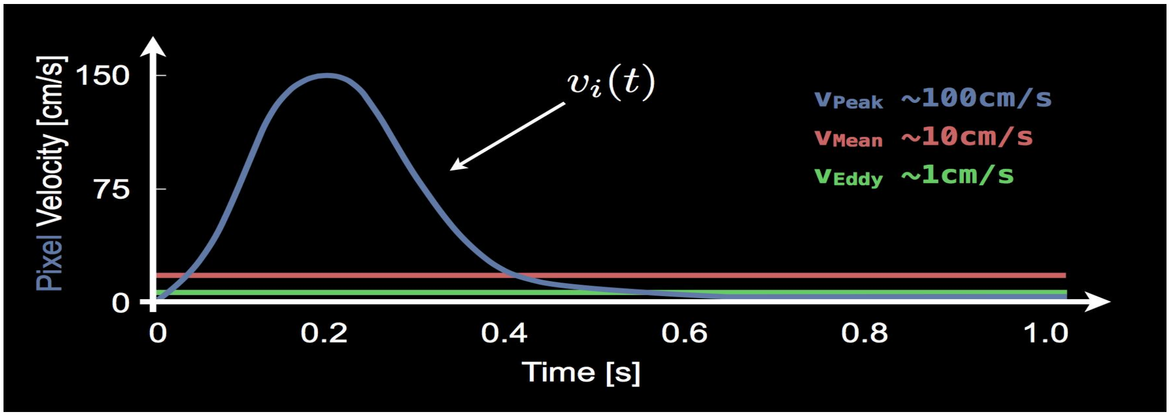

***Figure 2.4***. *Velocity profile influenced by eddy current offset. Estimates of mean, max, and total flow from a single pixel within a vessel lumen are all affected by eddy current offset.*

From Figure 2.4 it can be seen that eddy current offsets affect the estimation of mean velocity (over time) within a specific pixel of interest. A larger eddy current offset will more drastically affect mean pixel velocity calculation. In the above scenario, mean pixel velocity is being overestimated due to eddy currents. Estimation of peak velocity within this pixel is also compromised by eddy current offset. However, estimation of total volumetric flow will most severely be influenced by the eddy current phenomenon. Total volumetric flow within a pixel, free of eddy current offset, can be calculated by Eq 2.16 as follows:

$$Q_i = \int v_i(t) \bullet a_i \, dt \qquad \textbf{Eq 2.16}$$

*Where:* - $Q_i$ *= total volumetric flow, mL*
- $v_i(t)$ *= pixel velocity, cm/s*
- $a_i$ *= pixel area,* $cm^2$

Under the presence of eddy current influence, total volumetric flow (within a single pixel) is now calculated by Eq 2.17 as follows:

$$Q_i = \int [\, v_i(t) + v_{eddy} \,] \bullet a_i \, dt \qquad \textbf{Eq 2.17}$$

Eq 2.17 can then be expanded to describe total volumetric flow within an entire set of pixels or region of interest (ROI) as follows:

$$Q_{ROI} = \int \left( \sum [\, v_i(t) + v_{eddy} \,] \bullet a_i \right) dt \qquad \textbf{Eq 2.18}$$

*Where:* - $Q_{ROI}$ *= total volumetric flow, mL*
- $v_i(t)$ *= pixel velocity, cm/s*
- $v_{eddy}$ *= pixel level eddy current offset, cm/s*
- $a_i$ *= pixel area,* $cm^2$
-$\sum$ *= summation over all pixels within an ROI*

From Eq 2.18, it can directly be seen that eddy currents will drastically affect total volumetric flow estimates within an ROI as these errors will aggregate over both time and space[1,7]. Pixel velocity estimates at any instance in time will be offset by eddy currents, and these errors will aggregate upon integration over different temporal phases and once again upon summation with total flow estimates from other pixels within the ROI. Eddy current offsets have also been reported to affect the calculation of other clinical parameters derived from velocity information within PC-MRI, such as vessel wall shear stress calculations, flow vorticity estimates, calculated pressure gradients, and 3D streamline visualizations[1]. Accuracy in calculated parameters describing flow is essential for the proper diagnosis, assessment, and risk stratification of various cardiovascular and neurological pathologies.

## 5. Eddy Current Compensation Techniques

Unlike Maxwell phase errors, eddy current phase errors have no accepted "gold standard" correction method. As a result, a variety of correction techniques are usually simultaneously implemented within an experiment in hopes of reducing the magnitude of the eddy current error down to acceptable levels for quantitative analysis. Commonly implemented eddy current correction strategies and inherent limitations associated with these correction strategies will now be discussed. A detailed description for each of these correction strategies can be found in Bernstein's MRI Pulse Sequences handbook.

### *5A. Coil Shielding*

As previously mentioned, mutual inductance between the gradient coils and nearby conducting structures within the MRI scanner is responsible for the eddy current phenomena. Gradient coils within a scanner are designed to enclose the imaging volume. The conducting structures that contribute to the eddy current phenomena are typically farther radially than the gradient coils themselves, and are thus located towards the fringes of the scanner. Therefore, minimizing the gradient magnetic field that exists outside the imaging volume (enclosed by the gradient coils) can be an effective strategy in reducing the severity of eddy currents. Designing the gradient magnetic field to be zero outside the imaging volume prevents a changing magnetic flux to be induced within fringe conducting structures and thus prevents eddy current induction within said structures. This can be effectively accomplished by pairing each gradient coil with a corresponding “shield coil”. This shield coil is specifically designed to create a field that opposes and cancels out the gradient magnetic field at locations outside the imaging volume. Gradient coil shielding is routinely implemented within commercial scanners and has been shown to reduce eddy current amplitudes by a factor of 10 to 100 times[2].

It is important to note that the fields created by the gradient coils and the shield coils will also partially cancel out within the imaging volume itself. Therefore, scanners implementing shielded gradient configurations suffer from a direct reduction in gradient efficiency as extra input current is now required to generate the original, desired gradient field within the imaging volume itself[2].

### *5B. Gradient Waveform Modifications*

A variety of eddy current compensation techniques aim to modify the applied gradient waveforms themselves in order to minimize the severity of induced eddy current fields. As mentioned before, eddy currents are induced within conducting structures within the scanner during time varying portions of applied gradient waveforms. Therefore, limiting the amount of eddy current build up during these ramp up or ramp down portions of applied gradient waveforms can be an effective strategy in minimizing overall eddy current phase error. One method of limiting eddy current buildup is by minimizing applied gradient slew rates, as slew rate is proportional to current buildup rate[2]. Additionally, minimizing applied gradient amplitudes can also limit eddy current buildup. When implementing higher gradient amplitudes with a fixed slew rate, a longer ramp up or ramp down time is inherently associated with the applied gradient waveform. Therefore in this scenario, eddy currents are given longer periods of time to build up and will hence more severely contribute to eddy current phase error. This compensation technique of adjusting the slew rate and/or maximum amplitude of applied gradient waveforms is known as "gradient waveform de-rating". Gradient waveform de-rating techniques are limited by various constraints. A low slew rate gradient waveform will a take longer time to ramp up and ramp down and will therefore cause a subsequent lengthening in the echo time (TE) of a sequence. In PC-MRI, implemented sequences are designed to exhibit a short TE and as a result, slew rate of flow-encoding waveforms can only be adjusted within reason.

Alternatively, "gradient waveform pre-emphasis" techniques can be implemented to modify applied gradient waveforms for eddy current compensation. In waveform pre-emphasis, the input current into the gradient coils is manipulated to create a very specific gradient magnetic field. This produced gradient magnetic field is intentionally distorted such that subsequent eddy current induced field distortions will cancel out upon superposition, thus restoring the intended ideal gradient waveform. This concept is well illustrated by Figure 2.5 below.

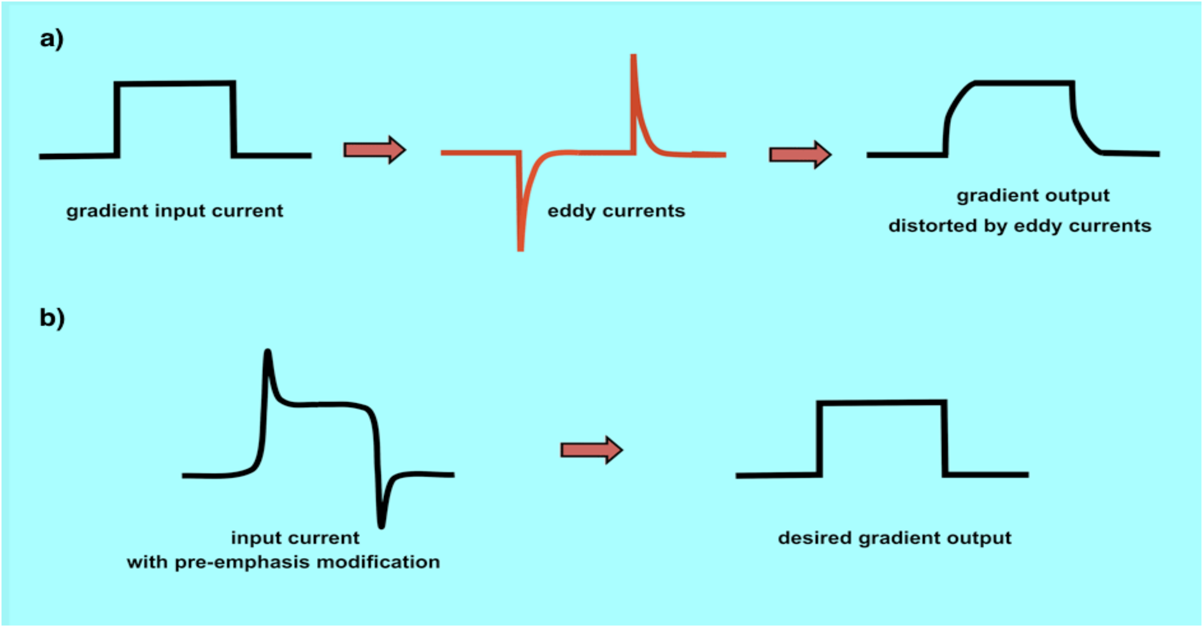

*Figure 2.5. Gradient waveform pre-emphasis overview. (a) Eddy current induced fields are generated during gradient slew. These fields cause distortions within the desired gradient waveform. An example of this phenomenon for trapezoidal gradient waveforms is shown in Figure 2.2. (b) Application of an intentionally distorted waveform can recover the desired gradient waveform upon superposition of eddy current induced fields. This compensation strategy is known as gradient waveform pre-emphasis. Figure source in references*[12]*.*

The intentional distortion field that is applied to the ideal gradient waveform is simply the opposite of the eddy current induced field[2], described by Eq 2.19 below:

$$B_{intentional} = -B_{eddy}(t) \quad \textbf{Eq 2.19}$$

$$= dG/dt * e_N(t)$$

$$= dG/dt * [\, H(t) \bullet \sum \alpha_N e^{-t/\tau} \,]$$

*Where: * = convolution operator*

- *$H(t)$ = unit step function*
- *$e_N(t)$ = eddy current impulse responses*
- *$\tau_N$ = time constant, ms*
- *$\alpha_N$ = amplitude coefficient*

It can be seen from Eq 2.19 that knowledge of the unique eddy current impulse responses is necessary to characterize the eddy current induced field and therefore necessary to calculate the pre-emphasis gradient waveform itself. Estimation of these eddy current impulse responses can be achieved via calibration techniques and will be discussed in the next section. Gradient pre-emphasis is routinely performed on scanners and has been shown to reduce eddy current errors by one to two orders of magnitude[2].

### *5C. Eddy Current Calibration*

Various calibration techniques exist to characterize the spatially dependent eddy current impulse responses, $e_N(t)$. Knowledge of these corresponding time constants and amplitudes is necessary to accurately model the eddy current induced field, and thus serves as a basis for different correction techniques (such as gradient waveform pre-emphasis). According to LTI theory, knowledge of the spatially dependent eddy current impulse responses will allow the estimation of the overall $B_{eddy}$ field induced by any arbitrary applied gradient waveform input (Eq 2.10).

The free induction decay (FID) responses of various point samples within the imaging volume can be used to estimate the spatially dependent eddy current impulse responses ($e_N(t)$). These FIDs are generated shortly after pulsing a test gradient to ensure that the effects of the eddy current phenomena are captured within the FID phase. Consider the phase of a FID signal for a single point location after a test gradient pulse is played:

$$\phi_1(t) = \left( \Upsilon \int B_{eddy}(r,t)\ dt \right) + \phi_0 \qquad \textbf{Eq 2.20}$$

*Where:* $r$ = *point sample location* $<x_s,y_s,z_s>$, *m*
- $B_{eddy}$ = *eddy current induced field, T*
- $\phi_0$ = *all phase contributions unrelated to eddy currents, radians*

A second FID is generated (at the same point location) after playing an opposite polarity test gradient pulse. The phase of this second FID is described by Eq 2.21:

$$\phi_2(t) = \left( - \Upsilon \int B_{eddy}(r,t)\ dt \right) + \phi_0 \qquad \textbf{Eq 2.21}$$

Subtraction of the phase profiles generated by the two separate FIDs will yield Eq 2.22 as follows:

$$\begin{aligned} \Delta\phi(t) &= \phi_1 - \phi_2 \\ &= \left[ \left( \Upsilon \int B_{eddy}(r,t)\ dt \right) + \phi_0 \right] - \left[ \left( - \Upsilon \int B_{eddy}(r,t)\ dt \right) + \phi_0 \right] \\ &= 2\Upsilon \int B_{eddy}(r,t)\ dt \qquad \textbf{Eq 2.22} \end{aligned}$$

Therefore, the eddy current induced field ($B_{eddy}$) local to this point location can be estimated from the time derivative of the phase difference profile generated by the two separate FIDs described above. With $B_{eddy}$ estimated, the eddy current impulse responses (time constants and amplitudes) specific to this point location can now be measured via fitting techniques and implemented in future pre-emphasis schemes[5]. This process is repeated for various point locations within the imaging volume to determine the overall $B_{eddy}$ spatial and temporal dependence. An inherent limitation with this calibration technique is that eddy currents with very short decay constants ($\tau_N$ < few milliseconds) are too short lived to be incorporated into the phase of the generated FID signals and therefore cannot be accounted for[5]. Nonetheless, calibration techniques measuring spatially dependent eddy current impulse responses for subsequent pre-emphasis are routinely implemented on commercial scanners.

### *5D. Static Tissue Phase Fitting*

Eddy current phase errors will persist in phase difference maps generated by PC-MRI. Maxwell phase errors are considered negligible in output phase difference maps when incorporating their analytical correction. Recall that regions of known static tissue within phase difference maps should exhibit zero phase due to MR physics; however due to eddy current influence, these static regions will now exhibit non-zero phase estimates. Therefore, fitting low-order polynomials to regions of known static tissue can serve as a quantitative model describing eddy current phase offsets from zero baseline. So called, static tissue fitting techniques utilize areas of known static tissue within phase difference maps to develop models describing the spatial dependence of eddy current errors to serve as a basis for correction[6,8,9]. These low-order polynomial models are then extrapolated to vessels of interest to correct for eddy current offsets within these vessels themselves, thereby yielding more accurate bloodflow velocities within said vessels upon subtraction.

The polynomial models used to describe eddy current phase offsets within static tissue regions contain low-order terms. It has been shown by various groups that eddy currents exhibit slow, smooth spatial dependence within the imaging plane itself[1,2]. These groups have modeled this behavior using constant, linear, and quadratic polynomial terms. These low-order terms describe the phase offsets created by both the induced "$B_0$ eddy current fields" and the "linear eddy current fields" observed in practice. Least-squares approaches are used when generating corresponding polynomial fits to describe eddy current error[8]. In addition, the polynomial models fitted to regions of known static tissue contain two spatial dimensions within them (x and y dimensions). In other words, the two-dimensional spatial dependence of eddy current phase error within the slice of interest alone is being modeled for. This is standard for single-slice acquisitions, multi-slice acquisitions, and volumetric acquisitions.

Current two-dimensional static tissue fitting techniques fall into one of two categories: local fitting approaches and global fitting approaches. The local and global fitting approaches are compared by MacDonald et al., and this study's findings are summarized below:

### *I. Local Static Tissue Fitting*

Within the local fitting scheme, phase estimates from static tissue pixels closely surrounding a vessel of interest are incorporated into the corresponding low-order polynomial fit. Typically, a 2-4 pixel annulus of static tissue surrounding vasculature is used for local corrections[8,10]. Identification of local stationary tissue pixels can be achieved via angiogram or velocity map thresholding techniques and is well documented[11]. A limitation to the local fitting scheme is that the phase error within static pixels surrounding a vessel of interest is assumed to be solely due to eddy current offsets themselves[8]. In actuality, the phase bias from zero baseline that is observed within these local static pixels may be due to a variety of sources (eddy currents, inherent velocity noise, partial volume effects, etc). If other sources of error, such as inherent velocity noise, dominate the level of eddy current error within these local static pixels, the generated polynomial fit will not be modeling eddy current nature itself[9]. In such cases, static tissue corrections have been shown to have the potential to introduce inaccuracies into the applied correction within vessels of interest[8,9,10]. As previously mentioned, velocity noise level is inversely related to the SNR of a PC-MRI acquisition[6].

### *II. Global Static Tissue Fitting*

Within the global fitting scheme, phase estimates from all static tissue pixels within the field of view (FOV) are incorporated into the corresponding low-order polynomial fit. Similar thresholding techniques can be used to define static tissue pixels for both fitting schemes. Global fitting techniques are hypothesized to be less sensitive to other sources of phase error (like velocity noise) as a significantly larger sample of pixels are used to generate polynomial models describing eddy currents. Therefore, majority of the pixels used to develop the global polynomial fit will contain phase offsets dominated by eddy current error itself rather than other sources of phase error (assuming eddy current error is significant in the first place).

However, the global fitting technique is still limited in that it has the potential to incorporate regions with low signal magnitude into the corresponding polynomial fit, and thus compromise correction performance[8,9]. Recall, phase cannot be accurately estimated within regions of low signal magnitude and due to this lack of fidelity in estimates, these regions should be avoided when developing the corresponding polynomial fit. Regions of low signal are typically observed at interfaces with mismatched magnetic susceptibilities, such as air-tissue interfaces (lungs, sinuses, neck, etc.)[8,10].

### *III. Local vs. Global Fitting Comparison*

The study completed by MacDonald et al. statistically analyzed the effectiveness of local and global static tissue fitting techniques. In this study, both fitting techniques were first used to correct eddy current phase offsets within a static phantom. Twenty-four uniquely oriented cut planes were prescribed at various locations within the static phantom and exhibited an average pixel flow rate of < 2.1 mL/sec per pixel prior to correction. Note that pixel flow rate within a static phantom should be zero according to MR physics; eddy currents account for this observed discrepancy. Upon polynomial fitting corrections, pixel flow rate estimates were shown to be statistically significantly closer to zero: local polynomial corrections yielded pixel flow rates of < 0.3 mL/sec per pixel and global polynomial corrections yielded pixel flow rates of < 0.5 mL/sec per pixel. Therefore, both local and global fitting techniques proved useful in reducing eddy current error within known static tissue regions. Within this static phantom experiment, the pixel flow rates estimated by local correction techniques were not found to be significantly different from the pixel flow rates estimated by global correction techniques. The study by MacDonald et al. then applied local and global fitting corrections within in-vivo datasets acquired from thirty healthy volunteers. Corrections in background regions of static tissue surrounding the cerebral vasculature once again showed reduction in pixel flow rates towards zero baseline as expected. Corrections in background static tissue were found to be independent of method implemented (local vs. global) following ANOVA testing. Finally, absolute volumetric flow rates were calculated in various vessels within the cerebral vasculature itself. Flow rates within vessels were calculated prior to correction and following both local and global polynomial corrections. Percent changes in flow rates after correction were small, indicating eddy current error was not severe within vessels of interest to begin with ( -6.04 % for local correction, -0.51 % for global correction). MacDonald et al. hypothesizes this is due to the fact that vessels of interest were relatively close to isocenter. Percent reductions in flow rates measured within background static tissue were about 60% for local corrections and 50% for global corrections for reference. However, vessel flow rates themselves were seen to vary significantly with specific correction method implemented; indicating performance difference between the two fitting strategies for vessel flow corrections. The results of the study conducted by MacDonald et al. directly highlight the usefulness of static tissue fitting techniques in reducing overall eddy current error, but still cannot conclude whether local or global correction is comparatively better than the other. In addition, the performance differences between the two fitting techniques have yet to be thoroughly characterized. The purpose of this work is to further investigate and characterize local and global static tissue fitting techniques in correcting eddy current phase error within PC-MRI.

### *IV. Overall limitations*

Various challenges can be associated with the implementation of static tissue correction techniques within PC-MRI. As previously mentioned, static tissue corrections may be compromised when other sources of phase error (like noise) dominate the static pixels used to develop polynomial models. Additionally in practice, the extent and location of static tissue available is highly variable. Static tissue used for corrections must avoid regions of air and adjacent vascular structures, and additionally must be as close as possible in proximity to the vessel of interest being corrected[10]. These requirements for the selection of static tissue are not met within the mediastinum or heart, thus limiting the correction technique for such applications[10]. For cerebral applications, there is a significant amount of static tissue that is eligible for correction surrounding vasculature[8].

## 6. References

1. Nayak, Krishna S., et al. "Cardiovascular magnetic resonance phase contrast imaging." *Journal of Cardiovascular Magnetic Resonance*, BioMed Central, 9 Aug. 2015, jcmr-online.biomedcentral.com/articles/10.1186/s12968-015-0172-7.

2. Bernstein, Matt A, et al. "Chapter 10: Correction Gradients." *Handbook of MRI Pulse Sequences*, 1st ed., Elsevier Academic Press, 2004, pp. 292–349.

3. Jehenson, P & Westphal, M & Schuff, Norbert. (1990). Analytical Method for the Compensation of Eddy-Current Effects Induced by Pulsed Magnetic Field Gradients in NMR Systems. Journal of Magnetic Resonance (1969). 90. 264-278. 10.1016/0022-2364(90)90133-T.

4. Gach, H M, et al. "A programmable pre-Emphasis system." *PubMed*, Magnetic resonance in medicine., Sept. 1998, www.ncbi.nlm.nih.gov/pubmed/9727946.

5. Spees, William M., et al. "Quantification and Compensation of Eddy-Current-Induced Magnetic Field Gradients." *PubMed*, Journal of magnetic resonance, Sept. 2011, www.ncbi.nlm.nih.gov/pmc/articles/PMC3163721/.

6. Markl, Michael. *Velocity Encoding and Flow Imaging*. University Hospital Freiburg, Dept. of Diagnostic Radiology, Medical Physics, Freiburg, Germany, Jan. 2005, ee-classes.usc.edu/ee591/library/Markl-FlowImaging.pdf.

7. Gatehouse, Peter D, et al. "Flow measurement by cardiovascular magnetic resonance: a multi-Centre multi-Vendor study of background phase offset errors that can compromise the accuracy of derived regurgitant or shunt flow measurements." *Journal of Cardiovascular Magnetic Resonance*, BioMed Central, 14 Jan. 2010, jcmr-online.biomedcentral.com/articles/10.1186/1532-429X-12-5.

8. MacDonald ME, Forkert ND, Pike GB, Frayne R (2016) Phase Error Correction in Time-Averaged 3D Phase Contrast Magnetic Resonance Imaging of the Cerebral Vasculature. PLOS one 11 (2): e0149930. doi:10.1371/journal.pone.0149930

9. Giese, Daniel & Haeberlin, Maximilian & Barmet, Christoph & P Pruessmann, Klaas & Schaeffter, Tobias & Kozerke, Sebastian. (2012). Analysis and correction of background velocity offsets in cine phase-contrast imaging using magnetic field monitoring. Magnetic resonance in medicine : official journal of the Society of Magnetic Resonance in Medicine / Society of Magnetic Resonance in Medicine. 67. 1294-302. 10.1002/mrm.23111.

10. Lotz, J, et al. "Cardiovascular flow measurement with phase-Contrast MR imaging: basic facts and implementation." *PubMed*, RSNA RadioGraphics, May 2002, www.ncbi.nlm.nih.gov/pubmed/12006694.

11. Walker, P G, et al. "Semiautomated method for noise reduction and background phase error correction in MR phase velocity data." *PubMed*, Journal of magnetic resonance imaging : JMRI., www.ncbi.nlm.nih.gov/pubmed/8324312.

12. Elster, Allen D. "Effect of eddy currents on gradient waveforms." *MRIquestions.com*, Division of Radiologic Sciences, Wake Forest School of Medicine, mriquestions.com/what-is-pre-emphasis.html.

# Chapter III: Specific Aims

## 1. Introduction

Despite advances in gradient hardware[1,2], eddy current induced phase errors remain a problem for absolute quantification in PC-MRI. Eddy current induced phase errors lead to velocity errors ($v_{eddy}$) observed to be as large as 10% to 25% of VENC in cardiac PC-MRI applications[3,4]. Various groups[3,5] have shown the efficacy of static tissue correction in reducing eddy current induced phase errors that influence PC-MRI derived parameters, including estimates of volumetric flow, 3D streamlines and particle traces, calculated pressure gradients, and wall shear stress (WSS). Studies comparing different implementations of these static tissue corrections (local vs. global schemes) have shown reduction of the velocity offset in background cerebral tissue on the order of 60% for local static tissue corrections and 50% for global corrections[3]. Despite these studies, the performance of local and global static tissue correction techniques have yet to be thoroughly characterized. The dependence of the two separate correction techniques on SNR and on the amount of static tissue used for correction is not well understood. Characterization of these relationships will highlight scenarios for the optimal usage of each separate fitting technique, and can thus improve the usefulness of static corrections as a whole in mitigating $v_{eddy}$ errors within PC-MRI.

## 2. Specific Aims

In order to characterize these relationships, static tissue corrections were analyzed within a static phantom experiment and within a flow phantom experiment. Corrections were repeated for a range of SNR and for varying amounts of static tissue used for polynomial fitting. We hypothesize that: 1) Correction performance of local fitting techniques lowers when compared to global fitting techniques for low SNR applications; and 2) Correction performance improves when using a larger amount of static tissue during polynomial fitting. Each of these claims were examined according to the following Specific Aims:

***Specific Aim 1*: *To examine the relationship between correction performance and SNR***. Local and global corrections were separately applied to reduce velocity offset within prescribed ROIs in a static phantom for varying SNR acquisitions. The ability of each correction technique to successfully reduce ROI velocity offset for varying SNR datasets was then assessed. ROI based correction differences between local and global techniques were also measured as a function of SNR within the static phantom experiment. Additionally, local and global techniques were separately applied to correct $v_{eddy}$ errors in total flow estimates within a flow phantom for varying SNR acquisitions. $V_{eddy}$ errors cause inconsistencies in total flow estimates measured at various locations within a closed circuit flow phantom; and these differences between total flow estimates are reduced with static tissue correction. The ability of each correction technique to successfully reduce these $v_{eddy}$ induced differences in total flow estimates was then assessed for varying SNR datasets. Correction differences between local and global strategies were also measured as a function of SNR within the flow phantom experiment. It is expected that local static tissue corrections are compromised by low SNR, and that correction differences between the two techniques will grow as SNR is decreased.

***Specific Aim 2*: *To examine the relationship between correction performance and the amount of static tissue used for correction***. Corrections implementing an increasing annular width of static tissue surrounding ROIs were applied to reduce velocity offset within a static phantom and to reduce $v_{eddy}$ induced differences in total flow estimates measured within a flow phantom. It is expected that static tissue correction will improve as larger amounts of surrounding tissue are used to develop polynomial models describing eddy current error.

## 3. Significance

The proposed study will highlight any dependencies that static tissue corrections have upon SNR and upon the amount of static tissue used during polynomial fitting. These relationships have not yet been clearly studied within the literature. Knowledge of these performance limitations associated with static tissue corrections will help define optimal scenarios for the implementation of local and global eddy current correction in PC-MRI, thus improving the usefulness of static corrections as a whole in reducing $v_{eddy}$ errors. Accurate absolute quantification in PC-MRI will directly improve the clinical usefulness of this imaging technique.

## 4. References

1. Bernstein, Matt A, et al. “Chapter 10: Correction Gradients.” *Handbook of MRI Pulse Sequences*, 1st ed., Elsevier Academic Press, 2004, pp. 292–349.

2. Giese, Daniel & Haeberlin, Maximilian & Barmet, Christoph & P Pruessmann, Klaas & Schaeffter, Tobias & Kozerke, Sebastian. (2012). Analysis and correction of background velocity offsets in cine phase-contrast imaging using magnetic field monitoring. Magnetic resonance in medicine : official journal of the Society of Magnetic Resonance in Medicine / Society of Magnetic Resonance in Medicine. 67. 1294-302. 10.1002/mrm.23111.

3. MacDonald ME, Forkert ND, Pike GB, Frayne R (2016) Phase Error Correction in Time-Averaged 3D Phase Contrast Magnetic Resonance Imaging of the Cerebral Vasculature. PLOS one 11 (2): e0149930. doi:10.1371/journal.pone.0149930

4. Gatehouse, Peter D, et al. "Flow measurement by cardiovascular magnetic resonance: a multi-Centre multi-Vendor study of background phase offset errors that can compromise the accuracy of derived regurgitant or shunt flow measurements." *Journal of Cardiovascular Magnetic Resonance*, BioMed Central, 14 Jan. 2010, jcmr-online.biomedcentral.com/articles/10.1186/1532-429X-12-5.

5. Nayak, Krishna S., et al. "Cardiovascular magnetic resonance phase contrast imaging." *Journal of Cardiovascular Magnetic Resonance*, BioMed Central, 9 Aug. 2015, jcmr-online.biomedcentral.com/articles/10.1186/s12968-015-0172-7.

# Chapter IV: Static Phantom Experiment

## 1. Introduction

The dependence of static tissue correction performance on SNR and on the extent of static tissue used during polynomial fitting is not well understood. Characterizing these dependencies within local and global static tissue correction strategies will define guidelines for their appropriate application towards correcting eddy current errors within PC-MRI data. We hypothesize that local static tissue correction performance lowers (in comparison to global corrections) for low SNR applications and that correction performance improves when using larger amounts of static tissue during polynomial fitting. To test these hypotheses, local and global corrections were applied to reduce velocity offset within established ROIs within a static tissue phantom. Corrections were repeated for a range of SNR and for increasing amounts of static tissue used during polynomial fitting. The ability of applied corrections to reduce velocity offset within static tissue ROIs was then assessed.

## 2. Methods

An adult torso sized phantom was filled with a polyacrylic acid gel slurry to minimize motion during the imaging experiment. Axial slices of this static phantom were acquired at 3T (Siemens, Prisma) using a three-directional velocity encoding protocol with the following acquisition parameters: VENC=80 cm/s, 6° flip angle, TE=3.37 ms, TR=5.16 ms, 1355 Hz/pixel bandwidth, 133x450 mm FOV, 1.78x1.78 $mm^2$/pixel resolution. This is a deliberately low SNR acquisition, and the number of averages was increased incrementally from 1 to 64 for subsequent acquisitions to obtain higher SNR datasets. A total of 6 datasets with unique SNR levels were acquired (1, 4, 8, 16, 32, and 64 averages).

In order to assess the relationship between correction performance and SNR (Specific Aim #1), static tissue corrections were applied to reduce velocity offset within ROIs of varying shape and size established within static tissue; and this process was repeated for datasets covering a range of averages (i.e. SNR). Prescribed ROIs were limited to $P_x$ and $P_y$ phase images, as eddy current offset within the $P_z$ phase images was negligible because the static phantom was most on-isocenter along the z-dimension. $P_x$ and $P_y$ phase images were produced by encoding flow along the x and y-dimensions respectively. The same 40 ROIs (20 from $P_x$ and 20 from $P_y$) were prescribed across each different SNR dataset, to obtain a total of 240 ROIs. 11 of these 240 ROIs were discarded as they displayed non-significant phase offset prior to correction, resulting in a total of 229 ROIs analyzed for Specific Aim #1. Phase offsets (prior to correction) within all ROIs were checked for significance (95% confidence) using a one-sample z-test ($H_0$: $\mu_{ROI} = 0$ cm/s, $H_A$: $\mu_{ROI} \neq 0$ cm/s). Local eddy current correction utilized phase estimates from a 4-pixel width annulus surrounding established ROIs to generate a polynomial fit describing eddy current phase error, similar to previous studies[1,2]. Global eddy current correction utilized phase estimates from all static pixels within the 2D FOV to develop a polynomial fit. Both correction strategies avoided both ROI pixels and noise pixels when developing a polynomial fit. Corrected phase estimates were obtained within ROIs upon subtraction of polynomial offset estimates on a pixel-by-pixel basis. Local and global polynomial fits were second order in x and y ($Ax^2 + By^2 + Cxy + Dx + Ey + F$), and were generated using least-squares methods. Local and global corrections were separately applied to all defined ROIs. The measured phase was converted to velocity by multiplication of a scaling factor ($VENC/\pi$) prior to data analysis. Successful eddy current correction of static ROIs results in a mean ROI velocity value that is closer to zero baseline following correction (reduction in velocity offset). Corrections that result in a ROI mean velocity that is farther away from zero baseline are considered unsuccessful, as they actually introduce phase error/velocity offset. Distributions of ROI offsets before and after applied static tissue corrections were plotted for distinct SNR datasets. Two sample z-tests (95% confidence) were repeated for distinct SNR datasets to compare local and global corrected distributions to zero baseline. The magnitude of the difference between local and global corrected mean velocities ("correction difference") was calculated and averaged for all ROIs pertaining to a single SNR dataset; and this process was repeated for all acquired datasets. SNR levels were calculated for each dataset by dividing the mean signal within the static phantom by the standard deviation of background noise.

In order to assess the relationship between correction performance and the extent of static tissue coverage (Specific Aim #2), ROIs of varying shape and size were once again established within static tissue in axial slices. The same 40 ROIs (20 from $P_x$ and 20 from $P_y$) were prescribed across varying SNR datasets to evaluate Specific Aim #2. Prescribed ROIs were again limited to $P_y$ and $P_x$ phase images and checked for significant offset (prior to correction). The same 229 total ROIs were analyzed in Specific Aim #2. ROI based corrections were applied and repeated using a surrounding static tissue annulus of varying size for polynomial fitting, incremented from 4 pixels to 128 pixels in width. A 128-pixel width annulus covered a majority of static pixels within acquired axial slices. The magnitude of residual velocity (speed) offset following applied correction (within a single ROI) was then measured as a function of static pixel annulus width. The residual speed offset vs. annulus width profiles for all prescribed ROIs within a single SNR dataset were then averaged. This process was repeated for all acquired SNR datasets.

## 3. Results

Axial slices of a static phantom were acquired. Figure 4.1 displays static phantom magnitude images from varying SNR acquisitions.

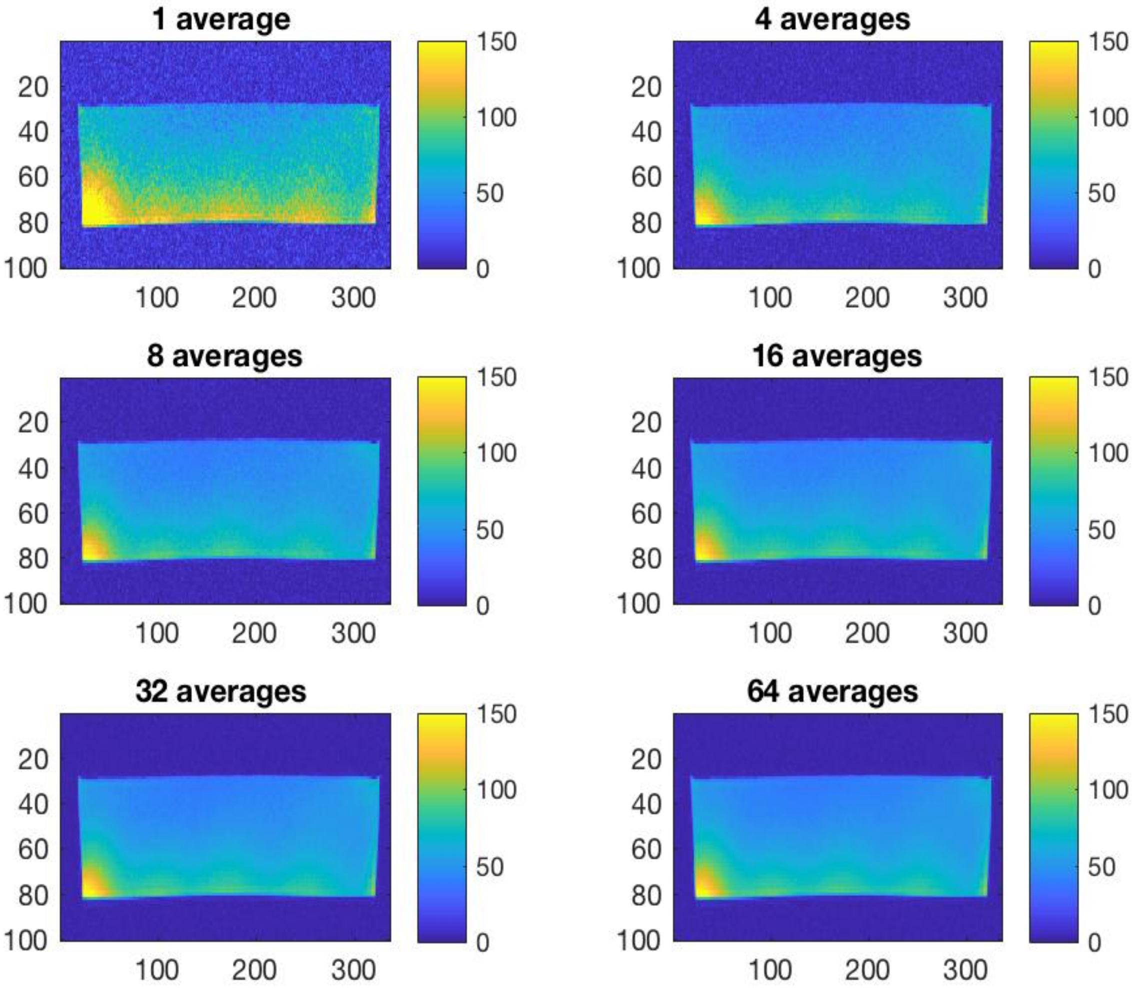

*Figure 4.1. Static phantom magnitude images for varying SNR acquisitions. Static tissue within the phantom is shown in light blue and background noise is surrounding in dark blue. SNR was calculated as average signal within the phantom divided by the standard deviation of background noise.*

ROIs for correction were prescribed within static tissue of $P_y$ and $P_x$ phase images. Phase was converted to velocity prior to analysis by multiplication of a VENC/ π scaling factor. Figures 4.2 and 4.3 display static phantom velocity images from varying SNR acquisitions.

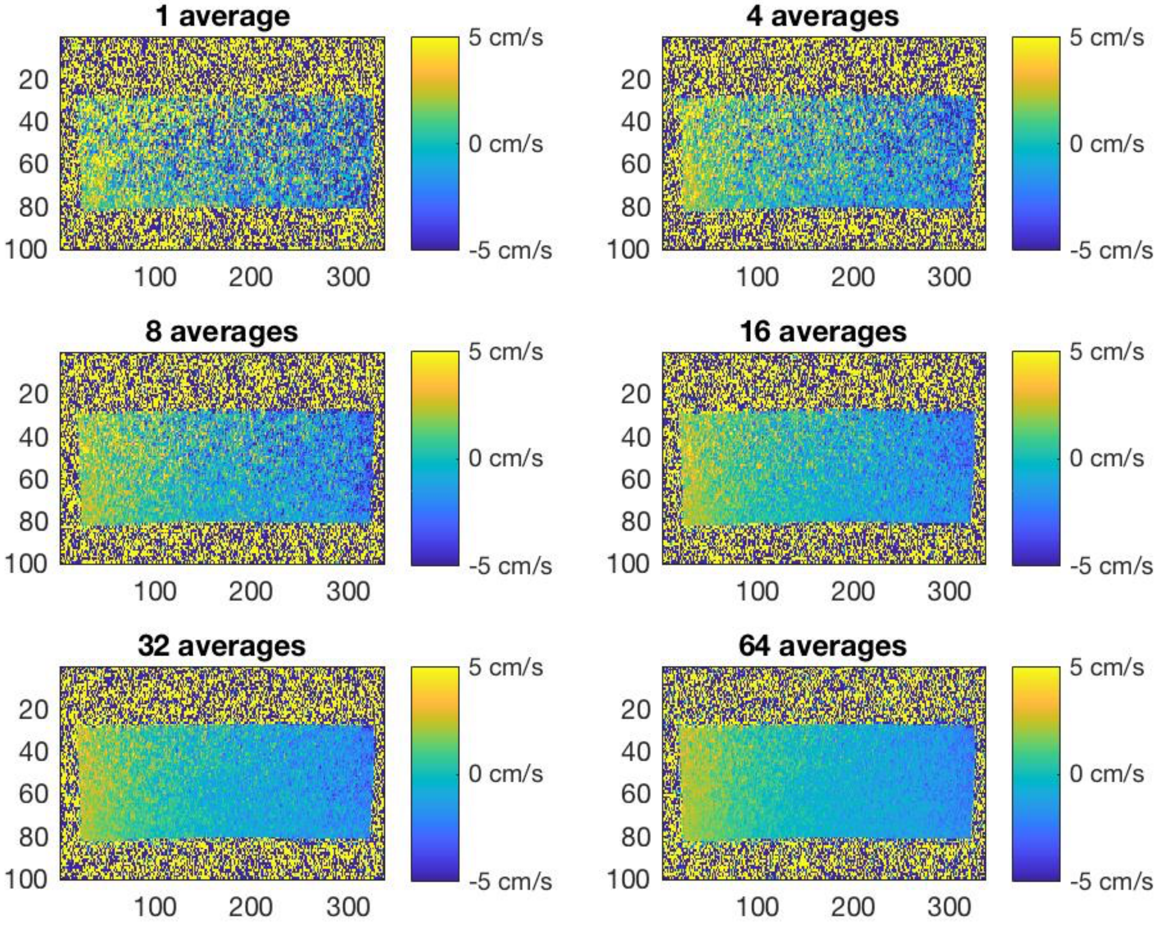

*Figure 4.2. Static phantom $V_y$ velocity images for varying SNR acquisitions. Flow encoding gradients were played on the $G_y$ axis to develop $V_y$ velocity maps. Eddy current offsets from zero cm/s baseline were observed within static "tissue".*

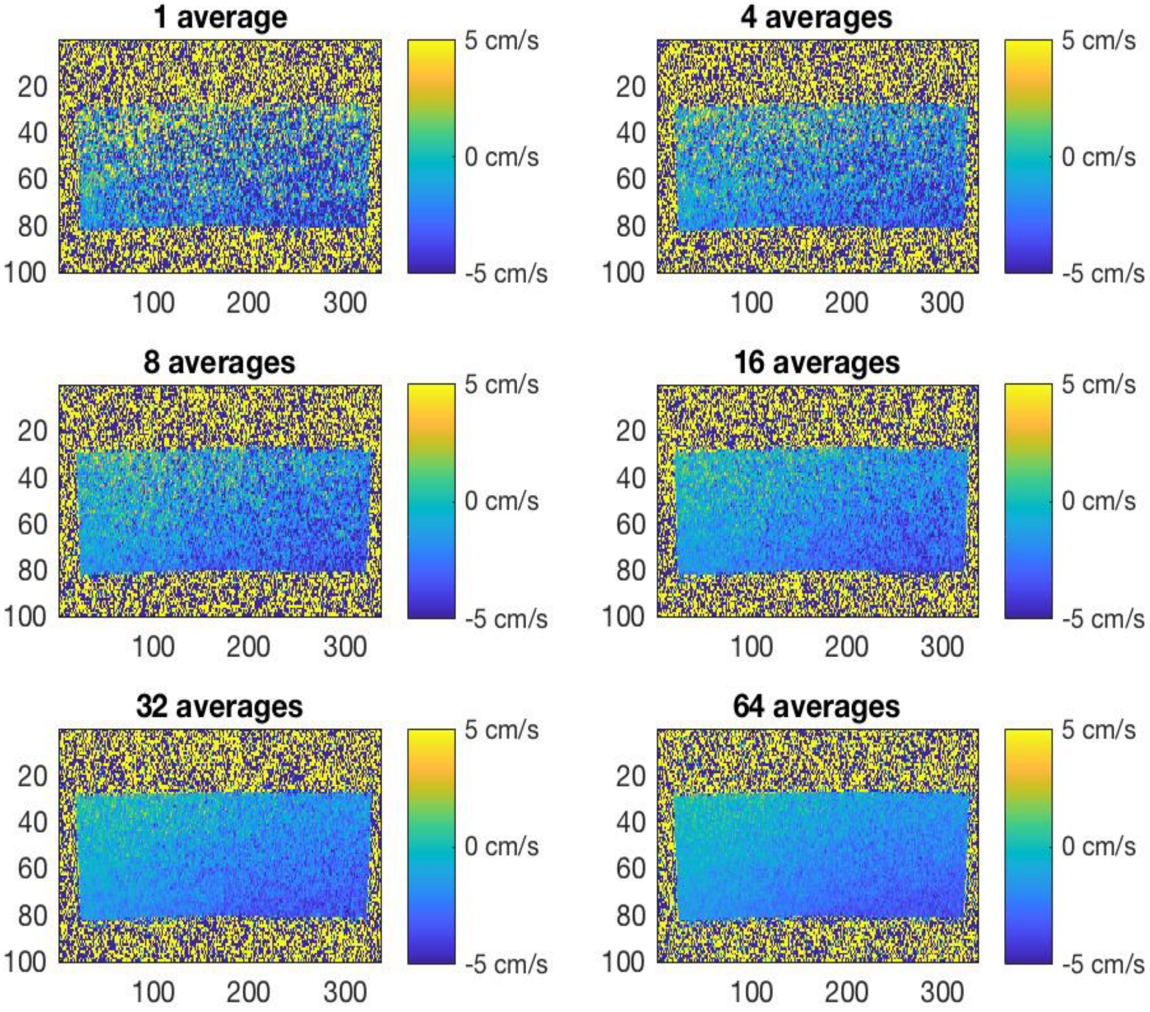
1 average

4 averages

8 averages

16 averages

32 averages

64 averages

*Figure 4.3. Static phantom $V_x$ velocity images for varying SNR acquisitions. Flow encoding gradients were played on the $G_x$ axis to develop $V_x$ velocity maps. Eddy current offsets from zero cm/s baseline were observed within static "tissue".*

Eddy current offsets as large as ~7 cm/s (~9 % of VENC) were observed within static tissue. Figure 4.4 displays four sample ROIs and highlights the corresponding static tissue regions used for polynomial fitting. A four-pixel width annulus of static tissue surrounding ROIs was used for local corrections to evaluate Specific Aim #1 (teal pixels). Global corrections used all static tissue pixels within axial slices to develop a polynomial fit describing eddy current offset (teal and blue pixels). ROI pixels (yellow) and noise pixels (red) were both excluded during polynomial fitting for both correction strategies.

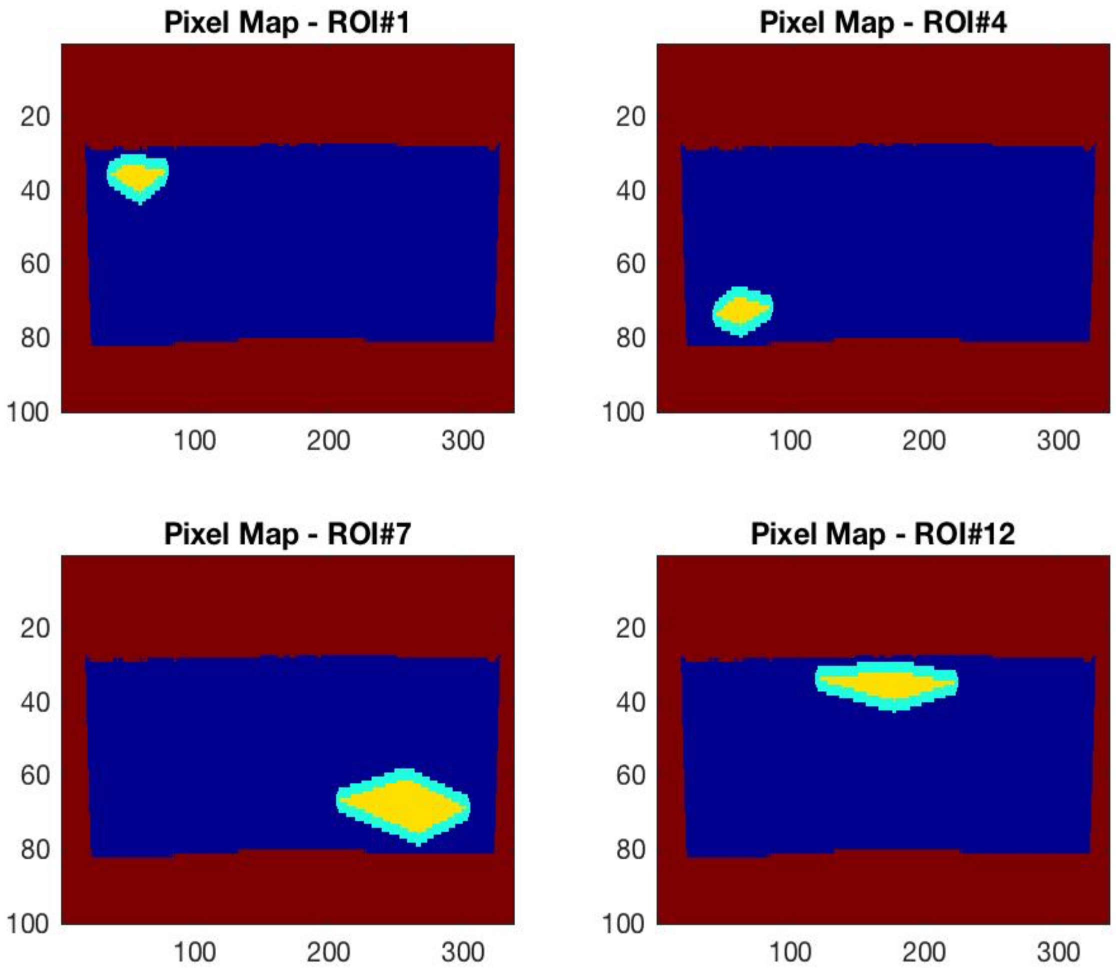

*Figure 4.4. Static phantom ROI pixel maps. Pixel maps distinguish pixels used for local and global polynomial fitting by color. ROI pixels (yellow) are surrounded by a 4-pixel width annulus of static tissue (teal). Other static tissue pixels within the 2D FOV (blue) and noise pixels (red) are also shown. Unique pixel maps were constructed for every analyzed ROI.*

Figure 4.5 displays a single prescribed ROI (ROI #7) with an increasing width static tissue annulus used for polynomial fitting. This process is repeated for prescribed ROIs across varying SNR datasets to evaluate Specific Aim #2.

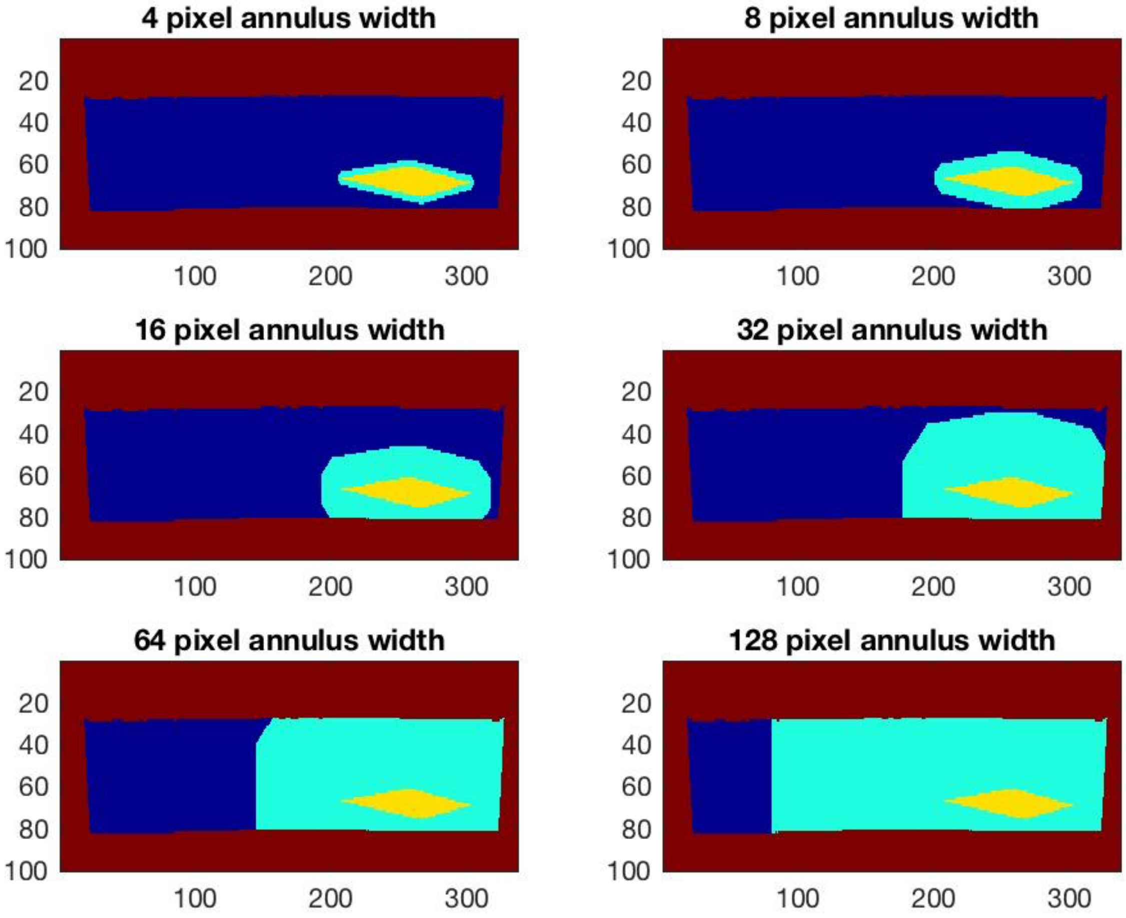

*Figure 4.5. Increasing static tissue coverage in ROI pixel maps. Pixel maps distinguish pixels used for polynomial fitting by color. ROI corrections implementing an increasing width surrounding static tissue annulus (teal) for polynomial fitting is shown. This process was repeated for all prescribed ROIs across distinct SNR datasets. Unique pixel maps were constructed for every analyzed ROI.*

Figure 4.6 displays the same single ROI (ROI #7) following both local and global corrections within a single SNR dataset (64 average dataset). Velocity offset within this ROI was significantly reduced towards zero baseline following both local and global static tissue corrections ($\mu_{uncorrected}$ = -3.0 cm/s, $\mu_{local}$ = 0.0 cm/s, $\mu_{global}$ = 0.0 cm/s). A difference image confirms pixel-level differences between applied ROI corrections by local and global fitting strategies (non-zero estimates within ROI itself in produced difference image).

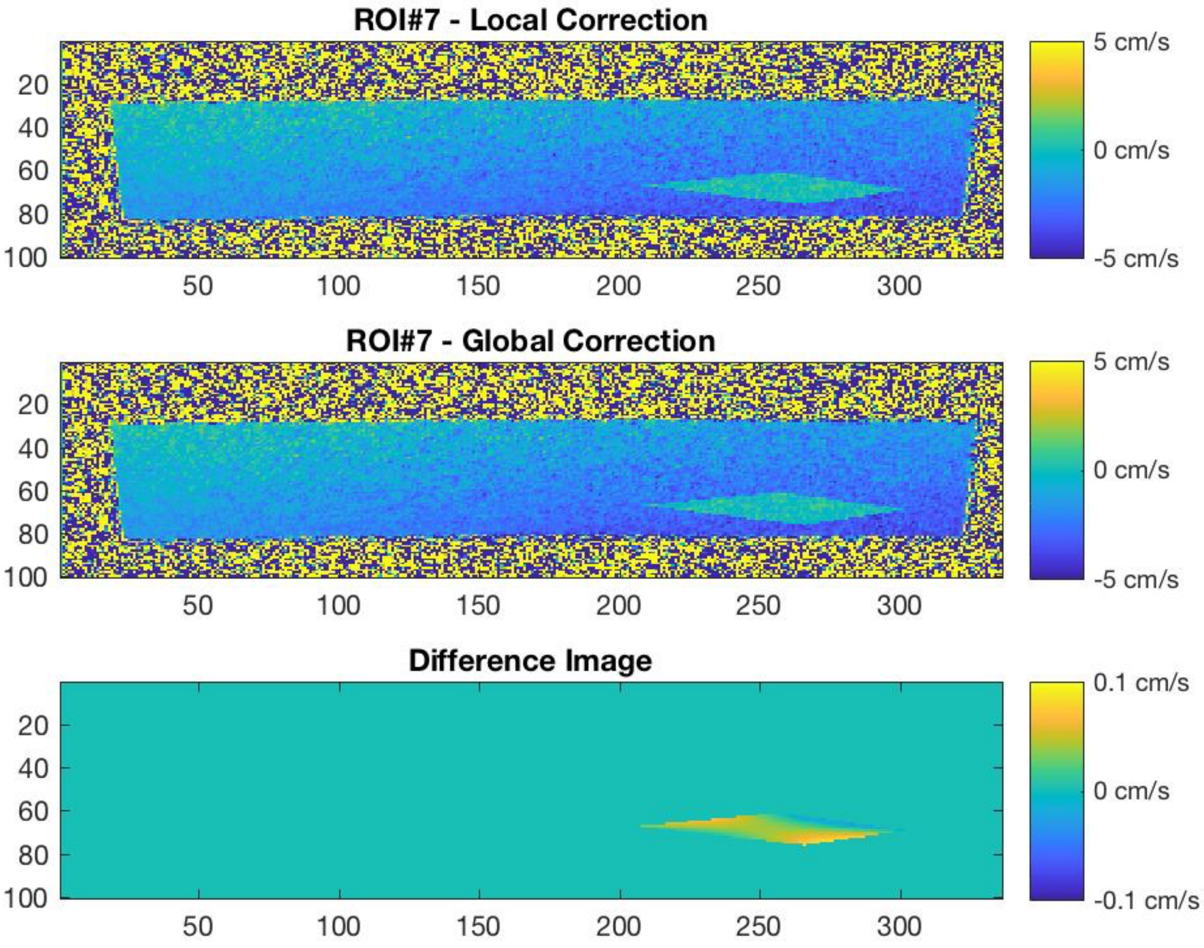

*Figure 4.6. Corrected $V_x$ velocity images. Velocity offset within ROI#7 was significantly reduced upon correction ($\mu_{uncorrected}$ = -3.0 cm/s, $\mu_{local}$ = 0.0 cm/s, $\mu_{global}$ = 0.0 cm/s). A difference image confirms pixel-level differences in applied ROI corrections between local and global strategies.*

229 of 229 (100%) established ROIs (for Specific Aim #1) displayed mean velocity values that were closer to zero baseline following global corrections. 219 of 229 (~96%) established ROIs displayed mean velocity values that were closer to zero baseline following local corrections. 10 of 229 (~4%) established ROIs displayed mean velocity values that were further from zero baseline following local correction, indicating additional phase error was introduced. These errors were all introduced during local correction in datasets with SNR < 30.

Of the 80 ROIs established in datasets with SNR > 30, global fitting provided a closer correction to zero baseline in 56 of 80 ROIs (70%) and local fitting provided a closer correction to zero baseline in 24 of 80 ROIs (30%). No instances of phase error being introduced by static tissue correction were observed for datasets with SNR > 30. Of the 149 ROIs established in datasets with a SNR < 30, global fitting provided a closer correction to zero baseline in 108 of 149 ROIs (~72%) and local fitting provided a closer correction to zero baseline in 41 of 149 ROIs (~28%). All 10 instances of local correction introducing phase error occurred for datasets with SNR < 30. 8 of these 10 total instances occurred for datasets with SNR < 20. Global corrections showed no instances of introducing phase error across all SNR datasets.

Figure 4.7 depicts the distribution of ROI mean speeds before and after static tissue corrections for distinct SNR datasets.

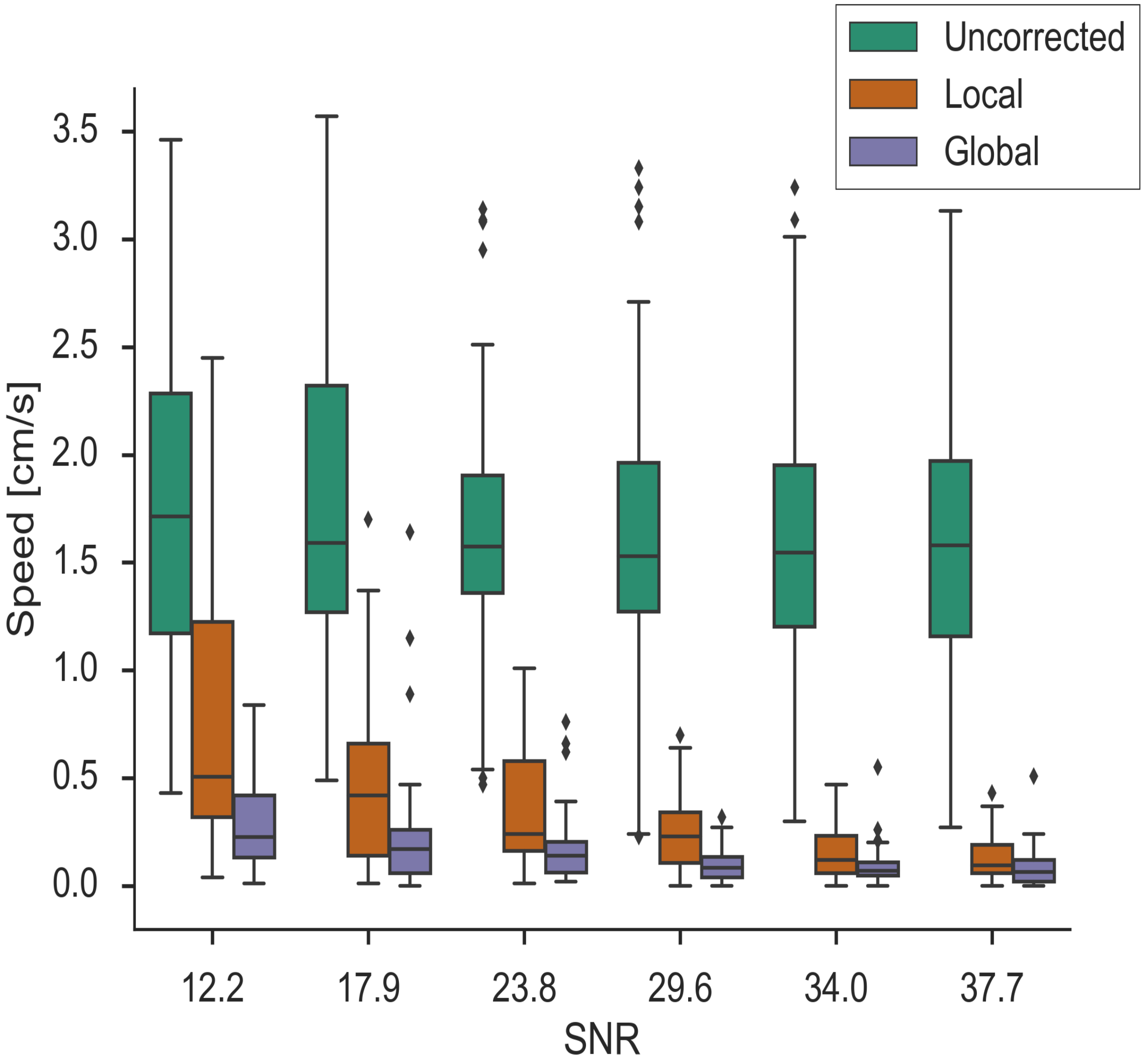

*Figure 4.7. Distribution of ROI mean speeds for distinct SNR. Uncorrected distributions (green) and distributions following both local (orange) and global (purple) corrections are shown. Two-sample z-tests confirmed local and global corrected distributions to be statistically significantly different (95% confidence) for acquisitions of SNR ~ 12, 18, and 24 (p = 0.0039, p = 0.0024, and p = 0.0239 respectively). These correspond to acquisitions of 1, 4, and 8 averages respectively. Global corrections therefore outperformed local corrections in reducing velocity offset when SNR < 30.*

The resulting correction difference vs. SNR plot (Fig 4.8) shows that there is greater disagreement between correction methods as SNR decreases. Correction differences between the two strategies were observed to be as large as 0.9 cm/s for low SNR protocols and as small as 0.2 cm/s for high SNR protocols.

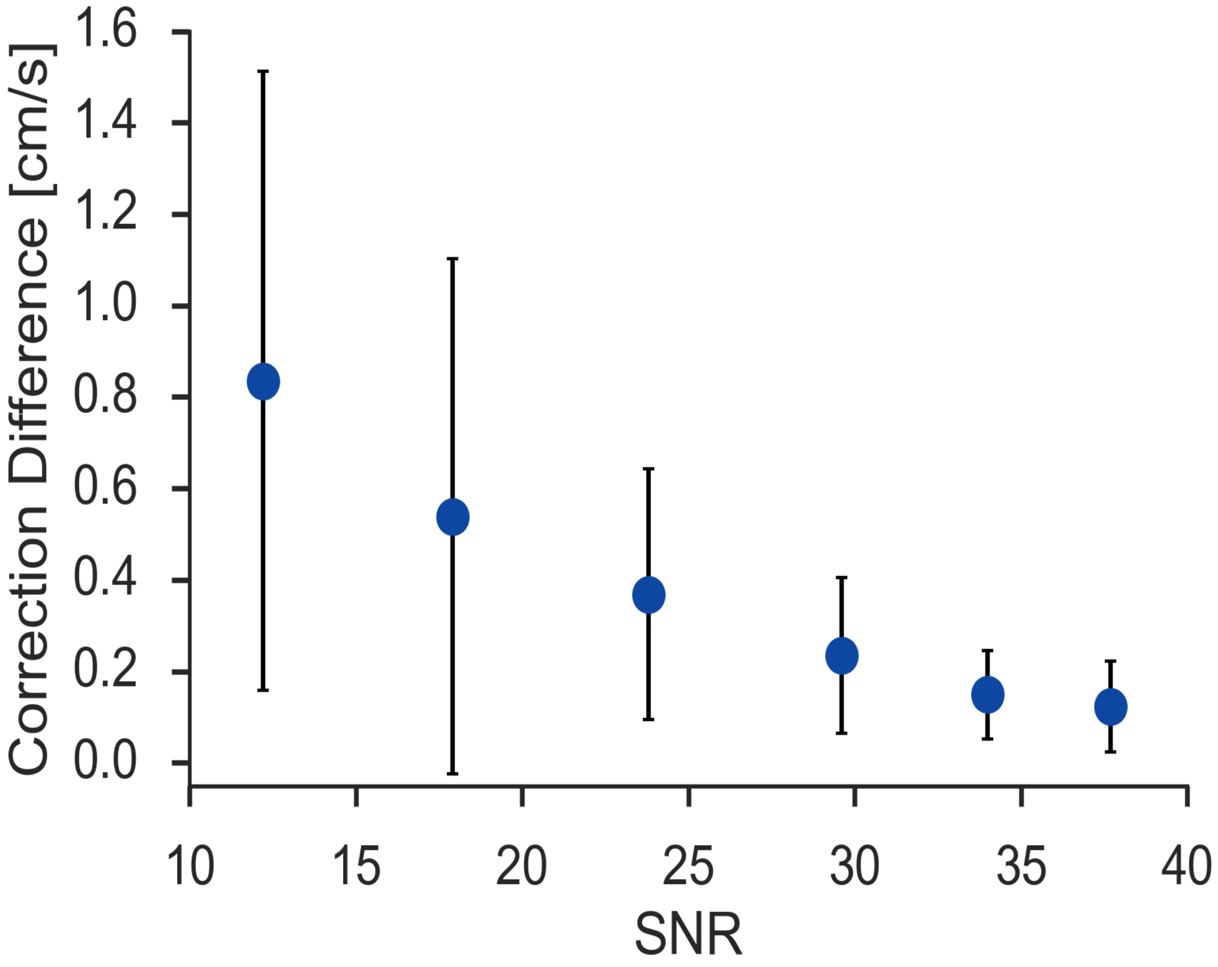

*Figure 4.8. Correction difference as a function of SNR. Differences between applied local and global corrections grew in magnitude as SNR was decreased within the static phantom experiment.*

Residual speed offset from zero baseline was measured within prescribed ROIs following applied corrections implementing increasing amounts of static tissue (Figure 4.9).

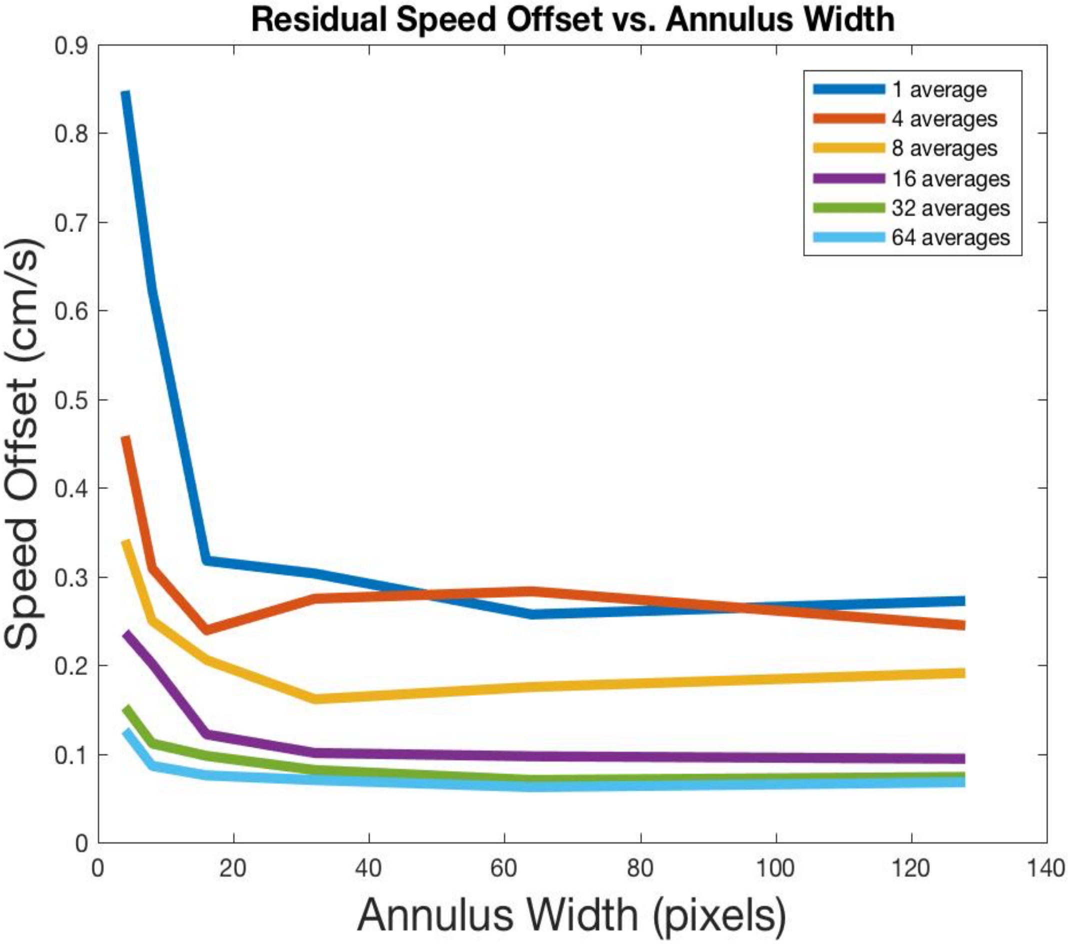

*Figure 4.9. Residual speed offset as a function of static tissue annulus width. Perfect static tissue correction results in zero speed offset within prescribed ROIs following applied corrections. Static corrections improved (resulted in smaller residual offset) by increasing the amount of static tissue used during polynomial fitting. Residual speed offset was reduced by up to an additional ~0.6 cm/s for low SNR applications upon increasing static tissue annulus width. Improvement in correction was smaller for high SNR applications (~0.05 cm/s).*

## 4. Discussion:

Offset on the order of 0.6 cm/s has previously been reported to affect estimates of cardiac output and shunt flow measurement by up to 5% and 10% respectively[3], and therefore the observed offset within this static phantom experiment can be considered significant. Overall, both local and global static tissue correction strategies proved useful in reducing velocity offset within static tissue. Global correction was observed to reduce velocity offset within 100% of all prescribed static ROIs. Local correction was observed to reduce velocity offset within ~96% of all prescribed static ROIs. However, local static tissue fitting techniques were also seen to occasionally introduce phase error when SNR of the implemented protocol fell below 30 (error introduced by local correction in ~7% of ROIs with SNR < 30). As SNR continued to decrease below 30, local fitting techniques began to introduce error with increased occurrence. In direct contrast, global fitting techniques showed no instances of introducing phase error across all SNR levels. Correction differences between local and global strategies were observed to be larger than the 0.6 cm/s error tolerance during low SNR applications (Figure 4.8), thus indicating that selection of either local or global polynomial fitting is meaningful for such scenarios. For datasets with SNR > 30, correction differences between the two fitting strategies are small in magnitude and are observed to be highly ROI dependent. Figure 4.7 confirms the compromised ability of local corrections in reducing offset within static ROIs (in comparison to global corrections) for low SNR applications. Figure 4.9 indicates that for low SNR applications, static tissue correction performance improves by increasing the amount of surrounding static tissue used during polynomial fitting. This study indicates that local fitting strategies may only be suitable above a certain SNR level, and warrants further investigation. In addition, this study indicates that it is advisable to maximize the amount of static tissue used during polynomial fitting for corrections in low SNR applications. Calculated SNR levels from a PC-MRI experiment depend upon many protocol parameters, including: $B_0$ field strength, flip angle, voxel size, number of averages, and more. PC-MRI acquisitions spanning a range of SNR of ~ 5 - 85 have been reported within literature[4,5].

## 5. References

1. MacDonald ME, Forkert ND, Pike GB, Frayne R (2016) Phase Error Correction in Time-Averaged 3D Phase Contrast Magnetic Resonance Imaging of the Cerebral Vasculature. PLOS one 11 (2): e0149930. doi:10.1371/journal.pone.0149930

2. Lotz, J, et al. "Cardiovascular flow measurement with phase-Contrast MR imaging: basic facts and implementation." *PubMed*, RSNA RadioGraphics, May 2002, www.ncbi.nlm.nih.gov/pubmed/12006694.

3. Gatehouse, Peter D, et al. "Flow measurement by cardiovascular magnetic resonance: a multi-Centre multi-Vendor study of background phase offset errors that can compromise the accuracy of derived regurgitant or shunt flow measurements." *Journal of Cardiovascular Magnetic Resonance*, BioMed Central, 14 Jan. 2010, jcmr-online.biomedcentral.com/articles/10.1186/1532-429X-12-5.

4. Donati, Fabrizio, et al. "Non-Invasive pressure difference estimation from PC-MRI using the work-Energy equation." *Medical Image Analysis*, Elsevier, 8 Sept. 2015, www.sciencedirect.com/science/article/pii/S1361841515001371.

5. Middione and Ennis: Reduced chemical shift- induced phase errors at 3T using novel PC-MRI encoding gradients. Journal of Cardiovascular Magnetic Resonance 2013 15(Suppl 1):W35.

# Chapter V: Flow Phantom Experiment

## 1. Introduction

The dependence of static tissue correction performance on SNR and on the extent of static tissue used during polynomial fitting is not well understood. Characterizing these dependencies within local and global static tissue correction strategies will define guidelines for their appropriate application towards correcting eddy current errors within PC-MRI data. We hypothesize that local static tissue correction performance lowers (in comparison to global corrections) for low SNR applications and that correction performance improves when using larger amounts of static tissue during polynomial fitting. To test these hypotheses, local and global corrections were applied to reduce $v_{eddy}$ induced differences in total volumetric flow estimates measured from various locations along a closed circuit flow phantom. Corrections were repeated for a range of SNR and for increasing amounts of static tissue used during polynomial fitting. The ability of applied corrections to reduce $v_{eddy}$ induced differences in total volumetric flow estimates was then assessed.

## 2. Methods:

An adult torso sized phantom was filled with a polyacryclic acid gel slurry to minimize motion during the imaging experiment. A “U-shaped” tubing network made of polypropylene tubing (3/8′′ outer diameter x 0.062′′ wall thickness) was submerged within this gel slurry; mimicking the physiological scenario of a blood vessel containing flow surrounded by background static tissue. The polypropylene tubing network was designed to incorporate multiple bifurcations; bifurcations were constructed using polypropylene Y-connectors (3/8′′ x 3/8′′ x 3/8′′). Ends of the tubing network were connected to male and female lines on an external flow pump (Shelley CardioFlow 5000 MR, located outside the MRI scanner) to form a closed flow circuit. The tubing network was submerged and positioned within the gel-filled phantom such that flow within tubing would be oriented along the z-dimension (long-axis) of the MRI scanner. Pulsatile flow was generated within the tubing network throughout the imaging experiment. Time-resolved velocity information was measured throughout the tubing network using a 4D-flow protocol at 3T (Siemens, Prisma) with the following acquisition parameters: VENC = 70 cm/s, 1° flip angle, TE = 2.92 ms, TR = 5.58 ms, 1.875x1.875x3 $mm^3$ voxel dimensions, 495 Hz/pixel bandwidth, and 20 temporal phases acquired. This is a deliberately low SNR acquisition, and flip angle was increased incrementally for subsequent acquisitions to span a range of SNR. Acquisitions with flip angles of 1°, 2°, 4°, 6°, 8°, and 10° were acquired. Phase was converted to velocity via multiplication of a scaling factor (VENC/ π) prior to data analysis.

Acquired axial slices provided cross-sectional views at unique locations along the tubing network. Acquired axial slices intersected the "U-shaped" tubing network multiple times, allowing for separate estimates of total volumetric flow ($Q_{total}$) to be calculated from a single axial slice position alone. According to conservation of total mass, any two estimates of $Q_{total}$ calculated within the "U-shaped" closed flow circuit should be equal in magnitude.

Total volumetric flow, $Q_{total}$, through a vessel was estimated as the sum of volumetric flow rates over all acquired temporal phases. Volumetric flow rate from a single temporal phase was calculated as the product of vessel lumen (cross-sectional) area and average perpendicular velocity through this vessel lumen. Encoding velocity along the z-dimension of the scanner provided the perpendicular velocity components necessary to estimate total volumetric flow, $Q_{total}$.

Local polynomial fits describing eddy current error utilized phase estimates from a 4-pixel width annulus of static tissue surrounding vessel lumens for correction. Global polynomial fits utilized phase estimates from all static pixels within the 2D FOV to describe eddy current offsets. Local and global corrections both avoided noise pixels and pixels within vessel lumens when developing a polynomial fit. Local and global polynomial fits were second order in x and y ($Ax^2 + By^2 + Cxy + Dx + Ey + F$), and were generated using least-squares methods. Corrected velocity estimates were obtained within vessel lumens upon subtraction of estimated eddy current offset on a pixel-by-pixel basis. Local and global polynomial fits provided estimates of eddy current offsets within vessel lumens. Corrected total volumetric flow estimates were obtained by using corrected velocity estimates (across all acquired temporal phases) within vessel lumens to calculate total flow. Unique polynomial corrections (both local and global) were applied to vessel lumens for each acquired temporal phase.

In order to evaluate the relationship between static tissue correction performance and SNR (Specific Aim #1), separate total volumetric flow ($Q_{total}$) estimates measured from a particular axial slice position were compared. $V_{eddy}$ errors introduce differences between estimated total volumetric flows from an axial slice position, and these differences ($\Delta Q_{total}$) are reduced in overall magnitude upon static tissue correction. Local and global corrections were separately applied to correct total volumetric flow estimates. Successful static tissue correction results in a magnitude reduction in flow difference ($\Delta Q_{total}$). Unsuccessful static tissue correction results in no change or an increase in flow difference ($\Delta Q_{total}$). Improved correction performance results in a larger reduction in flow difference ($\Delta Q_{total}$). The ability of local and global static tissue corrections to successfully reduce $\Delta Q_{total}$ was assessed for five unique axial slice positions along the tubing network. This analysis was then repeated for acquisitions spanning a range of SNR. A total of 30 cases of flow difference ($\Delta Q_{total}$) were analyzed (5 axial slice positions x 6 distinct SNR acquisitions). Uncorrected, local corrected, and global corrected flow difference ($\Delta Q_{total}$) distributions were compared for distinct SNR datasets. Two sample t-tests (95% confidence) were repeated for distinct SNR datasets to compare local and global corrected flow difference distributions. "Correction difference" within the flow phantom experiment is defined as the magnitude difference between estimated total volumetric flows by local and global corrections. Correction differences were calculated and averaged for all five axial slices of interest (within a single SNR dataset). This process was repeated for distinct SNR acquisitions, and correction difference was then plotted as a function of SNR.

In order to evaluate the relationship between correction performance and extent of static tissue coverage during polynomial fitting (Specific Aim #2), corrections incorporating increasing amounts of static tissue were applied to reduce flow differences ($\Delta Q_{total}$) measured from a particular axial slice position. Improved correction performance manifests as a larger reduction in flow difference ($\Delta Q_{total}$). Static tissue annular widths surrounding vessel lumens were increased incrementally from 4 to 128 pixels for corrections; a 128-pixel wide annulus covered majority of static tissue within the 2D FOV. Flow difference ($\Delta Q_{total}$) was measured as a function of surrounding static tissue annulus width (for a particular axial slice position). The $\Delta Q_{total}$ vs. annulus width profiles for all five axial slices of interest were then averaged; and this process is repeated for distinct SNR datasets.

## 3. Results:

Axial slices of a flow phantom acquired using a 4D-flow protocol were used for measurements. Magnitude images from four sample axial slice positions along a flow phantom are shown in Figure 5.1.

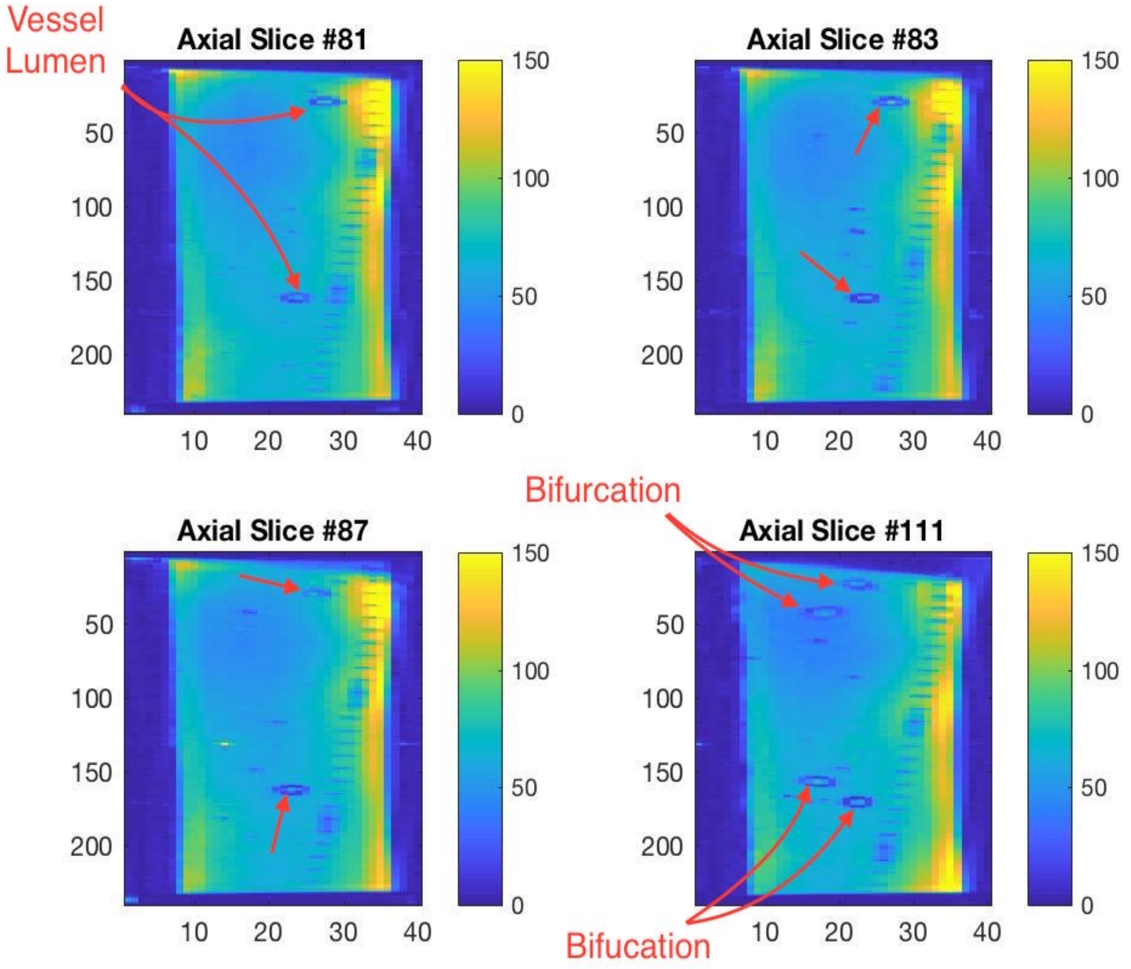

*Figure 5.1. Flow phantom axial magnitude images. Axial slices provided cross-sectional views at different locations along the flow phantom. Axial slices allow for calculations of total volumetric flow within the tubing network. Unique axial slice positions are shown for an identical temporal phase. Axial slices 81, 83, and 87 intersected a singular section within the "U shaped" tubing network. Axial slice 111 intersected a bifurcation segment within the "U shaped" tubing network.*

Velocity images from the same four sample axial slice positions are shown in Figure 5.2.

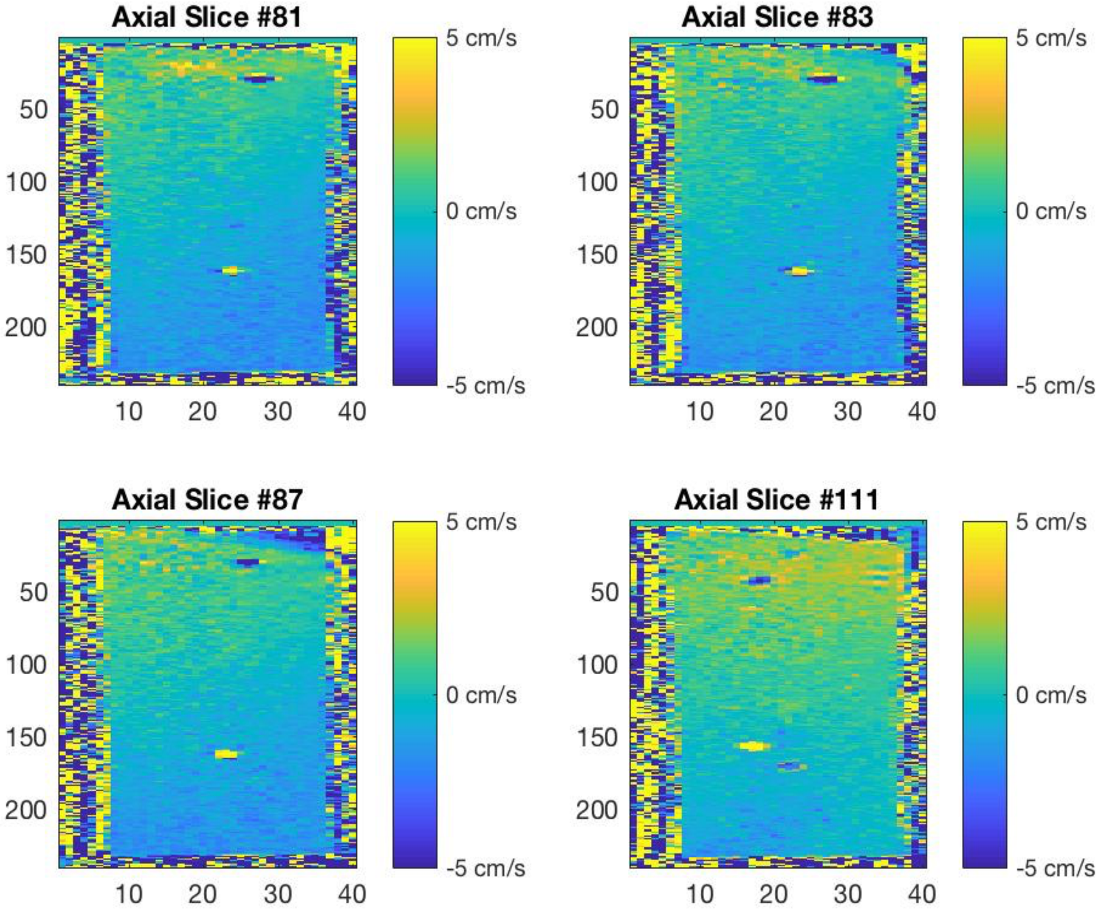

*Figure 5.2. Flow phantom axial velocity images. Unique axial slice positions are shown at an identical temporal phase. Axial slices intersected the "U shaped" tubing network at multiple locations, allowing separate estimates of total volumetric flow to be calculated from a single axial slice position alone. Ideally, calculated estimates of total volumetric flow from vessel lumens within an axial slice should be equal in magnitude and opposite in direction. In practice, eddy currents induce magnitude differences between calculated total flows (*$\Delta Q_{total}$*). Eddy current offsets in static "tissue" surrounding vessel lumens were observed within velocity images.*

4D-flow acquisitions spanned a range of SNR (Figure 5.3 and 5.4).

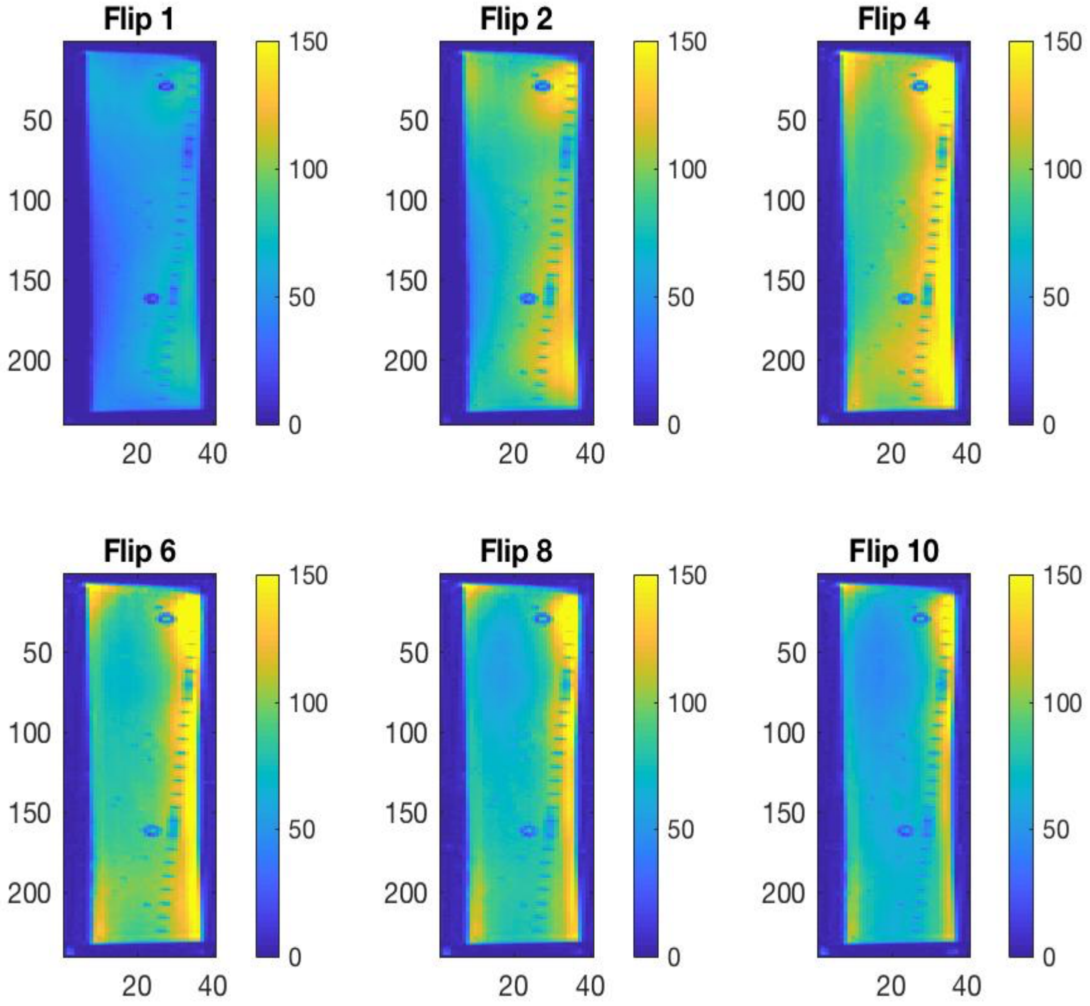

*Figure 5.3. Flow phantom axial magnitude images for varying SNR acquisitions. Datasets spanning a range of SNR were obtained by incrementing the flip angle parameter of the 4D-flow protocol. A single temporal phase and axial slice position are shown (temporal phase 4 of 20, axial slice 81 of 192).*

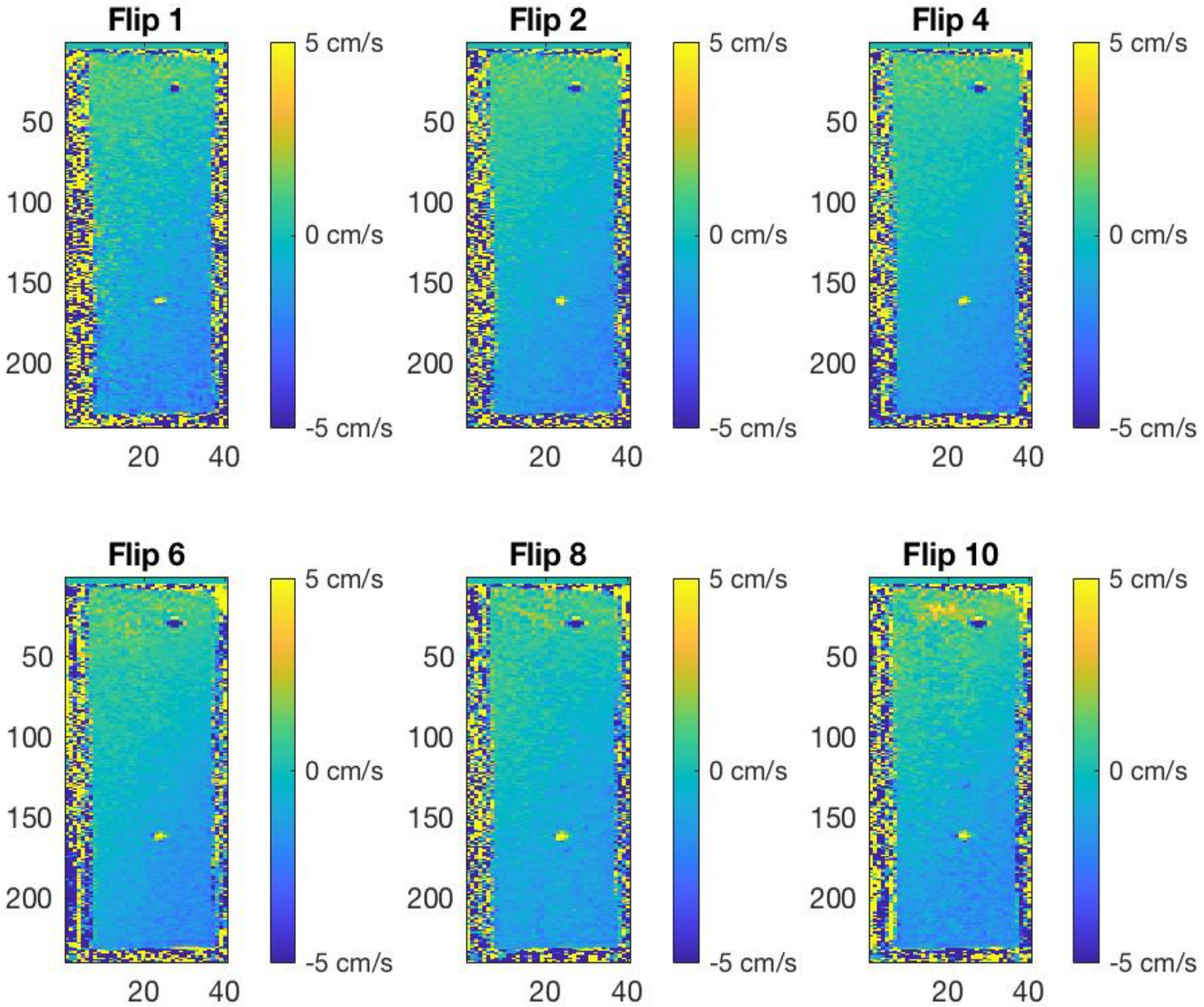

*Figure 5.4. Flow phantom axial velocity images for varying SNR acquisitions. $V_z$ velocity images (flow encoding along the z-dimension) yield through-plane velocity estimates within vessel lumens, allowing calculation of total volumetric flow. Eddy current offsets from zero cm/s baseline within static "tissue" surrounding vessel lumens were observed. A single temporal phase and axial slice position are shown (temporal phase 4 of 20, axial slice 81 of 192).*

Local polynomial fits used a 4-pixel wide ring of static tissue surrounding vessel lumens to describe eddy current offsets. Global polynomial fits used all static tissue pixels within the 2D FOV to describe eddy current offsets. Both fitting techniques avoided noise pixels and pixels within vessel lumens themselves. Wall thicknesses of the tubing network surrounding vessel lumens were considered noise pixels and were omitted from polynomial fitting and total volumetric flow calculations. Sample pixel maps, used to classify pixels prior to polynomial fitting, are shown in Figure 5.5 and 5.6.

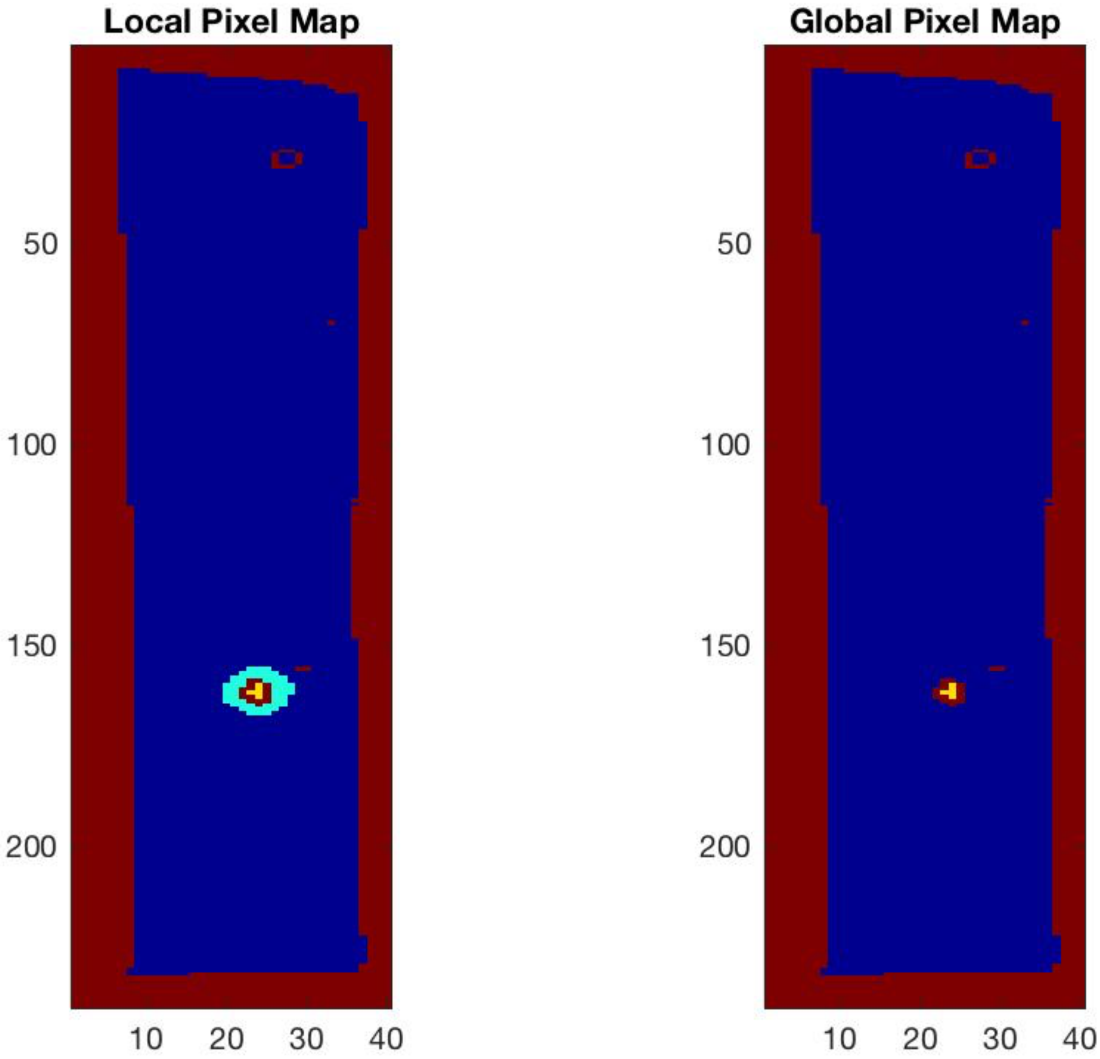

*Figure 5.5 Local and global flow phantom pixel maps. Pixel maps distinguish pixels used for local and global polynomial fitting by color. Vessel lumen and noise pixels are omitted during polynomial fitting (yellow and red respectively). Local corrections utilized phase estimates from a 4-pixel width ring of static tissue surrounding vessel lumens (teal). Global corrections utilized phase estimates from all static tissue pixels within the 2D FOV during polynomial fitting (blue pixels). Unique pixel maps are constructed for every vessel lumen corrected.*

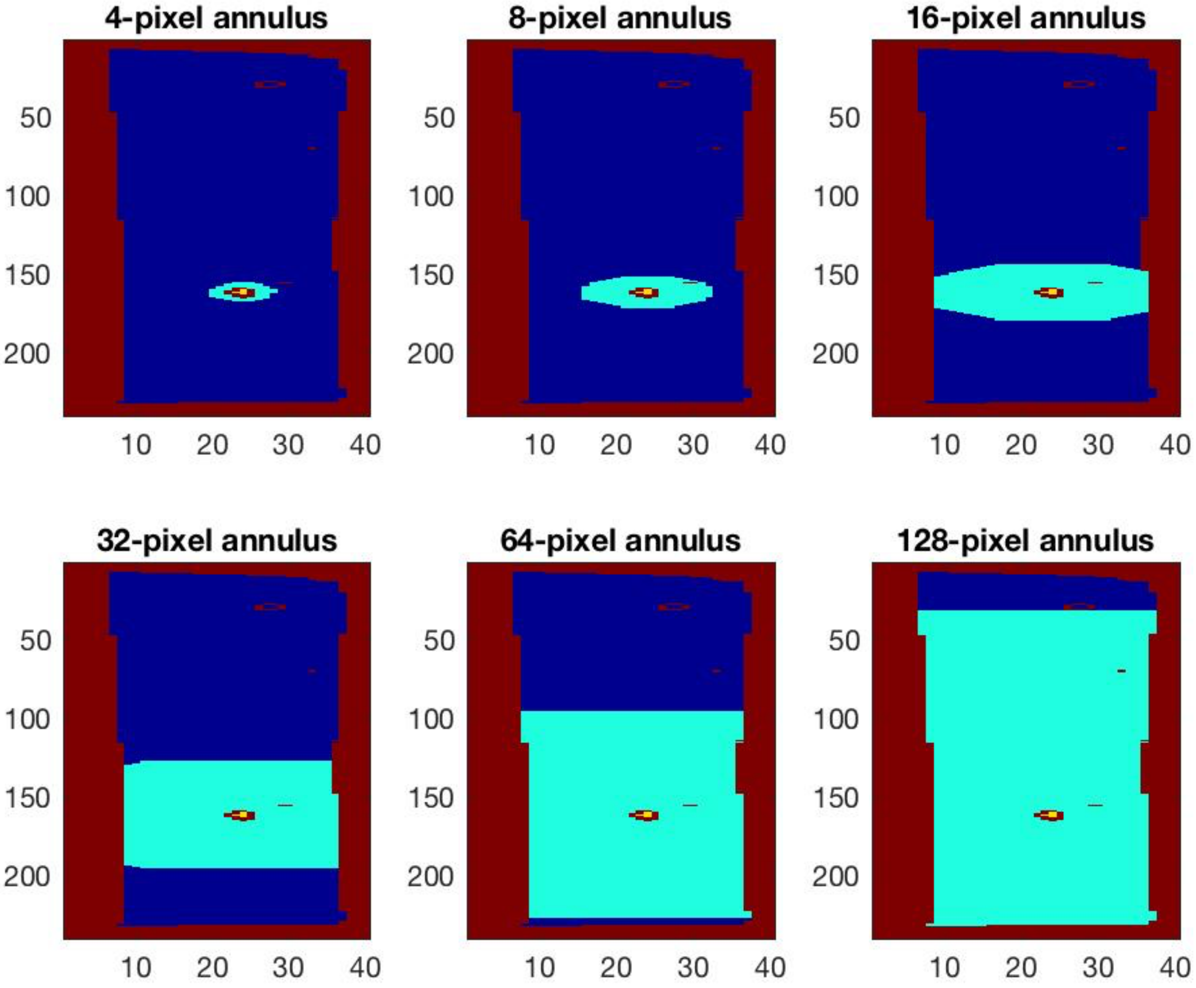

*Figure 5.6. Pixel maps with increasing static tissue coverage. Pixel maps distinguish pixels used for polynomial fitting by color. Rings of static tissue surrounding vessel lumens (teal) were increased in pixel width for polynomial fitting. Unique pixel maps were constructed for every vessel lumen corrected.*

Local and global corrections were separately applied to correct velocity estimates within vessel lumens (Figure 5.7). Corrections were repeated within axial velocity images for all acquired temporal phases. Unique local and global polynomial fits were generated to describe eddy current offsets for each temporal phase.

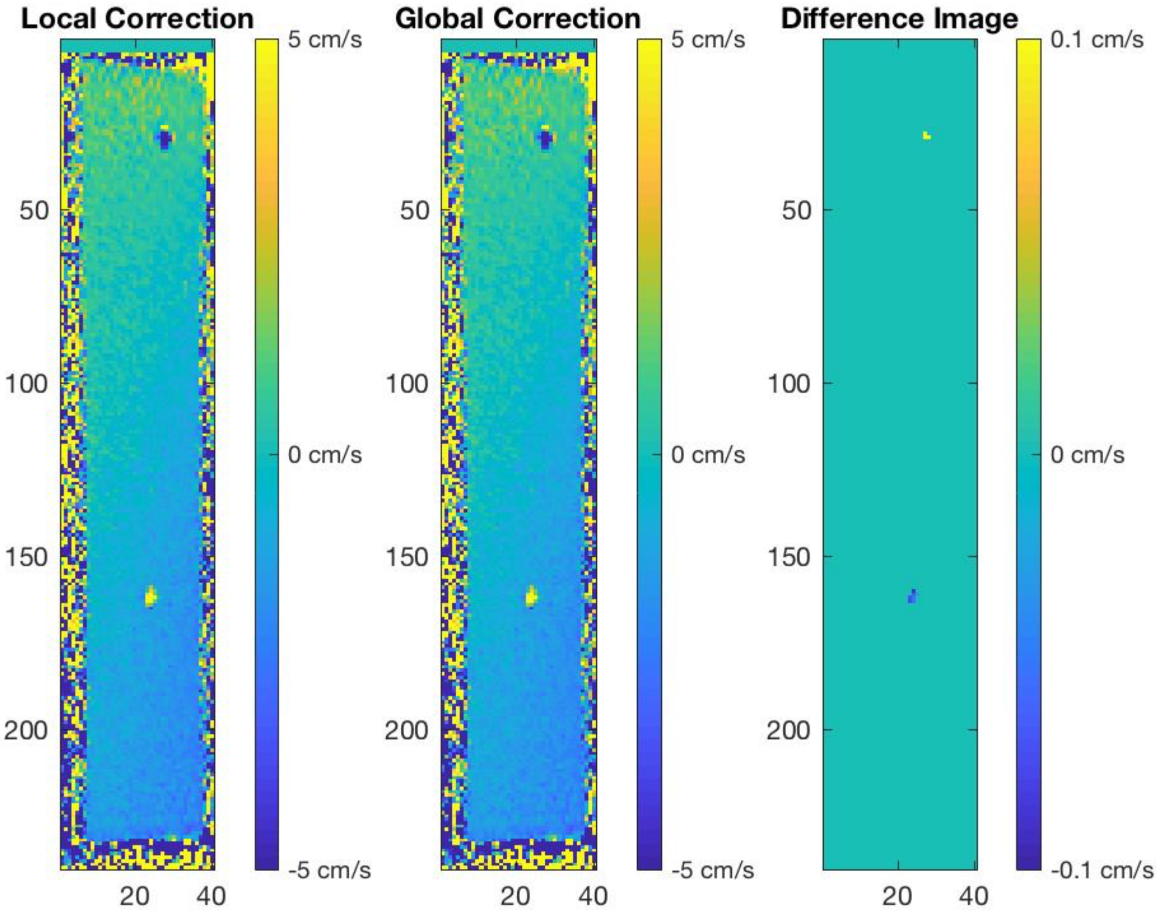

*Figure 5.7. Local and global corrected axial velocity images. Velocity estimates within vessel lumens were corrected on a pixel-by-pixel basis for eddy current offsets. Note that correction for a single axial slice position and temporal phase is shown. Velocity images from all acquired temporal phases were corrected prior to calculation of (corrected) total volumetric flows. A difference image confirms pixel-level differences (within vessel lumens) between applied local and global corrections.*

Estimates of total volumetric flow were calculated from both uncorrected and corrected velocity images. Separate estimates of total volumetric flow from a particular axial slice position were compared; and these flow differences ($\Delta Q_{total}$)

were recorded following no applied correction, local corrections, and global corrections. The same five axial slices of interest were analyzed for distinct SNR acquisitions. Distributions of $\Delta Q_{total}$ following local corrections, global corrections, and no applied corrections are shown in Figure 5.8.

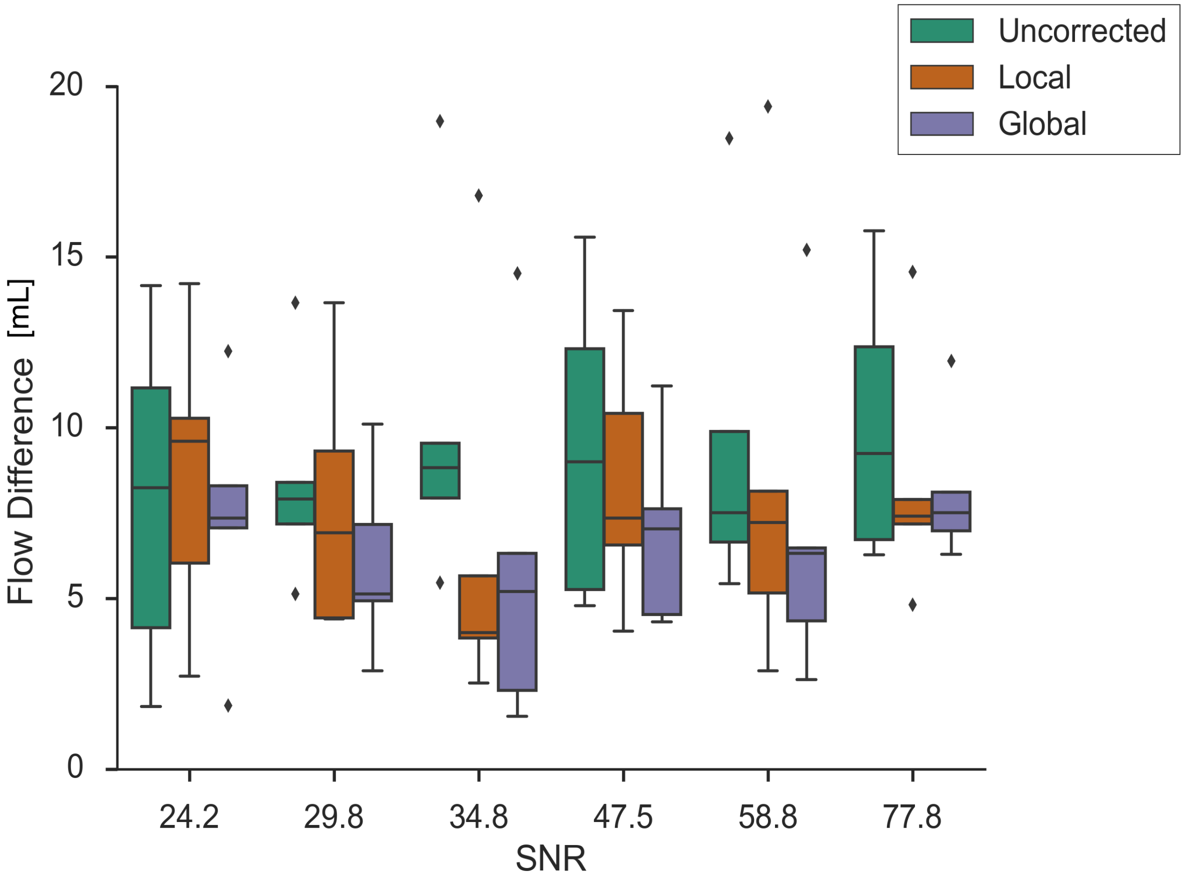

*Figure 5.8. Flow difference ($\Delta Q_{total}$) distributions for distinct SNR datasets. Uncorrected distributions (green) and distributions following both local (orange) and global (purple) corrections are shown. Two sample t-tests, repeated for each dataset, found no statistically significant differences between local and global corrected distributions (95% confidence). However, errors were observed with higher frequency in local corrections for low SNR applications.*

Uncorrected, local corrected, and global corrected differences between flow estimates ($\Delta Q_{total}$) were compared in 30 total cases (5 axial slice positions x 6 distinct SNR acquisitions). Static tissue corrections reduced flow difference ($\Delta Q_{total}$) in 27 of 30 cases. Global correction provided a larger reduction in flow difference ($\Delta Q_{total}$) in 18 of these 27 successful cases of static tissue correction. Global correction provided no change in $\Delta Q_{total}$ in 3 of 30 total cases and introduced error (increased $\Delta Q_{total}$) in 1 of 30 total cases. Global correction introduced this error in the 1° flip angle acquisition (lowest SNR). Local correction provided a larger reduction in $\Delta Q_{total}$ in 9 of 27 successful cases of static tissue correction. Local correction provided no change in $\Delta Q_{total}$ in 2 of 30 total cases and introduced error (increased $\Delta Q_{total}$) in 8 of 30 total cases. Local correction introduced error in acquisitions with flip angles of 1°, 2°, 4°, and 8°. No correction provided a smaller estimate of $\Delta Q_{total}$ than static tissue corrections (both local and global) in 1 of 30 total cases (observed in 1° flip acquisition). No correction provided estimates of $\Delta Q_{total}$ on par with static tissue corrections in 2 of 30 total cases.

Magnitude differences between total volumetric flows estimated by local and global correction techniques ("correction difference") are measured and averaged across all five axial slices of interest. Correction differences are measured for distinct SNR acquisitions and are shown in Figure 5.9.

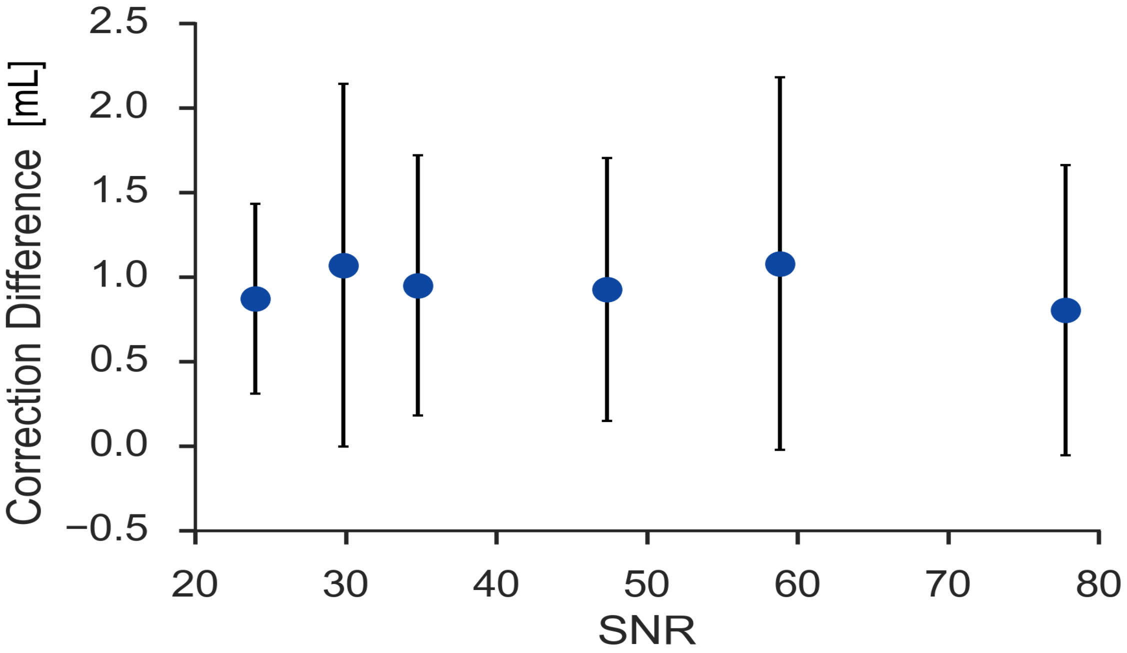

*Figure 5.9. Correction difference as a function of SNR. Correction difference between total volumetric flows estimated by local and global strategies remained relatively constant (~ 1.0 mL) across datasets spanning a range of SNR.*

Flow difference ($\Delta Q_{total}$) is measured as a function of surrounding static tissue annular width for all axial slices of interest. An average $\Delta Q_{total}$ vs. annulus width profile (across all axial slice positions) was then calculated. $\Delta Q_{total}$ vs. annulus width profiles are shown for distinct SNR acquisitions (Figure 5.10).

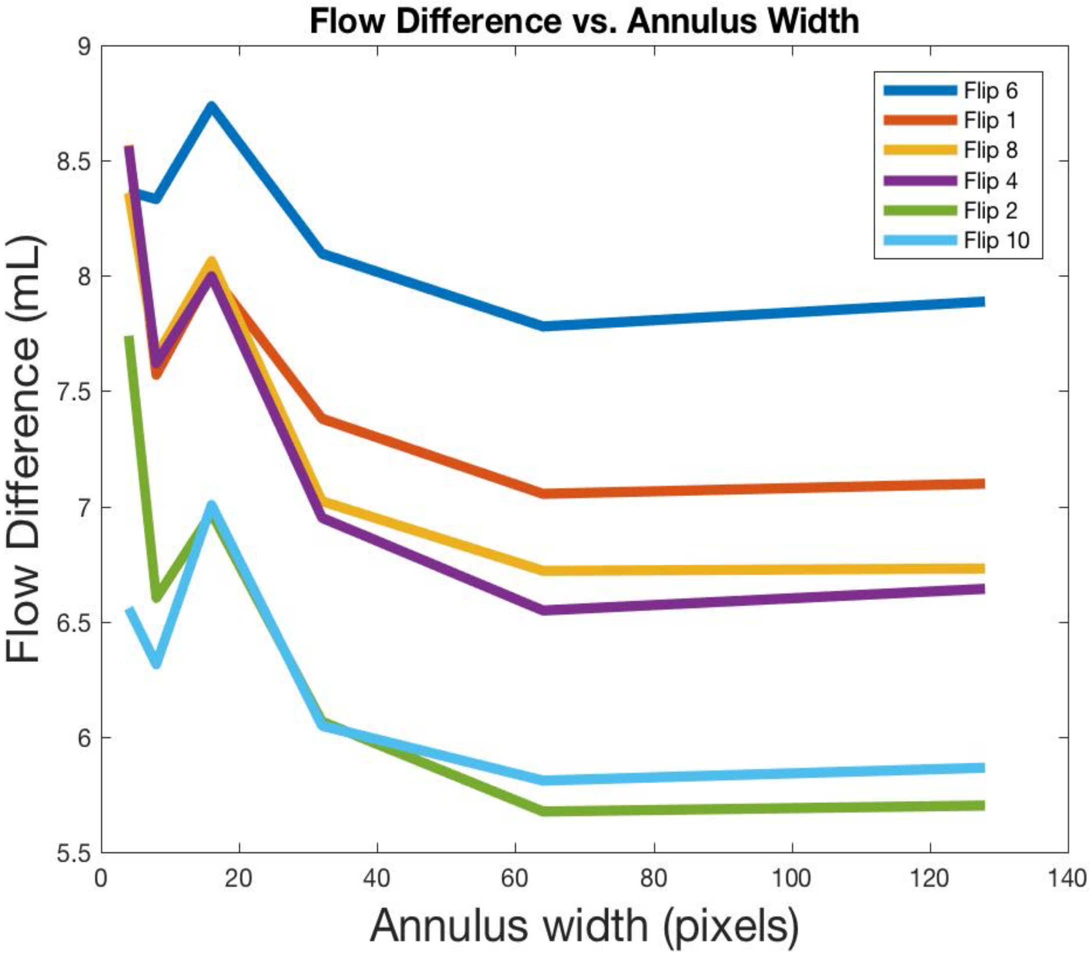

*Figure 5.10. Flow difference as a function of static tissue annulus width. Differences between total volumetric flow estimates ($\Delta Q_{total}$) were reduced upon increasing the amount of static tissue used during correction. Flow difference was reduced by up to an additional ~2 mL by increasing static tissue coverage.*

## 4. Discussion:

Offset on the order of 0.6 cm/s has previously been reported to affect estimates of cardiac output and shunt flow measurement by up to 5% and 10% respectively[1], and therefore the observed offset within this flow phantom experiment can be considered significant. Overall, static tissue correction proved useful in reducing differences between total volumetric flow estimates ($\Delta Q_{total}$) measured within a flow phantom (90% of total cases). Global correction provided a larger reduction in $\Delta Q_{total}$ in ~67% of cases of successful static tissue correction; however, was also seen to provide unsuccessful correction (no change or increase in $\Delta Q_{total}$) in ~13% of total cases. Global correction introduced error (increased $\Delta Q_{total}$) in one single case. This error occurred during global correction within the 1° flip angle acquisition alone (lowest SNR, SNR ~24). Local correction provided a larger reduction in $\Delta Q_{total}$ in ~33% of cases of successful static tissue correction; however, was also seen to provide unsuccessful correction (no change or increase in $\Delta Q_{total}$) in ~33% of total cases. Local correction introduced error (increased $\Delta Q_{total}$) in ~27% of total cases; these instances of local error occurred in datasets spanning a range of SNR (up to SNR of ~59). Although correction difference within the flow phantom experiment remained relatively constant (~1.0 mL) across SNR, local corrections were seen to introduce errors in correction with higher frequency (in comparison to global corrections). Figure 5.10 indicates that static tissue correction improved in ability to reduce flow differences ($\Delta Q_{total}$) upon increasing the amount of surrounding static tissue used during polynomial fitting. This study indicates that local static corrections strategies may only be suitable above a certain SNR level, and warrants further investigation. In addition, this study indicates that it is advisable to maximize the amount of static tissue used during polynomial fitting for corrections in low SNR applications.

## 5. References

1. Gatehouse, Peter D, et al. “Flow measurement by cardiovascular magnetic resonance: a multi-Centre multi-Vendor study of background phase offset errors that can compromise the accuracy of derived regurgitant or shunt flow measurements.” *Journal of Cardiovascular Magnetic Resonance*, BioMed Central, 14 Jan. 2010, jcmr-online.biomedcentral.com/articles/10.1186/1532-429X-12-5.

# Chapter VI: Conclusion:

## 1. Introduction:

Eddy current induced phase offsets lead to velocity errors ($v_{eddy}$) which remain a problem for absolute quantification within PC-MRI. Static tissue corrections aim to correct $v_{eddy}$ errors within velocity data by developing polynomial models to describe eddy current offsets. The aim of this work was to characterize local and global static tissue correction techniques in order to develop guidelines for their appropriate application. The dependence of local and global correction performance on SNR and on amount of static tissue used during polynomial fitting is not well understood within literature and was explored through a series of experiments.

## 2. Overall Findings:

Corrections were applied to reduce $v_{eddy}$ induced offsets within ROIs within a static tissue phantom. Corrections were also applied to reduce $v_{eddy}$ induced differences in total volumetric flow estimates measured from unique locations along a closed-circuit flow phantom. Corrections, in both experiments, were repeated for a range of SNR and for varying amounts of static tissue used during polynomial fitting. From both experiments, static tissue corrections proved useful in reducing $v_{eddy}$ errors as a whole. However, static tissue fitting techniques were also seen to occasionally introduce error upon correction. Notably, local corrections were seen to introduce errors with significantly increased frequency as SNR decreased. Additionally, corrections were observed to increase in performance by increasing the amount of static tissue used during polynomial fitting. Correction performance is more sensitive to increases in static tissue coverage for low SNR applications. Local correction is therefore suitable only above a certain range of SNR and warrants further investigation.

## 3. Future Work

As discussed, the exact range of SNR for which local correction introduces error is unclear and warrants further investigation. SNR in both experiments was estimated using ROI-based calculations; however, pixel-level SNR maps provide best assessments of true SNR. For instance when employing ROI-based calculations, SNR was not observed to increase by the square root of number of averages relationship within the static phantom experiment or observed to increase with flip angle within the flow phantom experiment (6° flip was highest observed SNR). Additionally, various limitations arose within the flow phantom experiment. In this experiment, the number of unique axial slice positions usable for flow difference comparisons was limited. Axial slices containing susceptibility artifacts from nearby restraints (used to hold the tubing network in place during the imaging experiment) were excluded from analysis; increasing the overall size of the phantom would increase the number of unique axial slice positions (free of these artifacts) usable for analysis. This experiment would also benefit from exploring corrections in a tubing network containing flow oriented along the x and y-dimensions of the scanner rather than the z-dimension alone; and by increasing the inner diameter of the polypropylene tubing used to construct the tubing network to simplify identification of vessel lumens. Furthermore, the effects of the location of static tissue used during polynomial fitting should be explored. Regions of static tissue used in corrections may be limited to locations far away from vessels of interest and thus may introduce inaccuracies upon applied corrections. Finally, the use of three-dimensional polynomial fits in describing eddy current offset should be investigated. Volumetric acquisitions offer the potential for polynomials to be fit to regions of static tissue in three-dimensional space rather than static tissue regions within the 2D FOV alone. This may offer an advantage upon applied correction as the eddy current induced field itself exists throughout the entire imaging volume and is not limited to a 2D slice position alone. Increasing the amount of information used (from static tissue throughout the imaging volume) during polynomial fitting may provide a better model describing eddy current error.